MEMS Positioners with Silicon Nitride Waveguides for Photonic Integrated Circuits Alignment

by

Almur Abdelkreem Saeed RABIH

MANUSCRIPT BASED THESIS PRESENTED TO ÉCOLE DE TECHNOLOGIE SUPÉRIEURE IN PARTIAL FULFILLMENT FOR THE DEGREE OF DOCTOR OF PHILOSOPHY
Ph.D.

MONTREAL, MARCH 5th 2024

ÉCOLE DE TECHNOLOGIE SUPÉRIEURE
UNIVERSITÉ DU QUÉBEC

ACKNOWLEDGEMENT

MEMS POSITIONERS WITH SILICON NITRIDE WAVEGUIDE FOR PHOTONIC INTEGRATED CIRCUITS ALIGNMENT

Almur RABIH

RÉSUMÉ

L'intégration de puces actives telles que les lasers et les amplificateurs optiques semi-conducteurs avec la photonique sur silicium est essentielle dans les circuits intégrés photoniques. Le silicium, en tant que plateforme principale de l'industrie des semi-conducteurs, n'est pas le bon substrat pour des puces actives efficaces. Ainsi, les puces actives fabriquées en externe sont actuellement intégrées à l'aide d'un assemblage flip-chip. Cependant, les désalignements verticaux et latéraux ainsi que les écarts horizontaux entre les guides d'onde des puces actives et les guides d'onde des puces de silicium sont des sources majeures de pertes optiques. Ce travail propose cinq dispositifs positionneurs MEMS pour assurer l'alignement dynamique des puces actives dans les circuits intégrés photoniques. Des dispositifs à plusieurs degrés de liberté (MDOF) ont été fabriqués et testés. Le premier dispositif est doté d'un actionneur piézoélectrique en nitrure d'aluminium pour assurer des déplacements vers le bas et vers le haut sur l'axe z. Le deuxième et le troisième dispositif utilisent des actionnements hybrides piézoélectriques-électrostatiques pour fournir respectivement des mouvements sur 2DOF et 3DOF. Tous les appareils sont équipés de peignes capacitifs pour suivre les déplacements, où une bonne corrélation entre la capacité détectée et les déplacements mesurés a été obtenue. De plus, l'alignement dynamique est assuré en activant plusieurs actionneurs à la fois et les guides d'ondes suspendus ont été alignés sur les guides fixes en compensant les désalignements dans le plan et hors du plan. Le quatrième appareil utilise trois actionneurs thermiques à chevrons pour fournir des mouvements 3DOF sur les axes x, y et z. Un déplacement important sur l'axe z a été obtenu grâce au flambage provoqué par deux forces thermiques opposées dans le plan. Le cinquième appareil fournit des mouvements dans le plan 2DOF sur les axes x et y à l'aide d'actionneurs thermiques. Les prototypes des dispositifs montrent que sur l'axe des x, le troisième dispositif fournit un déplacement total de 300 nm à ±100 V, tandis que le quatrième dispositif atteint un déplacement total de 6,7 μm à 105 mW. Sur l'axe y, des déplacements de 3,06 μm à 120 V, 10,9 μm à 140 V, 4,5 μm à 140 mW et 6,92 μm à 189 mW ont été obtenus respectivement par les deuxième, troisième, quatrième et cinquième dispositifs. Sur l'axe des z, les premier, deuxième, troisième et quatrième dispositifs assurent un déplacement respectivement de 1,3 μm, 3,16 μm, 0,63 μm à ±60 V et 7 μm à 210 mW. Contrairement aux quatre premiers positionneurs qui utilisent une couche de silicium sur isolant (SOI) de 10 μm d'épaisseur, le cinquième positionneur utilise une couche SOI de 59 μm d'épaisseur. De plus, ce positionneur est fabriqué avec un guide d'onde fonctionnant suspendu constitué d'un empilement de couches de dioxyde de silicium-nitrure de silicium-dioxyde de silicium. Le guide d'onde suspendu est

séparé d'un autre guide d'onde fixe identique de 6,92 ± 0,01 µm. La fermeture de cet écart a permis d'obtenir une perte d'insertion minimale de -1,60 ± 0,06 dB dans la plage de longueurs d'onde de 1550 à 1620 nm, tandis que la fermeture de l'écart tout en maintenant un déplacement latéral de ± 2 µm peut fournir une atténuation allant jusqu'à 20 dB. Ainsi, le dispositif peut fonctionner comme un atténuateur ou un interrupteur optique marche/arrêt. L'appareil dispose de deux guides d'ondes de sortie suspendus séparés de 10 µm et moins de -40 dB de diaphonie entre les guides d'ondes a été observée.

Mots-clés : Désalignement, actionnements dans le plan et hors plan, actionneur piézoélectrique, MEMS, contrainte résiduelle, nitrure d'aluminium, micro-positionneur 3 axes, alignement optique, nitrure de silicium, électrothermique, flambage de faisceau, électrostatique, capteur de déplacement.

MEMS POSITIONERS WITH SILICON NITRIDE WAVEGUIDE FOR PHOTONIC INTEGRATED CIRCUITS ALIGNMENT

Almur RABIH

ABSTRACT

The integration of active chips such as lasers and semiconductor optical amplifiers into silicon photonics is essential in photonic integrated circuits. Silicon as the main platform in the semiconductor industry, is not the right substrate for efficient active chips. Thus, externally fabricated active chips are currently integrated using flip-chip bonding. However, vertical and lateral misalignments, and horizontal gaps between the waveguides of the active chips and the waveguides of the silicon chips are the major sources of optical losses. This work proposed five MEMS positioner devices to provide dynamic alignment of active chips in photonic integrated circuits. Multi-degrees of freedom (MDOF) devices were fabricated and tested. The first device has an aluminum nitride piezoelectric actuator to provide downward and upward displacements in the z-axis. The second and third devices used hybrid piezoelectric-electrostatic actuations to provide 2DOF and 3DOF motions, respectively. All the devices were equipped with capacitive combs to track the displacements, where good correlation between the sensed capacitance and measured displacements were achieved. In addition, the dynamic alignment is provided by activating more than one actuator at a time, and suspended waveguides were aligned to the fixed ones by compensating in-plane and out-of-plane misalignments. The fourth device used three chevron thermal actuators to provide 3DOF motions in the x, y and z axes. A large z-axis displacement was achieved as a result of buckling caused by two opposite in-plane thermal forces. The fifth device provides 2DOF in-plane motions in x- and y- axes using thermal actuators. Prototypes of the devices show that in the x-axis, the third device provides total displacement of 300 nm at ±100 V, whereas the fourth device achieves a total of 6.7 μm displacement at 105 mW. In the y-axis, displacements of 3.16 μm at 120 V, 10.9 μm at 140 V, 4.5 μm at 140 mW and 6.92 μm at 189 mW were achieved by the second, third, fourth and fifth devices, respectively. In the z-axis, the first, second, third and fourth devices give 1.3 μm, 3.16 μm, 0.63 μm, at ±60 V, and 7 μm at 210 mW, respectively. Unlike the first four positioners that used 10 μm-thick silicon-on-insulator (SOI) layer, the fifth positioner utilized a 59 μm-thick SOI layer. Also, this positioner is fabricated with a suspended functional waveguide made of a stack of silicon dioxide-silicon nitride-silicon dioxide layers. The suspended waveguide is separated from another identical fixed waveguide by 6.92 ± 0.01 μm. Closing this gap achieved -1.60 ± 0.06 dB minimum insertion loss from 1550 to 1620 nm, whereas closing the gap while maintaining ± 2 μm lateral displacement can provide an attenuation of up to 20 dB. Thus, the device can operate as an attenuator or an on/off switch.

TABLE OF CONTENTS

Page

LIST OF TABLES

LIST OF FIGURES

Page

LIST OF ABREVIATIONS

1DOF	One Degree of Freedom
2DOF	Two Degrees of Freedom
3DOF	Three Degrees of Freedom
AlN	Aluminium Nitride
Al	Aluminium
BCB	Benzocyctobutene
CMOS	Complementary-Metal-Oxide-Semiconductor
CTE	Coefficient of thermal expansion
CVD	Chamical vapor deposition
DRIE	Deep Reactive Ion Etching
DUT	Device Under Test
ETS	École de Technologie Supérieure
FCB	Flip-chip bonding
FDTD	Finite-difference time-domain
FEA	Finite element analysis
FFT	Fast Fourrier Transform
GaAs	Gallium Arsenide
Ge	Germanium
InGaAs	Indium-Gallium-Arsenide
InP	Indium Phosphide

LPCVD   Low pressue chemical vapor deposition

MDOF   Multi-Degrees-of Freedom

MEMS   Micro-Electro-Mechanical Systems

MOEMS   Micro-Opto-Electro-Mechanical Systems

OD   Optical detector

PECVD   Plasma-enhanced chemical vapor deposition

PICs   Photonics integrated circuits

PVD   Physical vapor deposition

PWB   Photonic wire bonding

PZT   Lead zirconite titanate

RF   Radio frequency

RIE   Reactive-Ion Etching

SEM   Scaning electron microscope

Si   Silicon

SiN   Silicon nitride

SiO2   silicone dioxide

SOA   Semiconductor optical amplifier

SOI   silicon-on-insulator

UQAM   Université du Québec à Montréal

UV   Ultraviolet

WG   Waveguide

INTRODUCTION

Photonics integration is a fast growing trend that provides compact and low power devices for communication, sensing and quantum applications (Chang, Zhou, Tamura, & Hung, 2022). Silicon photonics is among the most blooming platforms for photonics integration, due to various distinctive advantages such as large-scale integration, low cost-production (Suzuki et al., 2017), excellent optical properties and compatibility to Complementary Metal Oxide Semiconductor (CMOS) technology (Wenqi et al., 2022). Among the silicon photonics platforms, silicon-on-insulator (SOI) and silicon nitride (SiN) are generating special interests. SOI has a high refractive index contrast that enables the fabrication of small cross-section and bending radius waveguides (Y. Chen et al., 2022). In addition, SOI supports fabricating several photonics building blocks, such as Y-junctions (Su, Liu, & Zhang, 2022), couplers (Vitali, Lacava, Domínguez Bucio, Gardes, & Petropoulos, 2022), interferometers (El Shamy, Afifi, Badr, & Swillam, 2022), gratings (Zha, Li, Wen, Zhou, & Zhang, 2022) and resonators (Zeng et al., 2022). SiN offer passive devices with outstanding performance, due to its very low loss and low susceptibility to phase errors (Theurer et al., 2019). Despite the excellent properties of silicon-based platforms, the indirect bandgap structure of silicon prevents the emission of efficient light (Y. Han, Park, Bowers, & Lau, 2022). Thus, commonly, externally fabricated active chips such as laser sources and semiconductor optical amplifiers (SOAs) are integrated on silicon photonics platforms using techniques based on flip-chip bonding (Zia et al., 2022). However, this integration method requires a stringent assembly process (Y. Yang et al., 2021) which makes the alignment very challenging (Moody et al., 2022).

Micro-electro-mechanical systems (MEMS) positioners made on SOI platforms and equipped with suspended SiN waveguides are expected to provide alignment of these silicon photonics waveguides to active chip waveguides to realize an efficient chip-to-chip light coupling. Active dynamic alignment is also possible by using CMOS control circuitry to continuously monitor the light coupling and track the displacements of the suspended waveguides to maintain the efficient coupling. Silicon photonics MEMS provide small size, low power consumption, and

low cost devices (Leondes, 2006). Such devices include optical switches (Guerre, Hibert, Burri, Flückiger, & Renaud, 2005; T. Liu et al., 2017), phase shifters (Ikeda, Takahashi, Kanamori, & Hane, 2010; Oda et al., 2012)*,* variable optical couplers (Abe & Hane, 2013; J. Yao, Leuenberger, Lee, & Wu, 2007) and ring/disk resonators (Errando-Herranz, Niklaus, Stemme, & Gylfason, 2015; Sridaran & Bhave, 2011), to name a few. The most used MEMS actuation techniques to control silicon photonics devices are electrostatic (N. Quack et al., 2020), piezoelectric (Ruiz-Díez et al., 2021), electrothermal (Sciberras et al., 2022) and electromagnetic (Yunas et al., 2020) effets. A brief explanation of the work principle for each actuator will be presented in chapter 1.

0.1   Problem statement

As stated, the industrial standard silicon photonics platforms are not the right candidates for light generation or for amplification. As majority of silicon photonics are inherently passive components and it is challenging to create monolithic light sources, there is a vital need to integrate non-silicon active components such as laser diodes and in-line SOAs.

Currently, the main efforts made to integrate active chips include:

- Hybrid-integration based on flip-chip or wafer bonding technologies:
  These techniques require a stringent assembly process to maintain good alignment during the active device bonding, yet achieving fine alignment is a challenge due to lateral and vertical misalignments and protection gaps left between the cleaved edge of the active chip and the silicon-based waveguides. The alignment accuracy depends on both accuracy of fabrication tools and bonding machines (Li et al., 2022).

- Heterogeneous integration based on die/wafer bonding and micro-transfer printing:
  This technique bonds the active chip during the wafer bonding. However, it lacks the ability to pre-test the active chip before the integration, and that does not guarantee the efficient functionality of the active chip. Beside, the throughput is also low (Y. Han et al., 2022).

- Monolithic integration through direct growth on silicon-based platforms:

This technique builds the active device on the silicon photonics layer using direct epitaxial growth. However, the lattice mismatch between the silicon and active device layer causes defects that shorten the lifetime of the devices (Kaur et al., 2021). In addition, this method has low yield (Billah et al., 2018).

- Recently, the direct Photonic Wire Bonding (PWB) method was proposed:
  This method resolves the issues related to misalignments. However, PWB requires a complex manufacturing process with several elaborate steps (Billah et al., 2018), hence, availability, reliability and production yield of PWB need further confirmation.

Therefore, there is a need for accessible and reliable dynamic integration method that does not rely on the accuracy of bonding machines, and that is able to integrate proved-functionality active chips. MEMS positioners are proven to be the right candidates.

0.2 Objectives of the research

The aim of this research is to develop Multi-Degrees of Freedom (MDOF) MEMS actuators as waveguide positioners to align active components to passive counterparts on silicon photonics platforms. The following are the three specific objectives of this research:

1. To identify different actuation principles and identify suitable techniques to achieve the required displacements that can compensate for the misalignments left by the current active chip integration techniques, taking into account size, fabrication complexity, and power consumption of the actuators.

2. To combine individual MEMS actuators and form 3-DOF positioners that are able to carry suspended waveguides and provide the required displacements in x-, y- and z-axes, and to numerically model and simulate these positioners and study the effect of varying their parameters (like length, width and thickness) on the generated motion.

3. To experimentally conduct mechanical and optical tests to determine the performance of the positioners and their suitability to resolve the research problem.

0.3   Research novelty and contributions

This research contributed to scientific knowledge by proposing novel techniques for generating out-of-plane vertical motion based on a pre-deformed platform and in-plane forces, in addition to using hybrid piezoelectric and electrostatic techniques to achieve multi-degrees of freedom motion. Furthermore, following are the expected direct industrial impacts:

1. The development of a MEMS dynamic alignment system is expected to reduce the vertical and lateral misalignments, and close the horizontal gaps between the waveguides in the active chip and those in the silicon chip during packaging and also in operation. Thus, the insertion losses encountered by the current static alignment based on hybrid bonding could be reduced, and the light coupling efficiency could be enhanced.

2. Due to the small size of MEMS actuators and the possibility of mass production, fast, low power consumption and low cost photonic integrated circuits could be realized.

As an outcome for this research, four journal manuscripts with the following titles were published:

a) Rabih, A. A. S., Kazemi, M., Ménard, M., & Nabki, F. (2023). Aluminum Nitride Out-of-Plane Piezoelectric MEMS Actuators. Micromachines, 14(700). doi:https://doi.org/10.3390/mi14030700.

b) Rabih, A. A. S., Sharma, S., Pita, J., Ménard, M., & Nabki, F. (2023). Two-axis MEMS positioner for waveguide alignment in silicon nitride photonic integrated circuits. Optics Express, 31(19), 30797-30814. doi:10.1364/OE.500102 (featured as one of the top-downloaded papers in September 2023)

c) Rabih, A. A. S., Nabavi, S., Ménard, M., & Nabki, F. (2024). Multi Degrees-of-Freedom Hybrid Piezoelectric-Electrostatic MEMS Actuators Integrated With Displacement Sensors. Journal of Microelectromechanical Systems, 33(1), 21-36. doi:10.1109/JMEMS.2023.3341039.

d) Rabih, A. A. S., Nabavi, S., Ménard, M., & Nabki, F. (2024). A 3 Degrees-of-Freedom Electrothermal Micro-positioner for Optical Chip-to-chip Alignment. Journal of Microelectromechanical Systems. doi:10.1109/JMEMS.2024.3371829.

In addition, a declaration of invention entitled "Multi-degrees of freedom MEMS actuators as waveguide positioners" was submitted.

0.4   Organization of the thesis

The rest of the thesis is structured as follows:

Chapter 1 presents the theoretical background on the commonly used MEMS actuation techniques, with their main advantages and disadvantages. In addition, the fundamental steps of micromachining fabrication processes, MEMS compatibility with CMOS, and our research limitations are highlighted.

In chapter 2, a literature survey on the state of the current existing co-integration techniques of photonic chips are presented. Moreover, this chapter also cover the state-of-the-art MEMS actuators in photonic integrated circuits, with more focus on the ones used for active chips alignment.

Chapters 3 − 6 present the four journal manuscripts produced during the period of this research study:

    -Chapter 3 presents an out-of-plane actuator made of aluminum nitride piezoelectric layer, equipped with capacitive sensing for tracking the displacement.

    -In chapter 4, two-axis and three-axis positioners with hybrid piezoelectric-electrostatic actuations are presented. The positioners are also equipped with capacitive combs to track the displacements. In addition, the positioners are able to compensate the misalignments of the suspended waveguides by simultaneous activation of more than one actuator.

    -Chapter 5 introduces a three-axis electrothermal positioner, where the out-of-plane motion is generated from two opposite in-plane thermal forces, with large displacements.

    -In chapter 6, a two-axis electrothermal positioner with active SiN optical waveguides is presented. Good mechanical and optical results are obtained.

The thesis is concluded by highlighting the key findings, and future recommendations for further improvements of the MEMS positioners are given.

CHAPTER 1

THEORETICAL BACKGROUND

1.1   Introduction

One of the major parts of the MEMS positioning devices is the MEMS actuator. It is essential to actuate the integrated waveguides, which leads to modification of their properties (length, direction and index of refraction) in order to realize the various applications of the photonic integrated circuits (PICs). There are several MEMS actuation techniques available, and the most used ones are electrostatic, electro-thermal, electromagnetic and piezoelectric. They are fabricated using well-known semiconductor fabrication steps. In the next sections, each actuation technique is briefly introduced, with its advantages and disadvantages, followed by the main fabrication steps. Compatibility of MEMS devices with the CMOS technology will be discussed and this chapter is ended by our research limitations.

1.2   Actuation mechanisms

Figure 1.1 illustrates four different actuation mechanisms that will be covered here: electrostatic, electrothermal, electromagnetic, and piezoelectric, each with a schematic diagram and the corresponding force equation.

1.2.1   Electrostatic actuation

This technique depends on the electrostatic force generated between two parts having different electric potentials. There are two principal types of electrostatic actuation: parallel plates and comb drive actuators. Compared to other actuation techniques electrostatic actuation requires very high voltages. However, it has low power consumption, very fast speed, and straightforward integration with optical components (Brière, Beaulieu, Saidani, Nabki, & Menard, 2015). As shown in Figure 1.1(a), the electrostatic force F_e generated by two parallel

plates separated by an initial gap d is determined using (1.1) (Megat Hasnan, Mohd Sabri, Mohd Said, & Nik Ghazali, 2014).
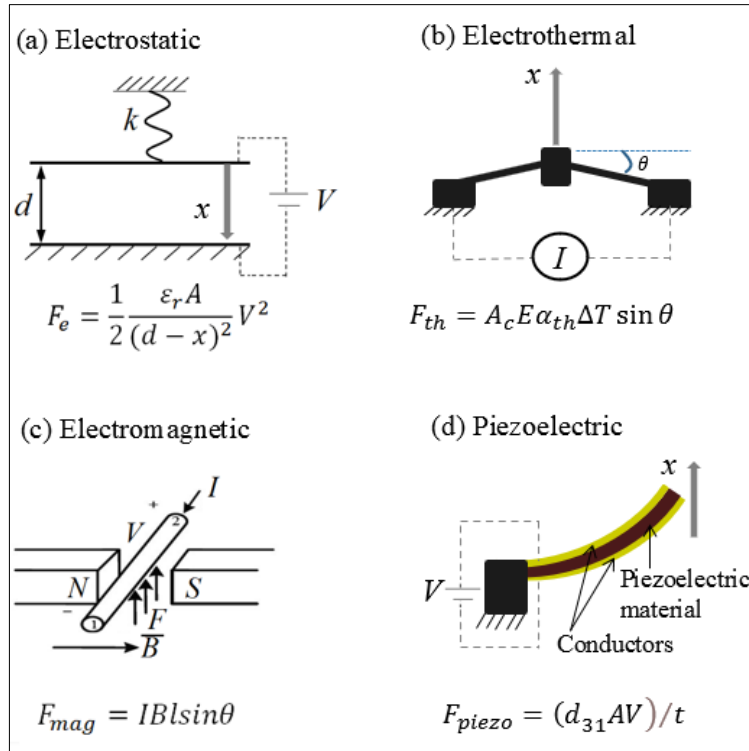
Figure 1.1 Common MEMS actuation methods, (a) electrostatic, (b) electrothermal, (c) electromagnetic, and (d) piezoelectric

$$F_e = \frac{1}{2}\frac{\varepsilon_r A}{(d-x)}V^2 \tag{1.1}$$

where ε_r is permittivity of the material between the two plates, A is the area of the plates, x is the displacement, and V is the voltage applied between the two plates.

1.2.2   Electro-thermal actuation

Electrothermal actuation depends on the thermal stress caused by either mismatch in coefficient of thermal expansion (CTE) of the actuator materials, or by different current densities in a single layer of different geometries. Due to geometry differences, some parts of the actuator expand and contract faster than others, leading to a motion. It is also possible to

use a V-shaped chevron actuator to induce the motion. The thermal bimorph based on materials with different CTEs is famous to achieve vertical displacements (X. Zhang, Zhou, & Xie, 2016). Electrothermal actuators have many advantages such as simplicity and easiness of implementation, in addition to providing large displacements at very low applied voltages. However, due to their dependence on the joule heating, electrothermal actuators requires high currents, thus they consume much power (Larsen et al., 2017) compared to other actuators. As shown in Figure 1.1(b), the electrothermal force F_{th} generated due to passing a current I through the chevron legs is found using (1.2) (Vargas-Chable, Tecpoyotl-Torres, Vera-Dimas, Grimalsky, & Mireles García, 2022).

$$F_{th} = A_c E \alpha_{th} \Delta T \sin \theta \tag{1.2}$$

where A_c is the cross-sectional area of the chevron leg, E and α_{th} are the Young's modulus and the coefficient of thermal expansion of the material used to build the actuator, ΔT is the temperature difference to the ambient environment, and θ is the angle of inclination of the chevron leg.

1.2.3   Electromagnetic actuation

Electromagnetic actuation uses the Lorentz magnetic force generated due to passing current on a wire placed between two poles of a permanent magnet or electrically induced magnetic field. This actuation technique is able to provide relatively large torques and hence large displacements at a low applied voltage. However, due to the need for magnets, the design becomes bulky and the fabrication is complex (Overstolz, 2007). A schematic showing the operating principle of electromagnetic actuation is shown in Figure 1.1(c), where the electromagnetic force F_{em} generated due to passing a current I through a wire placed between two magnetic poles is calculated using (1.3) (Yunas et al., 2020).

$$F_{em} = IBl \sin \theta \tag{1.3}$$

where l is the length of the wire, B is the radial component of the magnetic field in the wire plane, and θ is the angle direction of the magnetic field with regard to the vertical axis.

1.2.4   Piezoelectric actuation

Piezoelectric actuation provides displacements by applying an electric field across a piezoelectric layer of the structure. This technique features a fast response at low voltage and low power consumption (Piyawattanametha & Qiu, 2012). However, piezoelectric actuation does not typically provide large displacements, as the deformation is induced into the bulk of the piezoelectric material (F. Chollet & Liu, 2018). In Figure 1.1(d), the mechanism of piezoelectric actuation is depicted, where displacement is induced through the application of a voltage differential across a piezoelectric material that is flanked by conductive layers, leveraging the inverse piezoelectric effect. The resultant out-of-plane force, denoted as F_{piezo}, is quantified using equation (1.4) (Sharma et al., 2023a), illustrating the direct proportionality between the electrical input and mechanical response in such actuators.

$$F_{piezo} = (d_{31}AV)/t \tag{1.4}$$

where d_{31} is the piezoelectric coefficient, A is the area of the actuator, V is the voltage applied between the top and bottom conductors of the piezoelectric material, and t is the thickness of the piezoelectric layer.

1.3   Fabrication methods

To fabricate MEMS actuators side by side with photonic devices, the common micro and nanofabrication standards in semiconductor industries are used. Various fabrication foundries are available, including CMOS, Silicon on Insulator (SOI), PolyMUMPs and PiezoMUMPs technologies, beside other customized techniques. The main fabrication processes involved such as lithography, etching and deposition steps, are briefly explained in the following sections.

1.3.1   Lithography

Photolithography is the major technique used to transfer a pattern on a mask (normally glass) into a thin film on a substrate (often silicon) to design the required shape of the device, by the

help of a photoresist material. After coating the thin film with the photoresist, the substrate is aligned to the mask under a microscope and the photoresist layer is exposed to a UV light, then developed in a chemical solution to create the patterns. Etch process follows the lithography to remove the unwanted portions of the designed layer, then the remained photoresist is stripped off to complete the lithography sequence (Guangya Zhou & Lee, 2018).

1.3.2   Deposition of thin film layers

There are two broad categories for the methods used to deposit thin films. The first category is physical vapor deposition (PVD), while the other category is chemical vapor deposition (CVD). PVD depends on physical characteristics by vaporizing the material or using ion bombardment to force the material to change to its gaseous form to deposit onto the substrate. PVD uses thermal evaporation, electron beam or plasma (sputtering process). On the other hand, CVD depends on chemical reactions on the surface of the substrate to deposit the thin layer. Compared to PVD, CVD gives a high deposition rate, good coverage and does not require vacuum pressures. Low-pressure (LPCVD) and plasma-enhanced (PECVD) (Guangya Zhou & Lee, 2018) are used to address the issues of the conventional CVD.

1.3.3   Etching

In the microfabrication process, selective removal of specific regions from a deposited and patterned layer is achieved through an etching step, which is classified into wet etching and dry etching categories. Wet etching operates with chemical solutions, with the etchant in liquid form. Dry etching, in contrast, can be conducted via chemical or physical methods, with etchants in gas or plasma states. Although wet etching is typically associated with isotropic etching behaviors, meaning it removes material uniformly across all directions, anisotropic wet etching techniques have been established, allowing for material to be etched at different rates in different directions. Dry etching methods, such as reactive ion etching (RIE) and deep reactive ion etching (DRIE), are capable of achieving high aspect ratios and anisotropic etching profiles, which are critical for detailed microscale feature fabrication (Guangya Zhou & Lee,

2018). These etching techniques are pivotal for the precision and adaptability they bring to the etching process in the field of microfabrication.

1.4   MEMS compatibility to standard CMOS technology

MEMS technology is often recognized for its alignment with established CMOS processes, as evidenced by the successful integration of CMOS MEMS in various applications, like Texas Instruments' CMOS-MEMS digital micromirror devices and an array of sensors outlined in (H. Qu, 2016). Industry leaders such as TSMC and Globalfoundries have also begun to incorporate piezoelectric actuation into their CMOS fabrication lines, expanding the horizons for commercial MEMS products (Y. He, 2021). Despite the advancements in MEMS, the integration with increasingly miniaturized and complex CMOS technology poses substantial challenges. The adaptation of CMOS processes for MEMS incorporation must be approached with caution to prevent compromise to the CMOS transistors' integrity and functionality. The integration process demands meticulous attention to factors like thermal budgets, chemical compatibility, and mechanical stresses. This complexity necessitates thorough analysis to maintain the operational reliability of CMOS transistors after MEMS integration, accentuating the fact that achieving seamless compatibility remains a formidable task for engineers. However, the industry's progression, as demonstrated by the integration of piezoelectric actuation by leading companies, shows a willingness to balance trade-offs. In instances where MEMS devices offer valuable solutions to pressing issues, such as optical losses in photonic integrated circuits (PICs), foundries may consider specific alterations to CMOS processing steps as acceptable compromises.

1.5   Research limitations

In the development of multi-degree-of-freedom MEMS positioners for active optical alignment in photonic integrated circuits (PICs), our research confronted several fabrication constraints. We employed two distinct fabrication technologies, each with specific limitations. The first technology, PiezoMUMPs by MEMSCAP, includes a 10 μm-thick SOI device layer, a 0.2 μm pad oxide layer, a 0.5 μm piezoelectric layer, and a 1 μm aluminum metal layer. The second

fabrication process, provided by AEPONYX inc., utilized a thicker, 58 µm SOI device layer, and required that all MEMS structures fit within a cavity of 1400 µm by 625 µm. Crucially, this second process permitted the integration of optical waveguides above the SOI device layer, a pivotal factor in the optical operational demonstration of the positioners. Each fabrication method also imposed minimum width restrictions for the fabricated layers, necessitating certain compromises to conform to these rules, while still achieving the displacements needed for effective PIC alignment.

CHAPTER 2

LITERATURE SURVEY

2.1   Introduction

The introductory chapter outlined the critical role of technological advancements in enhancing photonic integrated circuits (PICs), which necessitate light sources and amplification at specific stages. Silicon, despite being the predominant material in these technologies, lacks the intrinsic properties to efficiently generate or amplify light. Consequently, alternative materials like indium phosphide and gallium arsenide are employed for active components. A significant hurdle in PIC development is the integration of these disparate components, where alignment discrepancies can lead to substantial optical losses. Our work proposes the use of MEMS positioners integrated with suspended waveguides as a novel approach to address misalignment, aiming to achieve optimal light coupling efficiency.

This chapter begins with an overview of co-integration methods that facilitate the bonding of active chips to silicon-based platforms. Following this, we present instances where MEMS actuators have been successfully applied within PICs to correct alignment issues, underscoring the limitations of current integration techniques. The persistent challenge of overcoming misalignment in PICs, coupled with the demonstrated effectiveness of MEMS actuators, forms the foundation for our proposed solution. This entails the deployment of multi-degree-of-freedom MEMS positioners, a topic that will be elaborated upon in subsequent chapters, showcasing our contribution towards resolving integration challenges in PICs.

2.2　　　Co-integration methods of active components in photonic integrated circuits

To address the passivity of silicon photonics, in-line integration of active chips like laser sources and semiconductor optical amplifiers (SOAs) is of a great importance. Several bonding techniques are available, depending the fabrication stage at which the integration is required. Figure 2.1 shows monolithic, wafer-to-wafer, die-to-wafer and die-to-die bonding techniques.

Monolithic integration is made by epitaxial growth of active material like germanium (Ge) and gallium arsenide (GaAs) on the silicon photonics layer. The advantages of this method are reducing size and the possibility of using the same material for various functions like gain, optical and mechanical functions by doping the material. However, it needs a trade-off for the material properties to cater for both optical properties (e.g. refractive index and thickness) and mechanical properties (e.g. stiffness and mechanical stresses) (Franck Chollet, 2016). In addition, there are coupling and propagation losses (Li et al., 2022). Wafer-to-wafer bonding
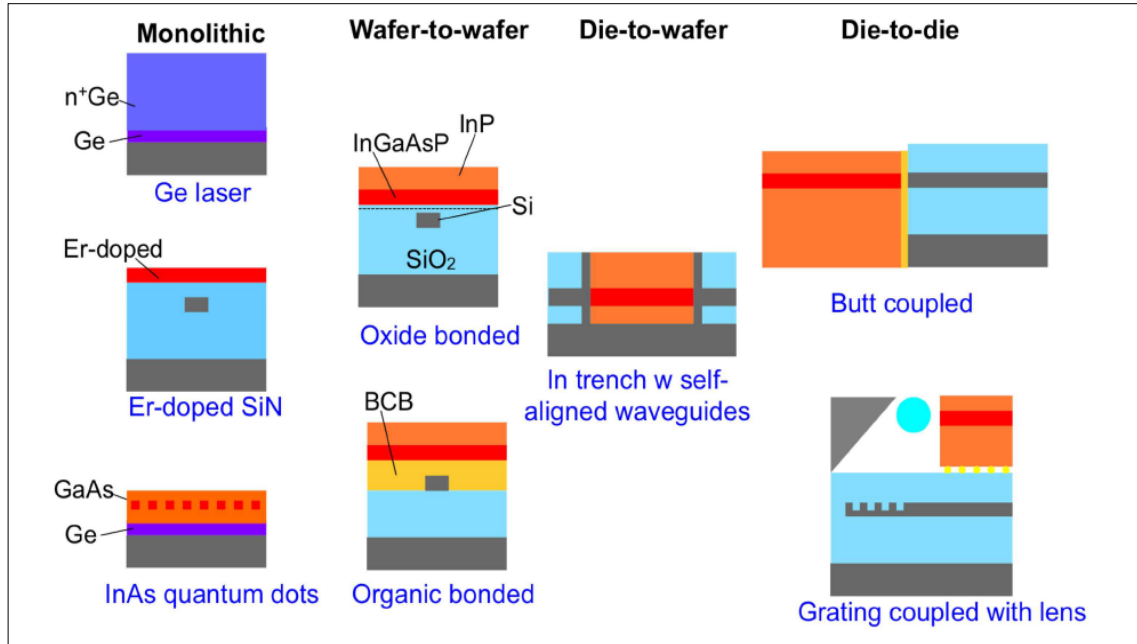
Figure 2.1 Integration mechanisms to include active optical devices into silicon photonic circuits: monolithic with direct growth of Ge, wafer-to-wafer where oxide or organic bonding is used to bond Si and InP wafers, die-to-wafer where trench is created on Si to bond the active chip, and die-to-die where two fully processed dies are integrated through butt or grating couplers
(Richard Doerr, 2015)

uses oxide or organic bonding such as benzocyclobutene (BCB) to bond the two wafers together. Die-to-wafer bonding requires creating trenches in the silicon carrier wafer to insert and bond the active die. The fourth co-integration strategy is die-to-die integration. In this technique, active components are fabricated using different dies to that used for MEMS and passive components, and then the dies are bonded together. Flip-chip bonding (FCB) and side by side system in package (butt coupling or grating couplers) are two examples of bonding techniques that have wide use in hybrid integration. Currently, the most used strategy for active components integration is performed by utilizing hybrid integration based on wafer bonding and FCB technologies. For instance, (Carrara et al., 2017) and (De Groote et al., 2016) used wafer bonding technology to integrate III-V optoelectronic components on a silicon on insulator (SOI) substrate to fabricate on chip laser sources. In wafer bonding technology, the alignment is performed lithographically in wafer scales as shown in Figure 2.2 for III-V/Silicon photonics integration.

In FCB technology, the chip is face-down flipped over and attached to substrate or another chip to have electrical and mechanical contact by using conductive bumps (Fretz, 2009).
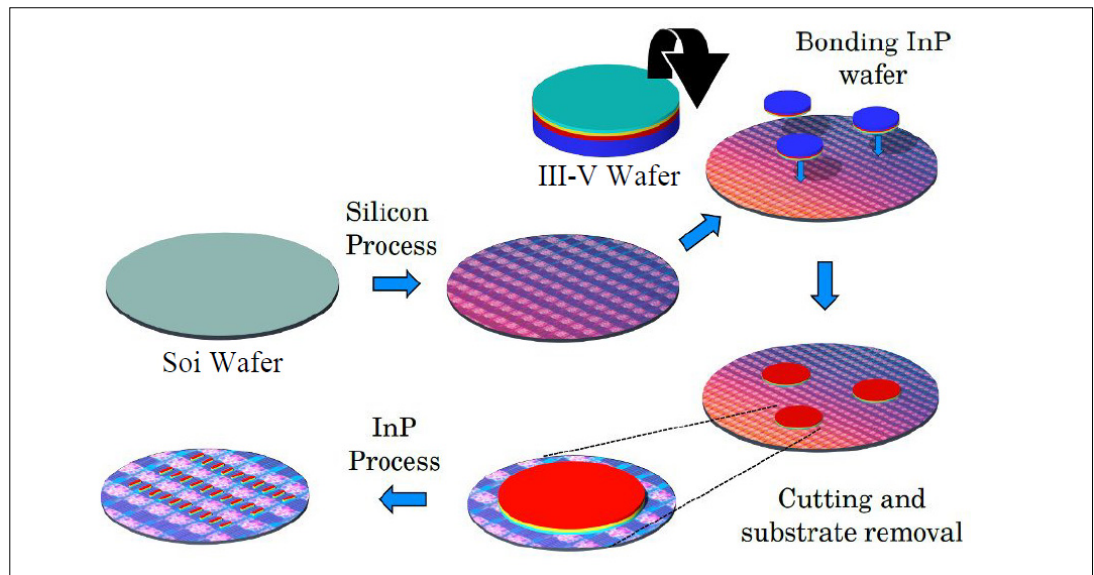
Figure 2.2 Hybrid integration of III-V components on SOI substrate
Taken from (Carrara et al., 2017)
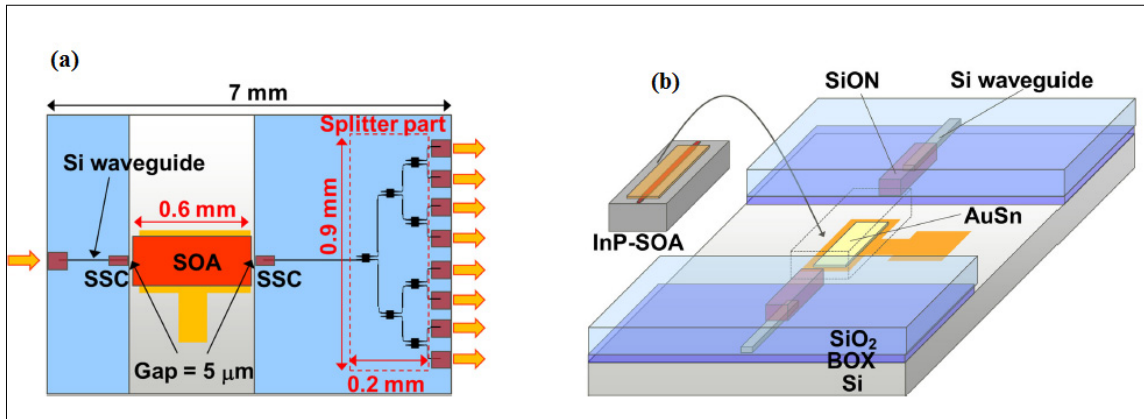
Figure 2.3 Integration of InP-SOA chip to silicon photonic platform: (a) schematic of InP-SOA inline integration to 1 × 8 Si optical splitter, and (b) configuration of flip-chip bonding technology for InP-SOA gain chip
Taken from (Matsumoto et al., 2019)

Figure 2.3 shows hybrid integration of an indium phosphide-semiconductor optical amplifier (InP-SOA) gain chip on silicon photonics platform. In this research, a 4-ch SOA array was integrated to a 4×4 Si switch to obtain inline optical amplification.

Though FCB technology is the most used technique for active components alignment, the issue of bonding alignment is the major challenge (Franck Chollet, 2016). Many fabrication dependent parameters determine the vertical and lateral alignment accuracy. For example, the vertical alignment accuracy depends on the accuracy of the etching processes, thickness tolerance of the deposited layers and bonding force. Lateral alignment accuracy is caused by offset angle due to rotation caused by thermal drift of the chip during bonding (Fitsios et al., 2014). The conventional SOAs are normally cleaved with tolerances in the range of ±5 μm, which results in having ≥ 5 μm gap between each facet of the SOAs and the mating silicon photonic waveguides (Budd et al., 2015). This causes optical losses. In another study, solder-aligned photonic chip assembly was proposed (Barwicz et al., 2018), where a standard high-throughput microelectronic tool is used to pick and place an active chip on a photonic carrier wafer. Thermal annealing of solder pads helps to self-align the waveguides of the two dies, and the alignment accuracy is controlled by vertical standoffs and lateral stops. By using a silicon mode-matching nano-taper adiabatic convertor, vertical and horizontal accuracies of 0.26 μm and 0.58 μm were achieved with a 1.1 dB optical loss. Table 2.1 summarizes some of

Table 2.1 Published works on active components alignment

Technology	Alignment accuracy (µm)			Total insertion loss (dB)	Reference
	Vertical	Lateral	Horizontal		
Flip-chip bonding	0.1	3	2.5	>10	(Fitsios et al., 2014)
Flip-chip bonding	<0.2	<3	<2	~1.5	(Budd et al., 2015)
Flip-chip bonding	0.2	1	2	<3	(Doany et al., 2016)
Flip-chip bonding	±0.5	±1	5±2	7.7	(Matsumoto et al., 2019)
Flip-chip bonding	0.26	0.58	-	1.1	(Barwicz et al., 2018)

the published works on active components alignment to waveguides in SOI chips. Alignment accuracy is usually insufficient to achieve very low insertion losses.

2.3   State of the art MEMS actuators for photonic integrated circuits

Mechanically tunable photonic devices with integrated MEMS actuators have progressed tremendously in the past three decades, where tuning of several passive silicon photonic devices such as waveguides and mirrors have become fundamental to many photonic integrated circuits (PICs) applications (Du, Chau, & Zhou, 2016). These applications range from optical telecommunications and networking (Errando-Herranz et al., 2015; Grade & Jerman, 2001; Poot & Tang, 2014), optical sensing (Takahashi et al., 2013; W. Wang, Chen, Zivkovic, Tanguy, & Xie, 2016) to optical imaging (Gora, Suter, Tearney, & Li, 2017; L. Liu et al., 2014; Luo et al., 2018). Nonetheless, only few works are available on specifically using MEMS actuators for active chip alignment.

2.3.1 MEMS actuators for active components alignment in photonic integrated circuits

Few studies on using electrothermal actuators for active components alignment were proposed by some research groups. For instance, in (Wu et al., 2016), (T.-J. Peters & Tichem, 2015), (T.-J. Peters & Tichem, 2016b), (T.-J. Peters, Tichem, & Staufer, 2014) and (T. Peters & Tichem, 2017), MEMS electrothermal actuators were used to actuate flexible suspended waveguides for chip-to-chip alignments. In these research papers, a 16 μm SiO_2 stack material of a TriPleX platform (silicon dioxide/silicon nitride (SiO_2/Si_3N_4) platform on a silicon (Si) substrate) was used. Figure 2.4 shows the schematic overview of the photonic assembly package.

In Figure 2.4, short and long loop bimorph actuators with maximum vertical deflection of 3.5 μm and 18.5 μm, respectively were reported, with a power consumption of 130 mW for the long loop actuator. In another work, (T.-J. Peters & Tichem, 2016b) presented electrothermal bimorph actuator made of polysilicon/oxide layers with power dissipation of ~50 mW and out of plane deflection of 6.5 μm, to align waveguides of two PICs. In another research by (Mu et
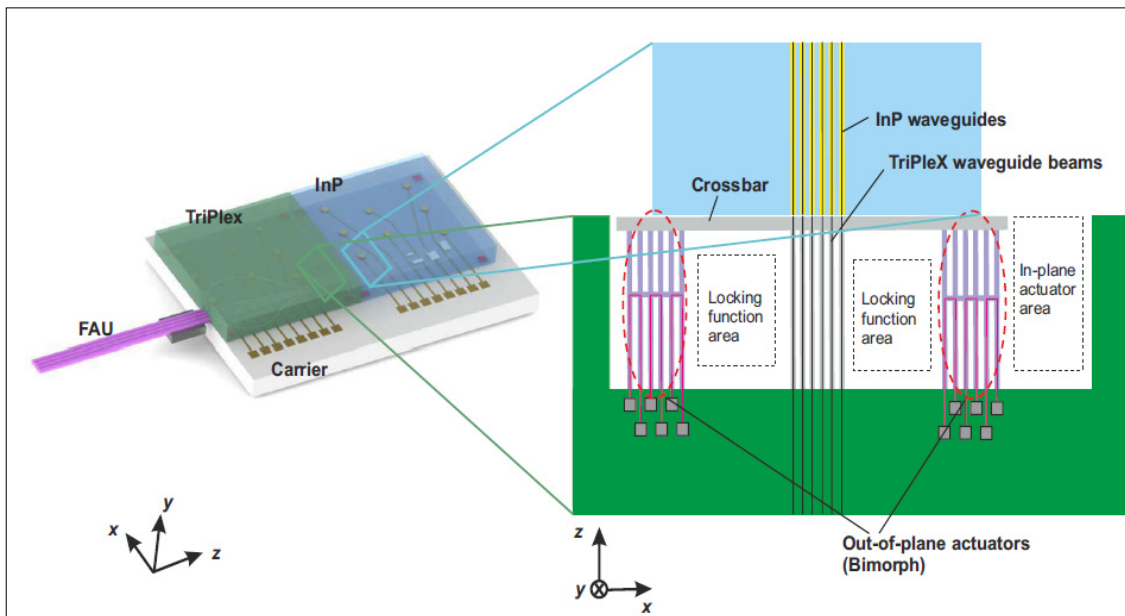
Figure 2.4 3D-schematic overview of filp-chip bonded-TriPleX and InP chips on a common carrier
Taken from (Wu et al., 2016)

Table 2.2 Summary of published MEMS actuators in photonic integrated circuits

Ref	Actuator type	Application	Actuation voltage	Displacement (μm)
(Alneamy et al., 2019)	Electrostatic	Low displacement applications	9.4 V	~ 0.63
(T. Liu, Pagliano, & Fiore, 2017)	Electrostatic	ON/OF switch	3V	0.05
(Nagai & Hane, 2018)	Electrostatic	ON/OF switch	18 V	0.424
(Amin, Huda, Tulip, & Jäger, 2015)	Electrostatic	Optical applications	130 V	282
(Wu et al., 2016)	Electrothermal	Active chip alignment	12 V	18.5
(Q. X. Zhang et al., 2010)	Electrothermal	Active chip alignment	25	50

al., 2016), a passive silicon nitride waveguide core vertical coupler was flip-chip bonded to a polymer waveguide with lateral misalignment of ±1.4 μm and optical loss of 0.8 dB. Table 2.2 summarizes some of the published papers on the MEMS actuator general applications in PICs. Broad range of applications exist, in some low displacements are required, whereas in other applications such as optical scanning that require moving MEMS mirror (Amin et al., 2015), large displacements in order of hundreds of microns are required.

CHAPTER 3

ALUMINUM NITRIDE OUT-OF-PLANE PIEZOELECTRIC MEMS ACTUATORS

Almur A.S. Rabih, Mohammad Kazemi, Michaël Ménard and Frederic Nabki

Department of Electrical Engineering, École de Technologie Supérieure, Montréal, QC H3C 1K3, Canada

3.1   Preface

This chapter contributes to an upward and downward out-of-plane actuator equipped with capacitive combs for self sensing to track the displacement of a waveguide-carrying platform. In addition, the actuator has also optical path for waveguide alignment. AASR designed, simulated and tested the devices. MK bonded the devices. MM and FN supervised the work. This single degree of freedom out-of-plane actuator has led to the development of two and three degrees of freedom actuators presented in chapter 4.

3.2   Abstract

Integrating microelectromechanical systems (MEMS) actuators with low-loss suspended silicon nitride waveguides enables the precise alignment of these waveguides to other photonic integrated circuits (PICs). This requires both in-plane and out-of-plane actuators to ensure high-precision optical alignment. However, most current out-of-plane electrostatic actuators are bulky, while electrothermal actuators consume high power. Thus, piezoelectric actuators, thanks to their moderate actuation voltages and low power consumption, could be used as alternatives. Furthermore, piezoelectric actuators can provide displacements in two opposite directions. This study presents a novel aluminum nitride-based out-of-plane piezoelectric MEMS actuator equipped with a capacitive sensing mechanism to track its displacement. This

actuator could be integrated within PICs to align different chips. Prototypes of the device were tested over the range of ±60 V, where they provided upward and downward displacements, and achieved a total average out-of-plane dis-placement of 1.30 ± 0.04 μm. Capacitance measurement showed a linear relation with the displacement, where at –60 V, the average change in capacitance was found to be –13.10 ± 0.89 fF, whereas at 60 V the change was 11.09 ± 0.73 fF. This study also investigates the effect of the residual stress caused by the top metal electrode, on the linearity of the displacement–voltage relation. The simulation predicts that the prototype could be modified to accommodate waveguide routing above it without affecting its performance, and it could also incorporate in-plane lateral actuators.

Keywords: Out-of-Plane Actuation; Piezoelectric Actuator; MEMS; Residual Stress; Aluminum Nitride;

3.3   Introduction

Photonic integrated circuits (PICs), and in particular silicon photonics, have developed tremendously over the past decade, because of the ever-increasing demand for fast and high-capacity optical communications. Nevertheless, further improvements in complexity, performance, and cost are impeded by the fact that different optical processing functions, such as light emission, modulation, filtering, switching, and detection, are best performed by devices fabricated with different materials. For instance, advanced lasers (Matsui et al., 2021; Rahim et al., 2019; Septon et al., 2019) and fast photodiodes (Nada et al., 2020; L. Zhang et al., 2022) at telecommunication wavelengths are made with III–V materials. On the other hand, recent work on integrated lithium niobate modulators indicates that they can achieve record performance (Mian Zhang, Wang, Kharel, Zhu, & Lončar, 2021). Silicon photonics, including devices made with silicon nitride waveguides, can be used to implement compact, low-loss passive (Boroojerdi, Ménard, & Kirk, 2016a; Q. Han, Menard, & Shi, 2020; Q. Han, St-Yves, Chen, Ménard, & Shi, 2019; Nair & Menard, 2021) and tunable filters (Boroojerdi, Ménard, & Kirk, 2016b), and can be monolithically integrated with electronic components (Nezami et al., 2018). Integrating components made on different chips enables devices with record-

breaking performance, as recently demonstrated with the narrow linewidth laser presented in (Jin et al., 2021), for instance. Nevertheless, misalignments between photonic and optical components are an important source of optical losses, especially when aligning active components such as laser sources and semiconductor optical amplifiers (SOAs). Despite the sub-micron accuracy of the pick-and-place tools implemented by the commonly used flip-chip bonding (FCB) technology, the issue of bonding alignment is still a major challenge (Franck Chollet, 2016), where out-of-plane and lateral in-plane misalignments were reported (Barwicz et al., 2018; Budd et al., 2015; Doany et al., 2016; Fitsios et al., 2014; Matsumoto et al., 2019). Beside the accuracy of pick-and-place tools, fabrication-dependent parameters were also found to contribute to total misalignments, where in the out-of-plane direction, maximum accuracies of only up to ±0.5 μm were achieved (Matsumoto et al., 2019). These misalignments are caused by the accuracy of the etching processes, the thickness tolerance of the deposited layers, and the bonding force (Fitsios et al., 2014). MEMS actuators combined with suspended waveguides could be a solution to resolve these alignment issues by providing dynamic alignment at low cost and within compact structures. For instance, in (Wu & Tichem, 2018), electrothermal bimorph actuators were proposed to compensate ~ 8 μm out-of-plane misalignment between the indium phosphide (InP) active chip and the silicon photonic chip.

Most used MEMS to provide out-of-plane motions include electrostatic (Sharma, Kohli, Brière, Ménard, & Nabki, 2019; Uhlig et al., 2018), electrothermal (Hussein, Fariborzi, & Younis, 2020; Si, Ding, Zhang, & Zhang, 2020), and piezoelectric (Meng Zhang et al., 2015) actuation mechanisms. The selection of the actuation mechanism depends on several factors, such as the availability of the fabrication technology, the maximum power dissipation allowed, and the maximum available voltage. Out-of-plane electrostatic actuation is performed using parallel-plate capacitors, staggered comb drives (X. Zhang et al., 2016), asymmetric combs (Bahgat, Zaki, Mohamed, & Sherif, 2018), or with vertical repulsive forces (S. He, Ben Mrad, & Chong, 2011). The staggered and asymmetric comb drive approaches need extra lithography, etch, and deposition steps during the fabrication process. For instance, multiple deep reactive ion etching (DRIE) processes are required (M. Kim et al., 2009), and in some cases the substrate is also patterned to create the lower comb drives (Manh & Hane, 2009).

Thus, they are more complex and costly (Fan et al., 2017). On the other hand, repulsive forces require upper and lower electrodes that can also be complex to fabricate in silicon-on-insulator (SOI) processes that are favored for MEMS. As electrothermal actuators consume significant amounts of power, piezoelectric actuators are preferred for low-power applications.

Typically, piezoelectric actuation is not able to provide as large out-of-plane displacements (F. Chollet & Liu, 2018) as that enabled by electrothermal actuations. Nonetheless, piezoelectric actuation provides fast response times at low voltage and with low power consumption (Piyawattanametha & Qiu, 2012). In addition, the possibility of having both up and down precise out-of-plane displacements is expected to make piezoelectric actuation a good candidate for alignment between PICs. In (Sandhu, Meade, Bi, & Smythe, 2017), a piezoelectrically driven micro-lens was used to align an optical fiber to a photonic device. The lens was placed between the fiber and photonic device and was held from the top and bottom by the actuators to move it in x, y, and z axes to maintain the optical alignment. To make piezoelectric devices, ceramics made of lead zirconate titanate (PZT) have been widely used, due to their high piezoelectric properties (S, Shinde, Kumar, & Kharat, 2012). For instance, the authors of (Zhen Qiu et al., 2010) reported a large z-axis PZT actuator for an endoscopic microscopy application. The actuator provides as high as 120 μm of displacement at 20 V. In another study presented in (Xie & Livermore, 2015), a PZT actuator with >3 μm of z-axis displacement using 170 V was proposed for high-force applications such as tactile displays and micropump applications. In (Michael, Chen, & Kwok, 2016), a dynamic PZT actuator was used to drive a micro-lens in the z-axis for miniaturized cameras, confocal microscopy, and pico-projectors. The actuator was controlled by a feedback system based on an optical displacement sensor. In another study (Z. Qiu et al., 2013), a combination of piezoelectric and electrostatic actuators was used to provide a 2D scanner to obtain vertical cross-sectional fluorescence images in an endomicroscope. A large commercial PZT-based z-axis actuator with an embedded strain gauge sensor was used to provide up to 400 μm vertical displacement, whereas an electrostatic actuator was used to provide a rotation on the second axis. As seen, PZT-based actuators, due to their high piezoelectric coefficients, provide large displacements at relatively low actuation voltages. However, PZT-based devices are difficult to use within integrated circuits (Rezaei, Lueke, Raboud, & Moussa, 2013). In addition, recently, there have

been environmental concerns about the use of lead in piezoelectric materials such as PZT (Damjanovic, 2008). Aluminum nitride (AlN) is one of the most studied non-ferroelectric piezoelectric thin films in the last decades, as its crystal is isotropic in the x-y plane but anisotropic along the z-axis (Mastronardi, 2016). AlN has been used as a piezoelectric thin film in many applications, including energy harvesters (Gablech et al., 2020), microphones (Segovia-Fernandez et al., 2017), inertial sensors (Schneider, Pfusterschmied, Patocka, & Schmid, 2020), and bulk acoustic wave resonators (Y. Liu et al., 2020). Despite the relatively low piezoelectric coefficients of AlN, it remains well suited in applications such as chip-to-chip alignment, where small out-of-plane displacements are required, due to its unique characteristics, such as its high Young's modulus, MEMS-CMOS compatibility (Meng Zhang et al., 2015), ease of deposition (Piazza, Felmetsger, Muralt, Olsson, & Ruby, 2012), and good optical properties (Li et al., 2021), which make it a good candidate for integrated photonic devices. It is also lead-free, as opposed to other piezoelectric materials such as PZT, which is a significant benefit for commercial applications.

This work presents a novel out-of-plane piezoelectric actuator to control the vertical position of a suspended platform. The actuator includes a capacitive sensing mechanism to electrically monitor its motion. The novelty of this actuator is its ability to provide positive and negative out-of-plane displacements with a sensing capability, where the sensed capacitance is linearly dependent on the displacement of the platform. The structure is also uniquely designed to be able to support an optical waveguide. The purpose of this study is to pave the way for integrated positioning systems that can provide out-of-plane dynamic alignment between different types of PICs. One of the issues faced with the current active alignment technique used to assemble optical subsystems is that the misalignments occurring after assembling and bonding the subsystems remain significant sources of optical losses. Thus, the main outcome of developing the proposed alignment system based on the piezoelectric actuation of suspended waveguides will be to provide a low-cost, high-accuracy integrated mechanism to align components built on different chips. Moreover, such integrated structures can allow for alignment adjustments during operation and not only at the packaging step. This chapter is organized as follows: Section 3.4 presents a schematic and the operating principle of the actuator along with the

simulation method used to design the devices and the fabrication process utilized to build them. Section 3.5 describes the simulations and experimental results. In Section 3.6, the results are discussed, Sections 3.7 and 3.8, respectively give results conclusions and chapter summary.

3.4   Materials and methods

This section is divided into four parts. First, the operating principle of the actuator is explained, and a schematic is presented. Then, the steps followed to design and simulate the device are outlined. The third part describes the fabrication process followed, and finally, the procedures for testing the devices are explained in the fourth part.

3.4.1   Operating principle and schematic of the actuator

The actuator is designed to be implemented on a SOI wafer, above which optical waveguides made of a silicon nitride core surrounded by a bottom and top cladding of silicon oxide could be patterned. As shown in the schematic presented in Figure 3.1, the function of the actuator is to precisely align the passive silicon nitride waveguide that lies on the platform with an optical active chip to optimize the optical coupling. Note that in our working assumptions, the active chip to couple to will be placed inside a cavity created on the SOI wafer. Thus, the range of motion of the actuator only needs to be large enough to compensate the variations in the etch depth of the cavity and in the thickness of the active chip, which are on the order of one micron or less. Since optical modes in integrated devices have dimensions of a few hundreds of nanometers, optical losses increase rapidly with misalignment, even at small values.

This actuator employs the piezoelectric effect to control the elevation of a platform that is used to emulate the waveguide carrier in a PIC. A schematic representation of the fabricated piezoelectric actuator is shown in Figure 3.1(a), whereas Figure 3.1(b) shows a version of the device that is modified to accommodate the optical waveguides in future work. Simulated results of the modified version are provided in the Discussion Section. The actuator is used to support the platform and vertically align it to a fixed test structure. This test structure, which simulates the active chip, will be aligned with the suspended waveguide in this demonstration.

The actuator consists of a central platform supported by two arms attached to two piezoelectric actuators. The two actuators are anchored to the substrate by folded beams. Each actuator
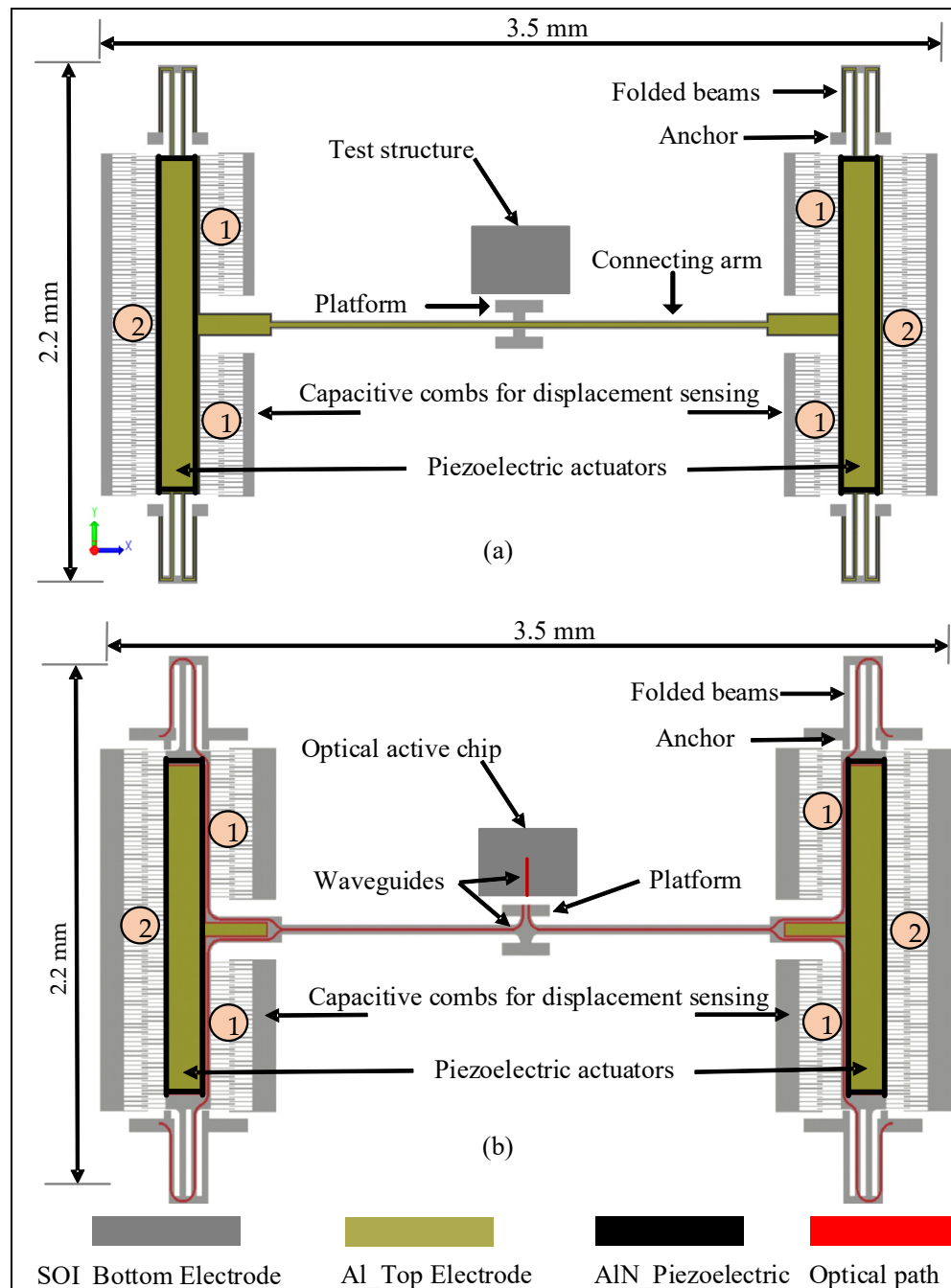
Figure 3.1 Schematic of the out-of-plane actuator: (a) the fabricated device, where the H-shape platform is aligned to a fixed test structure, and (b) a modified version (not fabricated) that accommodates waveguides on the platform for optical routing to align to an active optical chip

consists of a 0.5 μm-thick aluminum nitride (AlN) layer as the active piezoelectric material, and a 10 μm-thick silicon-on-insulator (SOI) device layer with a resistivity in the range of 1–10 Ω-cm, that is used as the device layer and as the bottom electrode. The top electrode of the piezoelectric actuator is made of 1.0 μm-thick aluminum (Al) layer, which also serves as the metal to form contact pads for electrical connections. Two sets of capacitive combs, referred to by 1 in Figure 3.1, were added to track the out-of-plane motion in the upward direction, whereas combs denoted by 2 are meant for tracking the motion in the downward direction. Separate combs were used to monitor the upward and downward motions to simplify tracking the platform displacement in the two directions of motion, since the capacitance measurements do not indicate the direction of motion.

This actuator moves in response to mechanical strain imparted by an electric field across the AlN layer, arising from a potential difference between the two electrodes sandwiching the AlN (i.e., aluminum on top and SOI on the bottom). Longitudinal and transverse piezoelectric forces create the strain that initiates the motion (Kaajakari, 2009). As shown in Figure 3.1(a), the two piezoelectric actuators are anchored by suspended folded beams and the H-shape platform is connected to these actuators through two long arms.

The direction of the platform displacement is controlled by the polarity of the applied electric field. The intrinsic electric field direction normally coincides with the positive z-axis; thus, applying a negative voltage on the top electrode generates an electric field that coincides with the intrinsic electric field, causing the upward motion. On the other hand, applying a positive voltage on the top electrode will reverse the operation, and thus the motion will be downward. The device was also designed in a way that provides the minimum stiffness in the out-of-plane direction, where the stiffness in the lateral directions is maximized by using a width to thickness ratio of 3, which is the minimum allowed by the fabrication process.

3.4.2   Design and finite element analysis simulations

The actuators were designed by taking into consideration the design rules of the commercial PiezoMUMPs process available through CMC Microsystems. As the actuators are intended to

be used for chip-to-chip optical alignment, the target displacement range was determined by the maximum out-of-plane misalignment reported with common chip integration techniques, such as flip-chip bonding, i.e., ±0.5 μm (Matsumoto et al., 2019). Therefore, the piezoelectric actuators shown in Figure 3.1 were designed to provide a displacement of 1 μm. The thicknesses of all the layers used in the PiezoMUMPs process are predefined and fixed; therefore, the displacement targets were achieved by simulating systematic variations of the lengths and widths of the actuators. Simulations showed that the optimal piezo-actuators must be 1.5 mm-long by 0.17 mm-wide. The required number and dimensions of sensing combs for a given sensing application was determined by multiple factors, including the desired sensitivity, sensing range, and fabrication constraints. Fundamentally, a higher number of comb fingers will provide a higher sensitivity and larger capacitance range. For the actuator, the number of sensing comb fingers was determined by the overall area of the piezoelectric actuator that was used to meet the 1 μm displacement target, as well as the minimum finger width and gaps allowed by the design rules (i.e., 3 μm). Therefore, the maximum number of fingers that could be used was 132 fingers for upward displacement sensing and 160 for downward displacement sensing.

The device was simulated numerically using the finite element analysis (FEA) software CoventorWare. Correct mesh sizing for the different designed parts and setting of the piezoelectric coefficients played a significant role in achieving accurate device modeling. The design and simulation of the device followed the rules of the PiezoMUMPs fabrication process provided by MEMSCAP (Cowen, Hames, Glukh, & Hardy, 2014), and the reverse piezoelectric effect mode was selected in the software to accurately model the behavior of the actuators. The piezoelectric strain was simulated with d_{31} and d_{33} piezoelectric coefficient values for AlN of −2.6 pm/V and 5.5 pm/V, respectively. The other coefficients and elastic constants used are available in (Kaajakari, 2009). It is worth mentioning that the signs of the piezoelectric coefficients were reversed from those reported in (Kaajakari, 2009), in order to obtain the displacement in the same direction observed by the measurements.

3.4.3 Fabrication process

The fabrication of this device used five masks, as per the PiezoMUMPs process (Cowen et al., 2014). As shown in Figure 3.2(a), the process started with a 150 mm n-type, double-side-polished silicon-on-insulator (SOI) wafer, with a handle layer thickness of 400 ± 5 μm.

The top surface of the silicon was doped by phosphosilicate glass (PSG) and annealed at 1050 °C for 1 h in argon, and then the PSG was removed using chemical wet etching. Then, a 0.2 μm-thick oxide layer was thermally grown and patterned using the first mask (oxide mask) through reactive ion etch (RIE) to define the ground pad and the device area where the piezoelectric material is directly attached to the 10 μm-thick SOI device layer, as shown in Figure 3.2(a) and (b). The second mask (Figure 3.2(c)) was used to pattern a 0.5 μm-thick aluminum nitride (AlN) piezoelectric layer by wet etching. The third mask (Figure 3.2(d)) was used to define a metal stack of 20 nm of chrome and 1 μm of aluminum for the pads and electrical routing, patterned using a liftoff process. With the fourth mask, the SOI layer was etched from the front side using deep RIE (DRIE), as shown in Figure 3.2(e). Thereafter, a polyimide coat was used (Figure 3.2(f)) as a front-side protection material to cover the top surface of the SOI layer, and the wafers were then flipped and back-side-etched using the fifth mask. First, RIE was used to remove the bottom thermally grown oxide, then a deep trench within the substrate back-side was patterned using DRIE, as shown in Figure 3.2(g). Finally, the devices were released (Figure 3.2(h)) by removing the buried oxide (BOX) layer using wet etching and stripping off the front-side protection polymer using a dry etching process. An optical microscope image of the fabricated devices is shown in Figure 3.3.

3.4.4 Procedures of experimental testing

Two types of tests were performed. First, the displacement of the platform and the capacitance change as a function of DC voltage applied to the piezoelectric actuator were measured. Then, frequency sweeps of the excitation were carried out and the mechanical response of the device was measured with a vibrometer to determine the resonant frequencies and their associated

modes. The movable SOI layer of the device was used as the common ground for both actuation
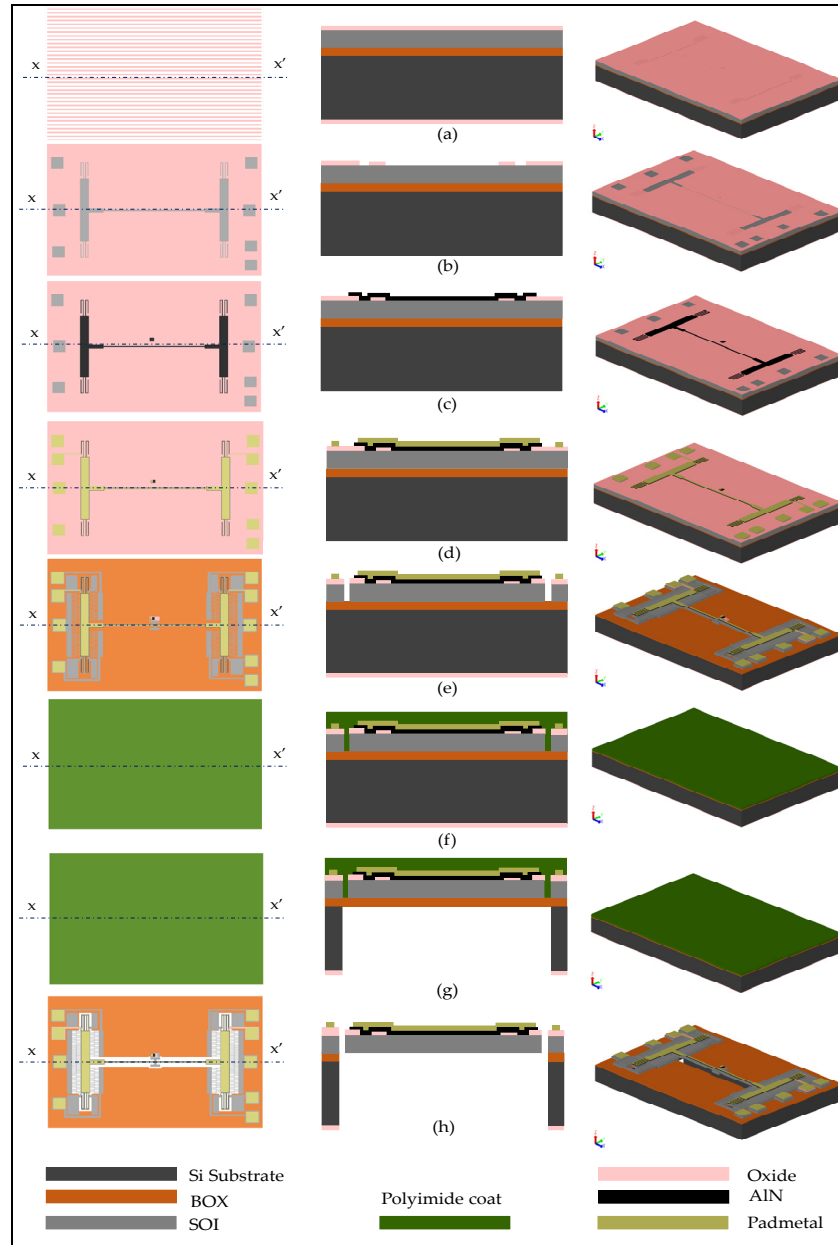
Figure 3.2 Fabrication steps of the piezoelectric actuator based on the PiezoMUMPs process: (a) the starting SOI wafer, (b) patterning thermally grown oxide layer, (c) depositing and patterning of AlN piezoelectric layer, (d) depositing and patterning of metal layer, (e) front-side etching of SOI layer, (f), front-side protection layer using a polymer layer, (g) back-side etching of handle layer, and (h) releasing the device
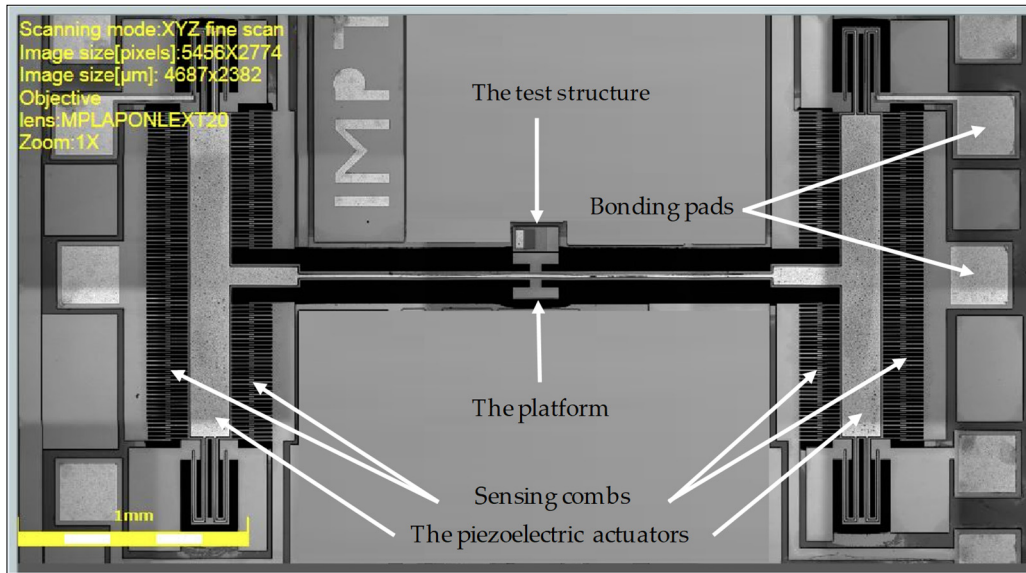
Figure 3.3 Scanning electron microscopy (SEM) image of the fabricated
MEMS device

and capacitive sensing, whereas the top Al was used as an active piezoelectric electrode. Before characterizing the device, the die was bonded on a specially designed PCB.The static displacement was characterized using a LEXT OLS 4100 laser confocal microscope from Olympus, Tokyo, Japan, whereas the capacitance was measured using an AD7747 capacitive readout circuit (Devices, 2007). The LEXT OLS 4100 provides a lateral resolution of 0.12 μm and a 10 nm height resolution, which is useful for the characterization of the out-of-plane displacement. Before using the microscope to measure the displacement of the platform, the height differences in a multilayered test structure were measured for calibration. The test structure was designed beside the platform to represent the active chip shown in Figure 3.1(b), and to facilitate the out-of-plane displacement measurements. The test structure contains the SOI device layer, oxide, and AlN and Al layers, as shown in Figure 3.4. Table 3.1 shows the average measured height differences compared to their values provided in the design rules handbook of the PiezoMUMPs process (Cowen et al., 2014). The table also includes the height differences between the top of the device layer and the oxide, the device layer and the AlN, and the device layer and the Al.
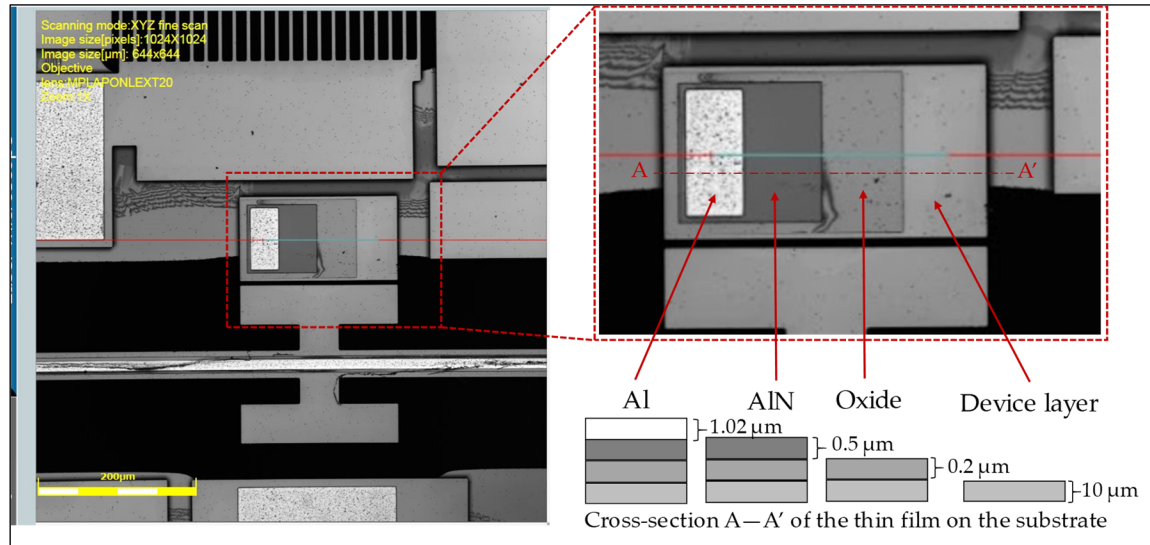
Figure 3.4 Multilayered test structure used for differential height measurements

Considering the fabrication tolerances (Cowen et al., 2014), these values are in good agreement with the expected ones. Having tested the accuracy of the microscope, before actuating the

Table 3.1 Measured height differences versus designed values

Layers	Height difference (µm)	
	Design rules value	Measured value
Device layer to oxide	0.2	0.16 ± 0.06
Device layer to piezoelectric layer	0.7	0.58 ± 0.06
Device layer to metal	1.72	1.54 ± 0.06

device, the initial deformation of the platform without an actuation voltage applied was measured against a fixed reference point, as shown in Figure 3.5. The platform was found to be below the reference point by 5.32 µm. The initial height difference between the platform and the reference point was set as the reference value to measure the displacement of the platform.
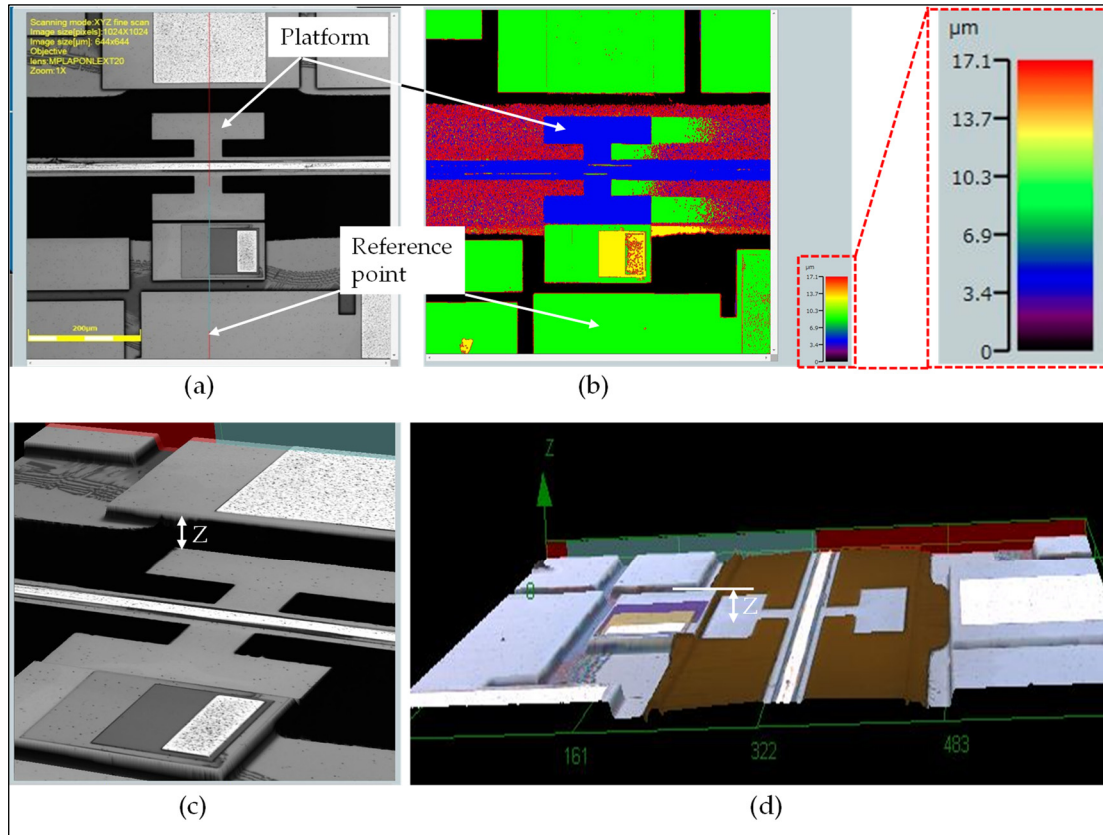
Figure 3.5 Initial deformation of the platform below the reference point due to residual stress: (a) the platform and reference measurement point, (b) color image highlighting the different levels of the platform and reference point, and (c,d) 3D pictures showing the z-axis height between the platform and the reference level

Then, a voltage in the range of −60 V to 60 V in steps of 10 V was applied to the actuators. At each step, an image was acquired and the height difference between the platform and the reference point was recorded. To find the displacement at a specific voltage, the height difference between the platform and the reference point at that voltage was calculated.

A Polytec laser doppler vibrometer (OFV2570 controller and OFV-534 laser unit) was used to determine the resonant frequency modes of the device. To excite the resonant modes, a function generator was used to apply the AC voltage signal to the electrodes of the piezoelectric actuator, and the laser beam of the vibrometer was focused onto the platform, where the reflected signal was monitored to measure its motion. An AC signal with a frequency ranging from 6 kHz to 15 kHz was applied, and a fast Fourier transform (FFT) was performed on the

vibrometer signal to identify the resonant out-of-plane modes. The first three resonant modes of the actuator identified using modal harmonics simulations are shown in Figure 3.6. All modes correspond to motion in the out-of-plane direction, despite that in the second mode the platform becomes a node, as shown in Figure 3.6(b). The first mode occurred at 7.785 kHz (Figure 3.6(a)), and the second and third modes occurred at 11.730 kHz (Figure 3.6(b)) and 12.970 kHz (Figure 3.6(c)), respectively.
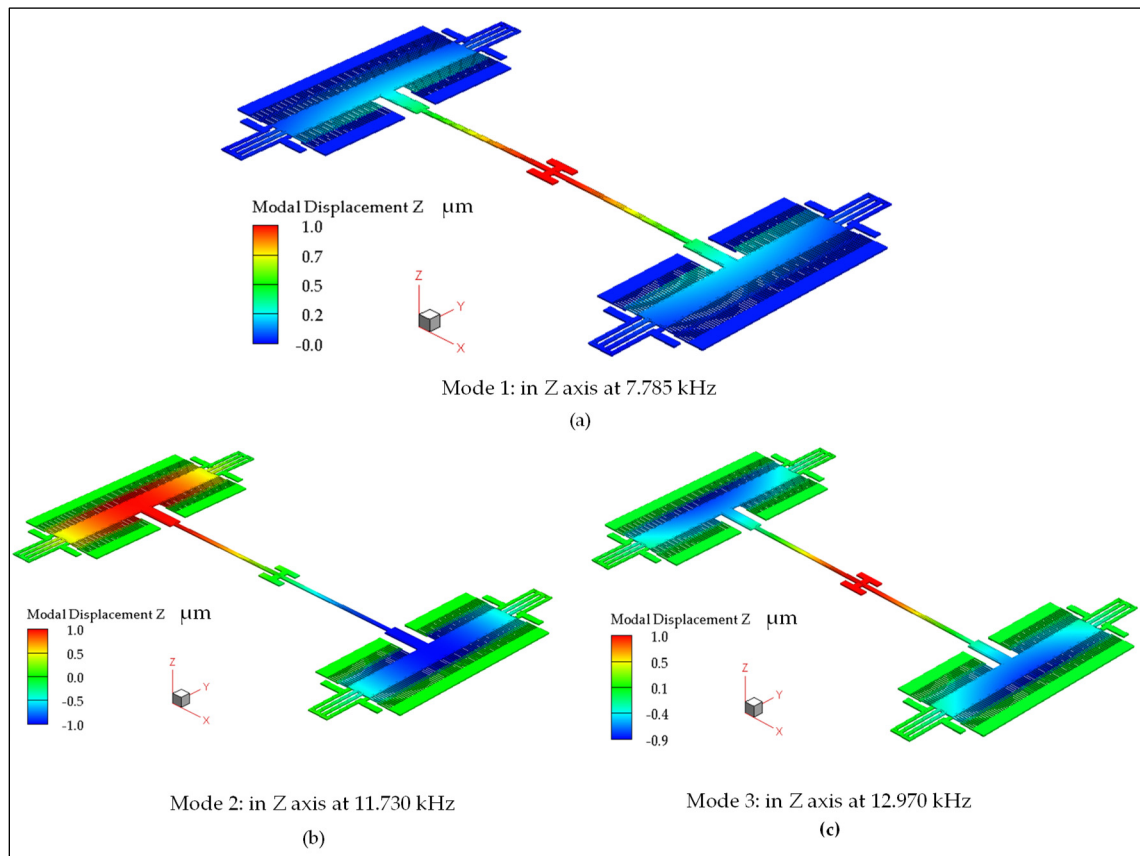
Figure 3.6 Simulated resonance frequencies showing (a) mode 1, (b) mode 2 (note: platform becomes a node), and (c) mode 3

3.5   Results

3.5.1   DC characterization

It was observed that applying negative actuation voltages to the top electrode (active electrode) caused the platform to move in the upward direction along the z-axis, whereas applying positive voltages led to motion in the downward direction. The measurement of the displacement under DC voltage excitation was performed using a confocal microscope, following the method previously described. Figure 3.7 shows microscope images of three
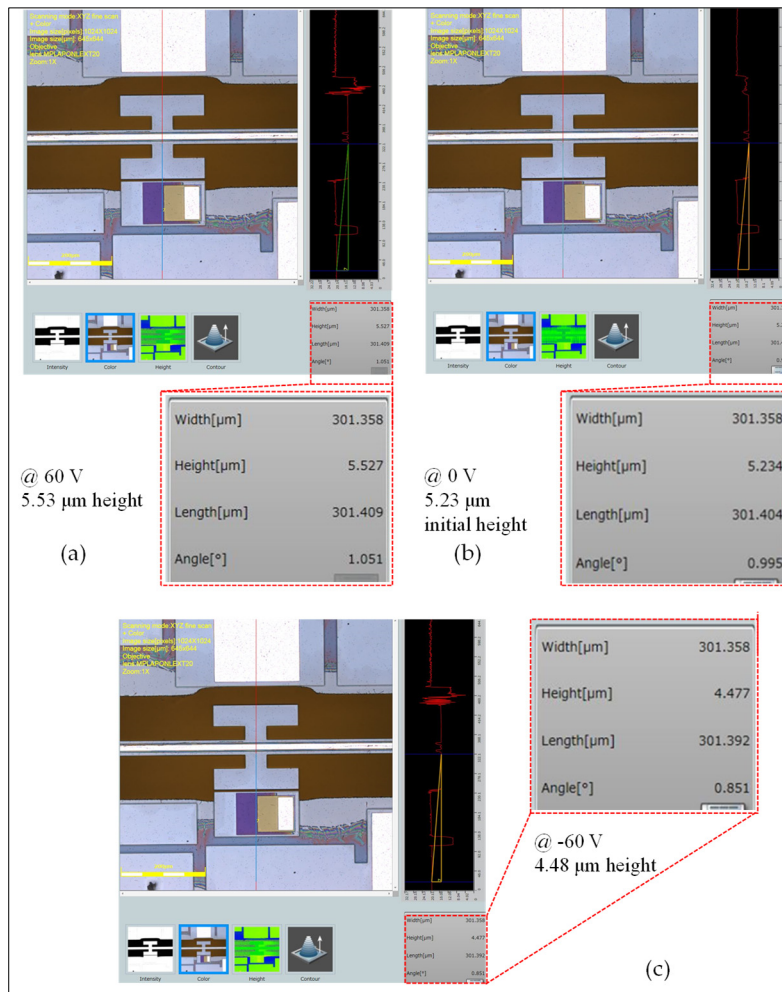
Figure 3.7 Microscope images showing the height of the platform with respect to the reference point for (a) −60 V, (b) at rest, and (c) at 60 V

measurements: at rest (0 V), maximum negative voltage (−60 V), and maximum positive voltage (60 V).

In total, three devices of the same design as the one shown in Figure 3.1(a) were tested. The devices were fabricated during the same manufacturing run but are from different dies. Throughout the following analysis, the three devices will be referred to as D1, D2, and D3. The tests were repeated five times for each device, and the averages were compared with the FEA simulation performed with the CoventorWare software, as shown in Figure 3.8. The standard deviation of the five measurement runs for each device showed small variations within ±34 nm, which demonstrates the repeatability of the measurements across the devices and dies. It is worth pointing out that the upward displacement was larger than the downward displacement at the same actuation voltage. Initial downward bending of the platform caused by tensile stress from the top metal electrode was found to be the main cause. This made the
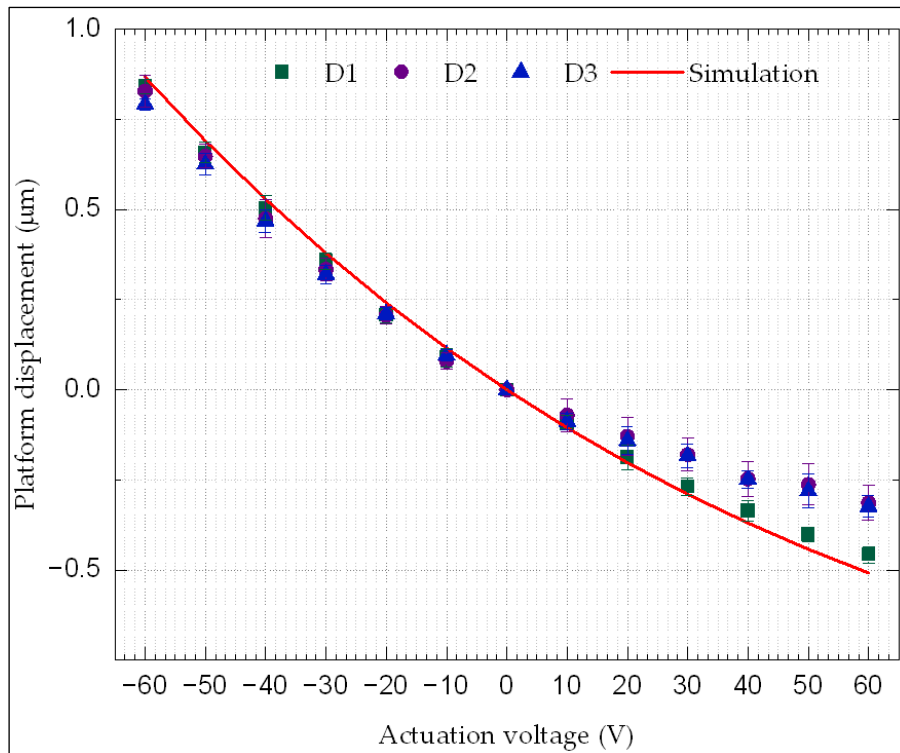
Figure 3.8 Averaged displacement for five measurement runs of three devices (D1, D2, and D3) versus the actuation voltage (the line represents the predicted behavior from the FEA simulation).

device bend downward at rest, and thus limited the linear downward displacement achieved though the positive actuation voltage. As a result, the downward displacement achieved beyond 40 V was not linear with applied voltage. For negative bias from −10 V to −60 V, the average of the positive displacement of the platform for the three devices went from 0.09 ± 0.03 µm (0.12 µm for simulations) to 0.82 ± 0.03 µm (0.87 µm for simulations). On the other hand, for the positive bias from 10 V to 60 V, the average of the negative displacement of the platform went from -0.08 ± 0.03 µm (−0.11 µm for simulations) to -0.36 ± 0.03 µm (−0.51 µm for simulations). The results and the effect of the stress will be discussed in the Discussion.

The capacitance of the comb fingers denoted by 1 in Figure 3.1(a) was recorded as a function of the displacement in the upward direction, whereas for downward displacements, the change in the capacitance was monitored using comb fingers denoted by 2 in Figure 3.1(a). The capacitance changes in a device measured with the AD7747 and the simulated values are shown in Figure 3.9, versus the actuation voltage. Note that the capacitance was measured on
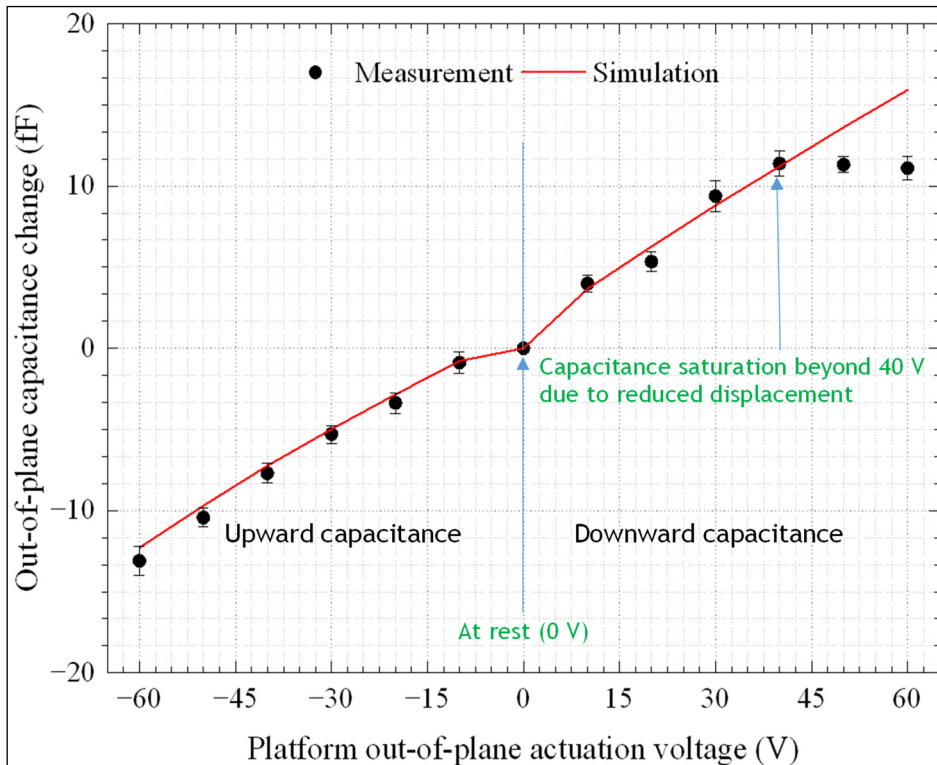
Figure 3.9 The average DC capacitance change versus the actuation voltage measured over five runs and the simulation results

an unpackaged bare die of the same design for a single device. This was needed in order to accurately measure the comb drive capacitances using the read-out circuit. The device was tested with a probe station (EP6 from Cascade) to minimize the effect of the parasitic capacitances of the read-out circuit caused by the wire-bonds, package, and test PCB used to achieve the displacement measurements previously presented.

For the entire actuation range in the upward direction and for voltages below 40 V in the downward direction, the actuator had a linear behavior. Beyond 40 V in the downward direction, the saturation in the capacitance was due to the reduced displacement caused by the nonlinear behavior, as explained above. At −60 V, the average change in capacitance over five runs was found to be −13.10 ± 0.89 fF (−12.29 fF for simulation), whereas at 60 V the change was 11.09 ± 0.73 fF (15.92 fF for simulation). Since the purpose of measuring the capacitance is to track the displacement of the platform, the capacitance change of this device was compared to the corresponding average of the average out-of-plane displacements of D1, D2, and D3, where the capacitance was found to decrease by increasing the out-of-plane displacement of the platform. For the downward displacement, at the maximum platform displacement of −0.36 ± 0.03 μm, the average capacitance change over five runs was 11.10 ± 0.74 fF (15.92 fF in simulations), whereas in the upward direction, the average measured capacitance change at the maximum platform displacement of 0.82 ± 0.03 μm was −13.10 ± 0.89 fF (−12.29 fF in simulations).

3.5.2   Mechanical frequency response

Figure 3.10 shows the mechanical frequency response extracted from D1 by using the vibrometer-based method previously discussed. The vibrometer was able to capture the first and the third modes at 7.841 kHz and 13.586 kHz, respectively. As shown in the simulation results presented in Figure 3.6(b), in the second mode at 11.730 kHz, the platform of the actuator is a node that exhibits no out-of-plane displacement discernable by the vibrometer. Thus, only the first and the third modes can be measured by the vibrometer. Table 3.2 shows the measured resonant frequencies of all three devices in comparison with simulations.
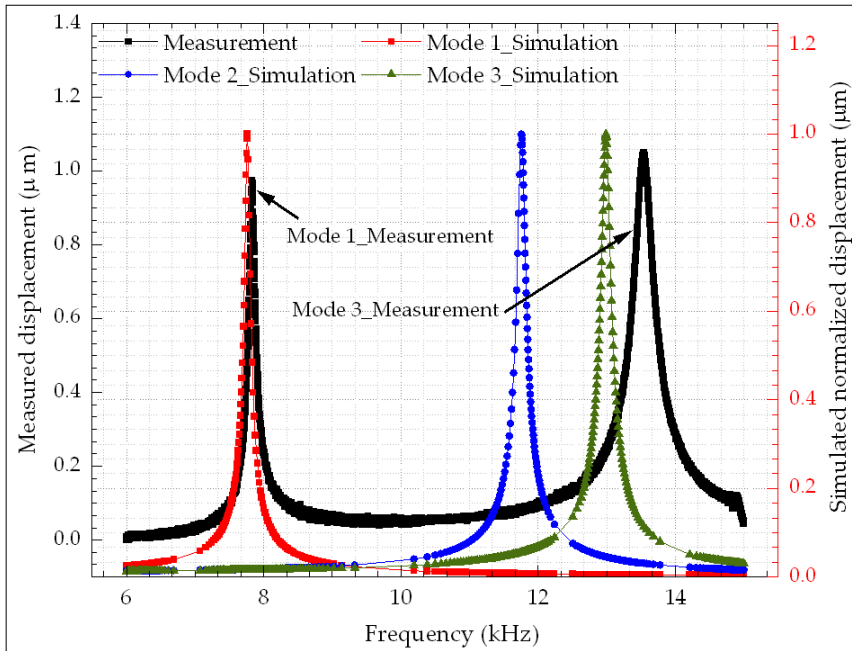
Figure 3.10 Measured frequency response of D1 showing two
resonant modes along with the simulation results

3.6   Discussion

Three devices from three different dies were tested and the results were compared to the FEA

Table 3.2 The measured resonant frequency modes of the devices

Die	Resonant frequency (kHz)		Error %	
	Mode 1	Mode 3	Mode 1	Mode 3
D1	7.841	13.586	0.714	4.534
D2	7.992	13.772	2.590	5.823
D3	7.722	13.492	0.816	3.869
Simulation	7.785	12.970		

simulations carried out using the CoventorWare software. As shown in Figure 3.8, the results

of all devices showed good agreement, especially for negative actuation voltages. However, D1 provided the closest results to the simulations compared to the other two devices. At −10 V, the simulations predicted a displacement of 0.12 μm, but the average measurement over five cycles for each of the three devices (i.e., D1, D2, and D3) yielded 0.09 ± 0.03 μm, 0.08 ± 0.02 μm, and 0.10 ± 0.02 μm, respectively, resulting in average differences of 22.3%, 30.9%, and 17.3%, respectively. At the maximum applied negative voltage of −60 V, a displacement of 0.87 μm was simulated versus the measurement of 0.84 ± 0.02 μm, 0.83 ± 0.02 μm, and 0.79 ± 0.04 μm, for D1, D2, and D3, respectively, with percentage errors of 3.0%, 4.5%, and 8.7%, respectively. For positive voltages, at 10 V, the simulation yielded a displacement of −0.11 μm, whereas the measurement was −0.09 ± 0.02 μm, −0.07 ± 0.02 μm, and −0.09 ± 0.04 μm for D1, D2, and D3, respectively, leading to differences of 11.0%, 32.7%, and 17.0%, respectively. At the maximum applied positive voltage of 60 V, the simulation yielded −0.51 μm versus −0.46 ± 0.02 μm, −0.31 ± 0.03 μm, and 0.32 ± 0.05 μm for the measurement for D1, D2, and D3, respectively, and hence the differences were 9.9%, 38.2%, and 36.3%, respectively. Compared to actuators made of materials with higher piezoelectric coefficient, e.g., PZT (S. H. Chen, Michael, & Kwok, 2018), the 60 V required to provide um-level actuation on AlN piezoelectric actuators is relatively high. Nevertheless, it remains below the breakdown voltage, which is estimated to be 200 V (breakdown voltage: 4 MV/cm) (An, Men, Xu, Chu, & Lin, 2005).

Residual stress was found to have a significant impact on displacement in simulations, and as such, it is understood to be the main cause that led D2 and D3 to show larger differences to simulations than D1. Experiments showed that while D1 had a −5.31 ± 0.01 μm platform initial deformation with respect to the reference point shown in Figure 3.5, D2 and D3 showed −7.75 ± 0.40 μm and −7.67 ± 0.05 μm, respectively. The simulated results were obtained at a residual tensile stress of 165 MPa on the metal layer, which resulted in an initial simulated deformation (−5.25 μm) of the platform at 0 V. This matches rather closely the value measured for D1 at rest. Positive displacements caused by negative actuation voltages were always higher than negative displacements caused by the positive actuation voltages. For instance, in Figure 3.8,

simulations showed that the platform can move by 0.87 μm with a −60 V bias. However, when −60 V was applied to the actuator, the maximum displacement was only −0.51 μm. Two factors can explain this phenomenon: the residual tensile stress applied to the device and the variation in the thickness of the layers (mainly the electrodes) on top of the structure. The former is expected to have the most significant impact. The residual stress is caused by mismatch either in the thermal expansion coefficients of the different layers, or in the lattice constants of the layers (Mastronardi, 2016). To show the effect of variations in the residual stress on the performance of the device, different levels of both compressive (C) and tensile (T) stresses were simulated by applying the stress on the metal layer that was used as the top electrode. The effect of stress was studied over the same actuation voltage range (±60 V) used experimentally. The correlation factor of the displacement–actuation voltage relation was extracted for each stress level. Simulations showed that the nonlinearity between the displacement and the actuation voltage increased with an increase in the stress level, as shown in Figure 3.11.
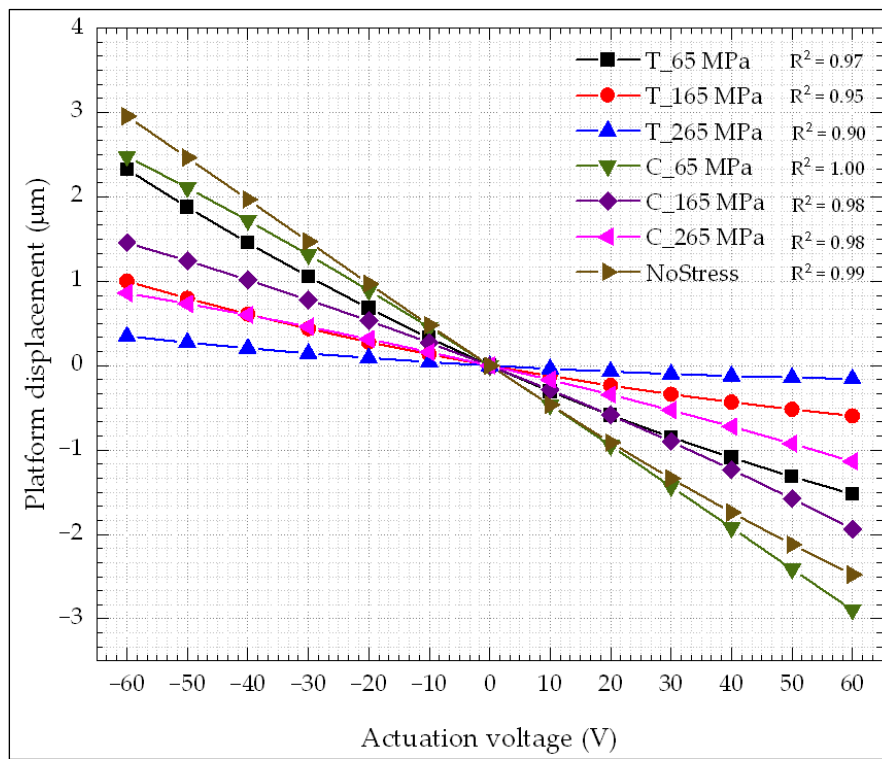
Figure 3.11 Effect of the stress on the linearity of the response of the actuator

Stress levels in a range of ±265 MPa were investigated. For compressive stresses, the linearity coefficients were found to be ~ 1, 0.98, and 0.98 for stress levels of 65 MPa, 165 MPa, and 265 MPa, respectively, whereas for tensile stresses, the linearity coefficients were found to be 0.97, 0.95, and 0.90 for stress levels of 65 MPa, 165 MPa, and 265 MPa, respectively. On the other hand, the model without stress in any materials showed a linearity coefficient of 0.99. Tensile stress had a stronger effect on the linearity of the relation between the displacement and the actuation voltage than compressive stress. For the case of tensile stress, the displacement for positive actuation voltages was lower than the one obtained with negative actuation voltages, as proven by the experiments for all the tested devices. This is explained by the fact that under tensile stress, the beams that support the platform bend downward. Simulations predicted this fact, and this was confirmed during testing by the fact that the platform was below the level of the reference point in Figure 3.5. Positive actuation voltages caused the beam to move further downward, as explained in Section 3.5. Thus, the beam may already be approaching the limit of its elasticity. On the other hand, negative actuation voltages caused the beam to move in the opposite direction to the one caused by the residual stress. Hence, the displacement was higher, as demonstrated by both simulation and experimental results. It is worth mentioning that the piezoelectric layer could also be hosting stress. A compressive residual stress of ~ −46.3 ± 0.66 MPa was measured in aluminum nitride films in (Mastronardi, 2016). However, depending on the film deposition conditions, such as the temperature and pressure, the residual stress may vary, and can be as high as 600 MPa (Mahameed et al., 2008). Besides stress, other factors could also contribute to the variations in results. Such factors include the accuracy of the measurement tools, the fabrication tolerances, and possible variations in the piezoelectric coefficients used, in addition to variations in material properties such as density, Young's modulus, and the coefficient of thermal expansion. The relation between the capacitance of the sensing combs and the actuation voltage was found to be linear. This could enable a simple feedback control circuit to track the motion of the platform.

As presented, the aim of the fabricated devices is for their use as a waveguide positioner for active chip alignment. Thus, the modified version that has an optical path included for

waveguide routing shown in Figure 3.1(b) was simulated and the results are compared in Figure 3.12 to the fabricated version previously discussed. The modified version has less piezo-material and metal area deposited on top of it, to make room for routing the waveguide.

Simulations indicate that the modified version of the device under a tensile stress of 100 MPa in the metal layer will provide the same performance as that of D1 at 165 MPa. Thus, the net residual stress of the modified version is expected to be reduced. Nonetheless, the waveguide is expected to also have an impact on the overall stress on the device and this will be characterized in future work.

As in-plane displacements are also required for the efficient waveguide positioning and chip-to-chip alignment, the width of the horizontal connecting arms could be reduced to integrate in-plane actuators in the future work.

Comparing our devices with the published works, despite the extensive use of piezoelectric transducers in several applications, including energy harvesters (Gablech et al., 2020), microphones (Ullmann, Bretthauer, Schneider, & Schmid, 2023), inertial sensors (Gabrelian, Ross, Bespalova, & Paulasto-Kröckel, 2022), and bulk acoustic resonators (Y. Qu et al., 2023),
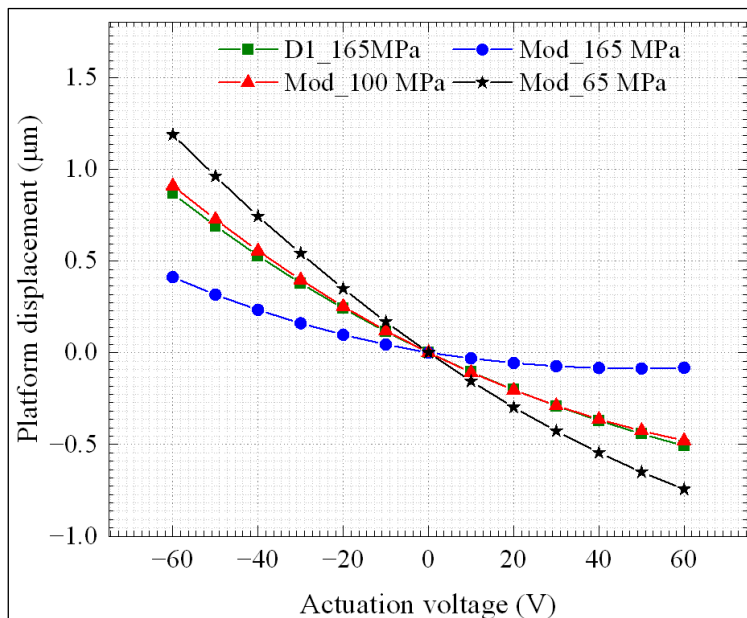
Figure 3.12 Out-of-plane displacement of the platform of the modified (Mod) version, including optical waveguides with different residual stresses compared to the fabricated devices (D1)

to the best of our knowledge, there are no works focusing on the PIC waveguide alignment application. The only report found for PICs' alignment was presented in (Sandhu et al., 2017) to align an optical fiber with a photonic device. In that work, a ball lens controlled by piezoelectric actuators was placed between the fiber and the photonic device to maintain the optical alignment. Only a few demonstrations of piezoelectric-actuated optical systems were surveyed in the literature, but they were built for different applications. For instance, the authors of (Jiang et al., 2020) used a AlN nano-bender piezoelectric actuator in a photonic crystal cavity for optical resonance tuning on nanometer scales. In (Ghosh, 2015), an acousto-optical modulator controlled through an AlN actuator was demonstrated. Work in (Stanfield et al., 2019) demonstrated phase and amplitude modulators in silicon nitride photonics controlled with an AlN actuator. Table 3.3 summarizes some of the works published on MEMS piezoelectric actuators used for different applications. As shown in the table, majority of the reported applications require displacements in the nanometer scale. Thus, actuators having sizes of hundreds of nanometers to a few micrometers were reported. The actuators in our proposed waveguide positioners for chip-to-chip alignment require the use of larger structures to support suspended waveguides and allow for a sufficient range of out-of-plane motion.

Table 3.3 Performance of published MEMS actuators for waveguide alignment

Application	ActuationVoltage (V)	Displacement (μm)	Reference
RF switch	25	0.65	(Mahameed, Sinha, Pisani, & Piazza, 2008)
Logic applications	6	0.12	(Sinha et al., 2009b)
General use	120	0.21	(Krupa, 2009)
Low-power logic	6	0.07	(Sinha et al., 2009a)
Phase shifting	2	1.25×10^{-4}	(Stanfield, Leenheer, Michael, Sims, & Eichenfield, 2019)
Tuning optical resonance	3	0.18	(Jiang et al., 2020)
Alignment	60	1.30	This work

3.7   Conclusions

This work presented a novel out-of-plane aluminum nitride piezoelectric MEMS actuator. Testing the fabricated device at voltages ranging from −60 to 60 V yielded a maximum travel range of 1.30 ± 0.04 μm. The device is equipped with a capacitive sensing mechanism to track its displacement, where the measured capacitance has shown a linear relation with the displacement. Frequency sweeps of the input signal yielded mechanical resonance frequency modes close to the simulated values performed by FEA modeling. The effect of residual stress was also investigated, where measurements and FEA simulations were matched to quantify the stress on the fabricated devices. Tensile stress influenced the performance of the devices and caused the displacement to be nonlinear with respect to the actuation voltage. The initial investigation showed that larger dimensions (length and width) are required to increase displacement, however, this will increase the impact of residual stress, and hence increase the bending of the device that causes the nonlinearity. Thus, future work will investigate the effect of the geometry of the device on its response. In addition, in-plane actuators and waveguides on top of the suspended platform will be integrated.

3.8   Summary of the chapter

This chapter introduced our initial design of a positioner, which utilizes a single degree of freedom (1DOF) piezoelectric actuator for z-axis movement, complemented by a displacement sensor. Recognizing the need for greater control to effectively address misalignments within PICs, subsequent chapters will detail the evolution of this design into more sophisticated ones. Specifically, we will present enhancements to the original 1DOF setup through the integration of electrostatic actuators, culminating in the development of two and three degrees of freedom (2DOF and 3DOF) hybrid piezoelectric-electrostatic positioners. These advanced positioners will also incorporate capacitive displacement sensors, enabling precise monitoring of the motion of platforms that carry optical waveguides, thereby facilitating improved alignment and coupling efficiency in PICs.

CHAPTER 4

MULTI-DEGREES OF FREEDOM MEMS ACTUATORS AS WAVEGUIDE POSITIONERS

Almur A. S. Rabih, Student member, IEEE Seyedfakhreddin Nabavi, Member, IEEE, Michaël Ménard, Member, IEEE and Frederic Nabki, Member, IEEE

4.1 Preface

This chapter presentes 2DOF and 3DOF versions of the single degree of freedom actuator described in chapter 3. Both actuators use a self-sensing mechanism using comb fingers to track the displacement of the waveguide-carrying platform. AASR designed, simulated and tested the devices. MM and FN supervised the work. Chapter 5 which follows this chapter is a continuation of the 3DOF actuator presented here, by using pure electrothermal means.

4.2 Abstract

This work presents novel multi degrees-of-freedom (DOF) actuators based on piezoelectric and electrostatic actuation to generate both in-plane and out-of-plane motions, intended to position a suspended optical waveguide for chip-to-chip alignment in photonic integrated circuits. In this context, the mechanical structures of the actuators with a suspended platform to carry the waveguide, are designed to house aluminum nitride (AlN) as the piezoelectric material for generating out-of-plane motion and a comb-drive, whose fixed and moveable fingers are positioned on the same layer for in-plane motion. Two distinct designs, i.e., a 2-DOF design with motions along the z-and y-axes and a 3-DOF design with motions along the z-, y-, and x-axes were fabricated and tested. Both designs include capacitive-based displacement sensors to track the motions in z-and y-axes. Experimental results at ±60 V

indicate that 3 devices of each design give an average displacement of 3.16 ± 0.34 μm and 0.63 ± 0.04 μm in the z-axis for the 2-DOF and 3-DOF designs, respectively. For the y-axis at 120 V, the average results for the two designs respectively were found to be 3.06 ± 0.17 μm and 7.38 ± 0.29 μm, with the ability to extended the later to 10.69 μm at 140 V. In the x-axis, the 3-DOF design can produce total of 300 nm of displacement at ±100 V. The capacitance measurements were found to correlate well with the tracked displacement. Furthermore, simultaneous activation of more than one actuator could mitigate misalignment and align the platform with a fixed surface.

Index Terms— Actuators, hybrid actuation, piezoelectric, electrostatic, MEMS, Aluminum Nitride (AlN), out-of-plane actuation, displacement measurement.

4.3 Introduction

Photonic integrated circuits (PICs) have reached a remarkable level of integration, with thousands of components on a chip (Takabayashi et al., 2021a). However, certain functional blocks require different materials. For instance, passive photonic devices such as phase shifters (Y. Kim, Han, Ahn, & Kim, 2021), resonators (Ding, Sun, Li, & Shi, 2023), switches (Barazani et al., 2023) and filters (Nezami et al., 2018) are fabricated on silicon substrates due to the great advantages provided by silicon, such as compatibility with complementary metal oxide semiconductor (CMOS) integrated circuits (ICs) (Nezami et al., 2018) and low cost. However, advanced lasers (Matsui et al., 2021) and fast photodiodes (L. Zhang et al., 2022) operating at telecom wavelengths are still typically fabricated with III-V materials. The integration of different chip technologies enables devices with record performance, as demonstrated by recent work on integrated lithium niobate modulators (M. Zhang et al., 2021), and the ultra-high Q resonance achieved in a narrow linewidth laser (Jin et al., 2021).

In order to enable the integration of the different chip technologies to drive down the cost of advanced optical systems, efficient co-packaging or heterogenous integration of active and passive PICs and electronics is needed. Currently, the most common strategy for integrating passive photonic components with active devices, such as laser sources and semiconductor

optical amplifiers (SOAs), is hybrid integration based on wafer bonding and flip-chip bonding (FCB). For example, work in (Carrara et al., 2017) used wafer bonding to integrate indium phosphide (InP)-based distributed feedback (DFB) lasers on a silicon photonic (SiPh) platform, whereas the work in (Marinins et al., 2023) presented FCB technology to integrate pre-tested DFB laser chips onto a SiPh platform. Despite the fact that FCB allows for integration of fully processed and tested devices, out-of-plane and in-plane misalignments between the integrated photonics components remain an important source of optical losses (Matsumoto et al., 2019). On the other hand, with wafer bonding, since the integration occurs prior to testing, it is not possible to recognize and replace non-functional components a priori, causing costly yield losses (Z. Zhou et al., 2023). Monolithic integration is another heterogeneous technique that requires no stringent micro-assembly alignment. However, monolithic integration typically suffers from less efficient laser light coupling to silicon photonic waveguides (Wei et al., 2023). Therefore, there is a need to tackle the challenging issue of misalignments when co-integrating fully processed high-performance chips.

Microelectromechanical Systems (MEMS) actuators integrated with suspended silicon optical waveguides can provide high accuracy alignment at low cost in complex PICs thanks to batch fabrication. The literature is rich with different actuation principles, namely, electrostatic (Sharma et al., 2019), electrothermal (Hussein et al., 2020), and piezoelectric (Meng Zhang et al., 2015) which, however, often have limitations in the number of degrees of freedom (DOF) they allow. Accordingly in this work, a combination of electrostatic and piezoelectric techniques is proposed to achieve both in-plane and out-of-plane displacements with low power consumption. Previously, the authors demonstrated an out-of-plane piezoelectric actuator (Rabih, Kazemi, Ménard, & Nabki, 2023) with a suspended platform designed to receive an optical waveguide that was able to provide 1.3 μm of out-of-plane displacement, which is sufficient to compensate the typical misalignments encountered in current integration schemes; i.e., ±0.5 μm (Matsumoto et al., 2019). To enhance the versatility of the previously proposed out-of-plane actuator, an additional in-plane motion capability was incorporated by integrating a set of electrostatic comb-drives. Consequently, the hybrid piezoelectric-electrostatic MEMS actuator proposed in this study utilizes electrostatic actuation for in-plane

motion and piezoelectric actuation for out-of-plane motion, enabling movement along the x-, y-, and z-axe.

As a result, the proposed hybrid MEMS actuators, when integrated with suspended beams that are able to carry optical waveguides, can provide an accurate integration mechanism to align these waveguides with components built onto other chips, such as lasers and SOAs. Advantageously, such an alignment technique can be performed not only during packaging, but also during operation.

This chapter is organized as follows: sections 4.4 and 4.5 describe the actuators and their fabrication. Sections 4.6 and 4.7 describe the test methods and experimental results. Section 4.8 discusses the results, and is followed by a conclusion and summary of the chapter.

4.4 Design and Finite Element (FE) Simulations

Two MEMS actuators designs with the capability of bearing optical waveguides on their structures are proposed and illustrated in Figure 4.1. Figure 4.1(a) shows a 2-DOF design, i.e., out-of-plane displacement along the z-axis and in-plane displacement along the y-axis. Figure 4.1(b) shows a 3-DOF design that additionally allows for motion along the x-axis.

Both designs contain a suspended platform anchored at four distinct points. Three points are attached to folded beams by connecting beams and actuators, whereas the fourth point of the platform is anchored through a quasi-serpentine silicon beam, labeled as the optical path, to accommodate and route optical waveguides and align them to those of active chips. Note that the active chip in Figure 4.1(a) is only shown for illustration, as this work focuses on the actuator structure. To close the gap between the platform and the active chip and finely tune the position of the optical waveguides, combinations of several types of springs and beams with hybrid-piezoelectric-electrostatic actuations were used. Figures 4.1(c) and (d) provide schematics of the comb drives used.

The devices were designed and simulated using finite element analysis (FEA) with the CoventorWare software (Coventor, Raleigh, NC, USA) following the design rules of the PiezoMUMPs fabrication process (Cowen et al., 2014). The design procedure begins by

importing materials properties into the database and modeling the fabrication process by providing the thickness, and order of the layers and of the processing steps. The 2D layout tool
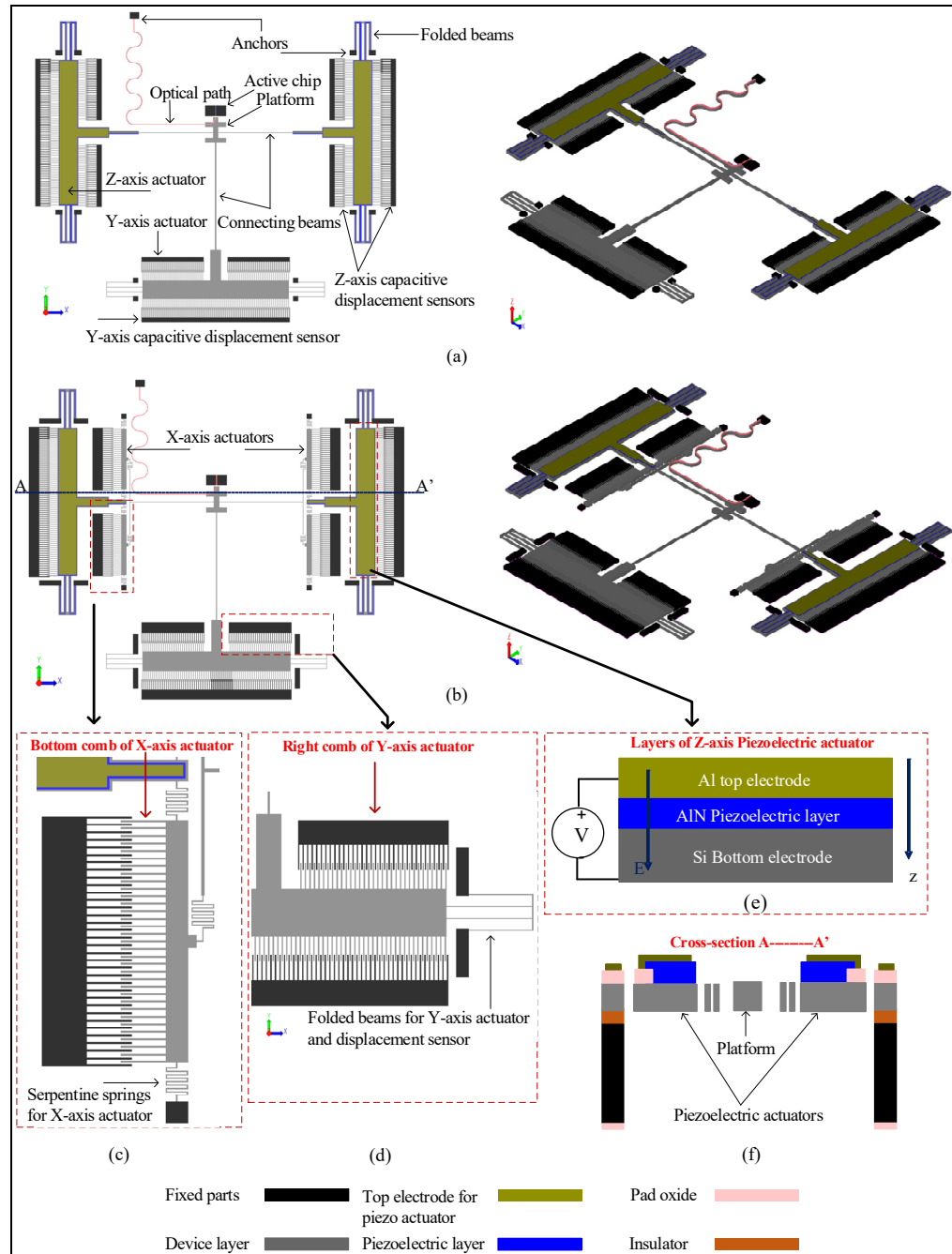
Figure 4.1 Schematic of the two actuator designs: (a) 2-DOF, and (b) 3-DOF, (c) bottom comb-drive of the x-axis actuator of the 3-DOF design, (d) right comb-drive of the y-axis actuator, (e) layers of thez-axis piezoelectric actuator, and (f) cross-section A---A' of the 3-DOF design

is then used to draw the designs, and 3D models are built from the information provided by the process and the layout. The meshed models with properly defined boundary conditions are then solved with mechanical, piezoelectric and coupled electromechanical solvers to determine the mode shapes, displacements and capacitances. The solvers provide tabulated data, and 2D and 3D graphs. The displacement components in the z-, y- and x-axes from the center of the platform are extracted, and the capacitances are determined directly from the fixed combs, as the device layer is used as a common ground among all the actuators and capacitive sensors. discussed.

4.4.1 Out-of-plane actuators along the z-axis

To generate out-of-plane displacements along the z-axis, each design uses two piezoelectric actuators. As shown in Figure 4.1, the actuators are connected to the platform through connecting beams. Each actuator consists of an aluminum nitride (AlN) piezoelectric layer sandwiched between the silicon (Si) device layer, which is also used as the bottom electrode, and an aluminum (Al) layer used as the top electrode, as shown in Figure 4.1(e). By applying a voltage difference (V_p) between the top and bottom electrodes, an electric field (E) is generated causing a transverse piezoelectric force (F_p) that is proportional to the applied voltage as given by (Kaajakari, 2009):

$$F_p = (d_{31} A_p V_p)/t_p \qquad (4.1)$$

where d_{31} is the transverse piezoelectric coefficient, A_p is the area of the piezoelectric actuator and t_p is the thickness of the piezoelectric material. The direction of the platform displacement is controlled by the polarity and the directionality of the applied electric field. In this work, the intrinsic electric field direction coincides with the positive z-axis; thus, applying a positive voltage on the top electrode generates an electric field that opposes the intrinsic electric field, causing the downward motion of the actuators. On the other hand, applying a negative voltage on the top electrode will reverse the operation, and thus the motion will be upward.

4.4.2 In-plane electrostatic actuators in the y and x axes

To generate in-plane displacements along the y- and x-axes, both designs use capacitive comb-drives. The x-axis actuators have four sets of combs, two combs for the −x-axis and two combs for the +x-axis. Figure 4.1(c) shows the lower comb of the −x-axis actuator. The y-axis actuator consists of two combs, i.e., the left and right combs, as shown in Figure 4.1(d). The actuators are made using the silicon device layer, and the generated electrostatic force is given by (Shkel, 2009):

$$F_e = -(N\varepsilon_0 tV_e^2)/g \tag{4.2}$$

where V_e is the bias voltage, N is the number of moving fingers, ε_0 is the permittivity of free space, t is the thickness of the fingers, and g is the gap between the moving and fixed fingers. These parameters influence the travel range of the actuators by determining the maximum allowable voltage that does not cause pull-in of the moving fingers toward the fixed ones. For instance, for the actuation in the y-axis, the maximum voltage that causes side instability is determined by the following (Legtenberg, Groeneveld, & Elwenspoek, 1996):

$$V_{max} = \frac{d^2 k_y}{2\varepsilon_0 bN}\left(\sqrt{2\frac{k_x}{k_y} + \frac{y_0^2}{d^2}} - \frac{y_0}{d}\right) \tag{4.3}$$

where k_y is the y-axis stiffness, b is the width of the comb fingers, k_x is the stiffness in x-axis, y_0 is the overlap between the moving and fixed fingers, and d is the fingers spacing. To maximize the displacement in y-axis, the stiffness in x-axis should be very small compared to that of the y-axis.

4.4.3 Capacitive displacement sensors

To track the displacement of the platform, three sets of capacitive combs were added. For the 2-DOF design, as shown in Figure 4.1(a), six combs are used to track the z-axis displacement, four track upward displacements and the other two track downward displacements. On the

other hand, for the 3-DOF design, four capacitive sensor combs were removed to accommodate the x-axis actuators, and therefore only two sensor combs were left to track both upward and downward displacements, as shown in Figure 4.1(b). Two separate sensors were used to monitor the upward and downward motions separately in the case of the 2-DOF design to simplify the tracking of the platform since the capacitance measurements do not indicate the direction of motion when the moving and fixed combs are well aligned. However, since both designs suffer from stress that creates an imbalance in the overlap area of the comb sensors, only one comb is needed to monitor the displacement in both directions, as one direction will lead to an increase in capacitance whereas the opposite direction will lead to a reduction. To track the y-axis displacement, both designs use a single sensor comb as shown in Figures 4.1(a) and (b).

The importance of using these displacement sensors is not limited to monitoring the displacement since they can also be used to troubleshoot the system when an interruption occurs in the optical signal between the aligned chips, i.e., to help to identify the issue by indicating whether the failure stems from the optical system or a mechanical failure in the actuators. In addition, these sensors can help to recalibrate the actuators when a performance degradation occurs.

4.4.4   Stiffness estimation and cross-talk

To achieve motion in multiple degrees of freedom, different sets of serpentine springs, folded and straight beams were included in both designs as stated before. As shown in Figures 4.1(a) and (b), z-axis and y-axis actuators were clamped on two sides using folded beams, whereas the centers of these actuators were attached to the platform using straight connecting beams. As for the x-axis actuators (Figures 4.1(c)), they are attached to the platform and also anchored to the substrate using serpentine springs. The dimensions of the springs and beams were different and they were determined by several factors. For instance, while the width of the folded beams of the y-axis actuators could be as small as 3 μm, the minimum width allowed by PiezoMUMPs design rules for the z-axis actuators is 26 μm to have enough space to lay the piezoelectric layer and to route the electrical signals to the top electrode.

The stiffness of the designs in the z-, y-, and x-axes was studied by applying a force along a single axis and observing the platform displacement in that axis according to Hooke's law (Kaajakari, 2009). As the goal of this study is to align to active chips, an optical waveguide (WG) will be added onto the optical path shown in Figures 4.1(a) and (b) to create fully functional devices. This will have an impact on the stiffness of the designs. Figure 4.2(a) shows a schematic of the optical WG routed on top of the optical path. The WG consists of an 8 μm-wide and 3 μm-thick silicon dioxide bottom cladding, and a 500 nm-wide and 400 nm-thick silicon nitride core. Figure 4.2(b) shows the 3D FE model of the simulated WG, and the resulting displacement-force relations for the z-, y- and x-axes are shown in Figure 4.2(c), where the force was applied onto the tip of the optical path. The stiffness of the WG with the optical path along these three axes, respectively, was found to be 0.002 N/m, 0.025 N/m and 0.017 N/m. As expected, the stiffness in the z-axis is the lowest. On the other hand, the highest stiffness was in the y-axis due to the compressing of the quasi-serpentine beam.

In addition, FE simulations were conducted to investigate the stiffness of the 2-DOF and 3-DOF designs with and without the inclusion of the WG onto the optical path. This was done by extracting the displacement-force relations shown in Figures 4.2(d)-(f) with the force applied onto the platform. The resulting stiffnesses are reported in Table 4.1, indicating that the addition of the WG does not have a significant impact on the stiffness of the designs. In the z-axis, the stiffnesses for the 2-DOF and 3-DOF were changed by only 4.3% and 3.9%, respectively. In the y-axis, the 2-DOF design showed only a 0.7% stiffness change, whereas the 3-DOF design exhibited a 1.5% stiffness change. The x-axis stiffness for the 3-DOF design

Table 4.1 Stiffnesses of the 2-DOF & 3-DOF Designs

Axis	Stiffness (N/m)			
	Without WG		With WG	
	2-DOF	3-DOF	2-DOF	3-DOF
Z	41.67	94.34	43.48	98.04
Y	13.99	6.68	14.09	6.78
X	-	175.44	-	178.57
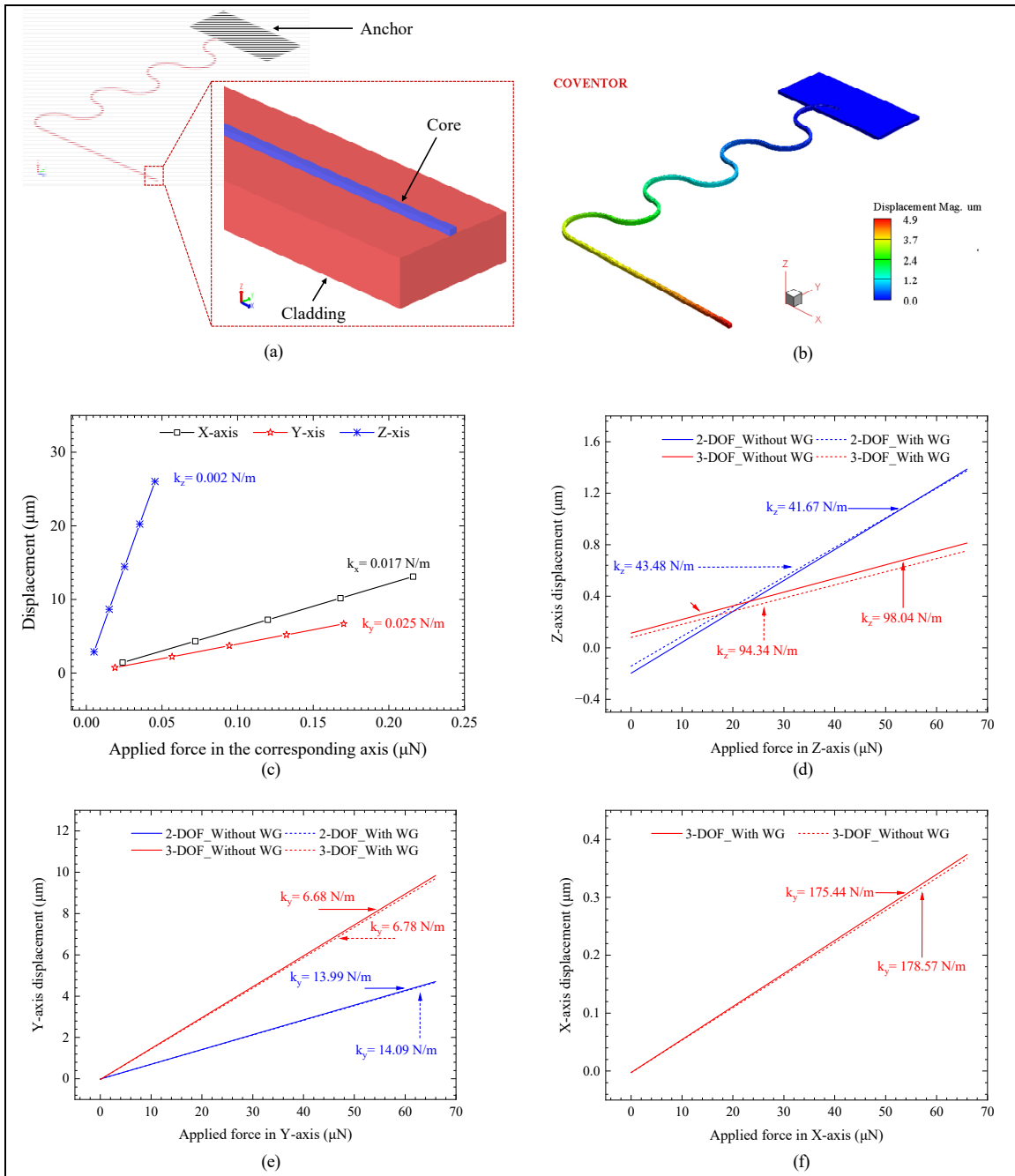
Figure 4.2 (a) The waveguide schematic, (b) the 3D profile of the simulated waveguide, (c) the displacement in the z-, y- and x-axes versus the applied force, (d)-(f) the effect of the waveguide on the z-, y- and x- axes' stiffnesses for the 2-DOF and 3-DOF designs

varied by 1.7%. As a result, the displacement is not greatly impacted by the addition of the WG onto the optical path, as can be seen in Figures 4.2(d)-(f). The figures show a linear relation between the displacement in all of the three axes and the corresponding applied force.

From this linear relation, important performance metrics such as sensitivity and resolution could be extracted and enhanced, leading to better control of the waveguide, and therefore, efficient light coupling between two chips.

The resolution of the alignment system depends on the minimum applied force on the actuators that can generate a displacement measurable by the capacitive sensors. As the cores of the waveguides of the aligned chips will generally have dimensions of a few hundred nanometers, matching their modes will require a resolution in the few tens of nanometers. To obtain a 10 nm change along the z-axis, the 2-DOF design requires about 0.5 μN of force, whereas the 3-DOF design requires about 1 μN. On the other hand, in the y-axis, to obtain a 10 nm displacement, the devices will need 0.15 μN and 0.07 μN, respectively. Contrary to the z-axis where the stiffness of the 3-DOF is double that of the 2-DOF, in the y-axis, the stiffness of the 3-DOF design is only half of that of its counterpart. The minimum force in the x-axis to achieve a 10 nm displacement is found to be 1.8 μN.

Due to the linearity of the displacement-force relation observed, the sensitivity of the actuators (i.e., the amount of displacement resulting from an incremental applied force) can be calculated directly from the forces obtained above. For the z-axis, the sensitivities of the 2-DOF and 3-DOF designs are 20 nm/μN and 10 nm/μN, respectively. In the y-axis the sensitivities are of 67 nm/μN and 143 nm/μN, respectively, and finally the x-axis the 3-DOF design is of 5.5 nm/μN.

The cross-talk is defined as the displacement generated in an axis other than the axis of the applied force. The displacements resulting from cross-talk were extracted from the displacement results given in Figures 4.2(d)-(f), and are shown in Figures 4.3(a)-(c), for forces applied in the z-, y- and x-axes, respectively. As the WG did not show a significant impact on the stiffness, the cross-talk displacements were also not significantly affected by the WG, therefore, only the results before the WG addition are presented. In the z-axis, both designs
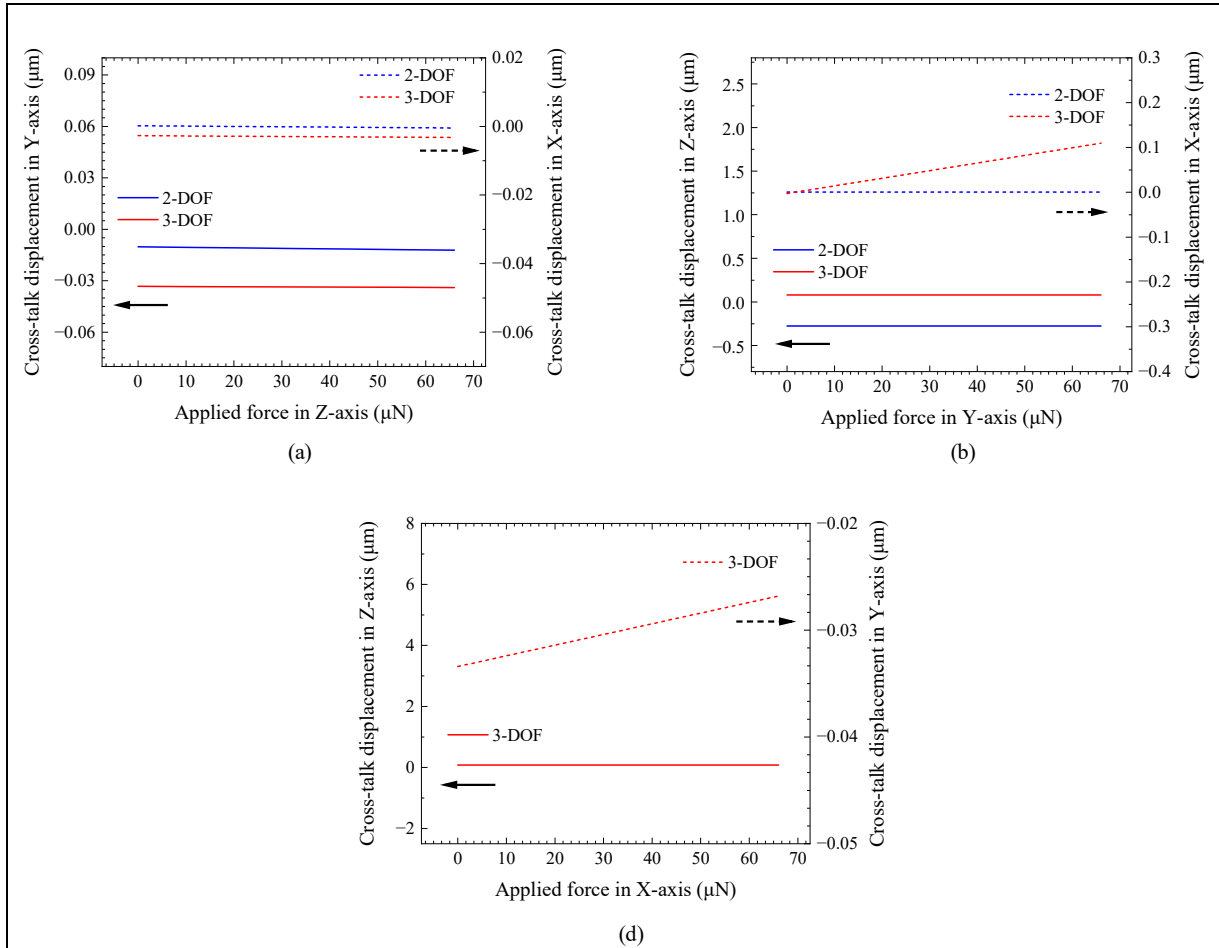
Figure 4.3 FE simulation results showing the cross-talk: (a) displacements in the y- and x-axes due to a force applied in the z-axis, (b) displacements in the z- and x-axes due to a force applied in the y-axis, and (c) displacement in the z- and y-axes due to the force applied in the x-axis

showed less than 33 nm displacement in the y- and x-axes. Similar trends were also observed for forces in the y- and x-axis, where negligible displacements were observed.

4.4.5 Design parameters

The hybrid MEMS actuators were designed based on the commercial PiezoMUMPs process provided by MEMSCAP (Cowen et al., 2014), which was used to fabricate the devices. Design parameters such as lengths, widths and thicknesses of the actuators and capacitive sensors were determined by taking into consideration the design rules of the fabrication process and the typical displacements required for the chip-to-chip optical alignment. The target z-axis

Table 4.2 Dimensions of the 2-DOF & 3-DOF Designs

Part	Dimensions	Value	
		2-DOF	3-DOF
Platform	Length	200 µm	
	Width	50 µm	
Connecting beams	Length	1000 µm	
	Width	10 µm	8 µm
Z-axis actuator	Length	1410 µm	
	Width	190 µm	
Folded beams of Z-axis actuator	Length	340 µm	
	Width	26 µm	
Folded beams of Y-axis actuator	Length	340 µm	
	Width	3 µm	
Serpentine springs of X-axis actuator	Length	-	460 µm
	Width	-	3 µm
Fingers geometry in all combs	Length	100 µm	
	Width	5 µm	
	Fingers spacings	4 µm	
	Overlap	25 µm	
Number of comb fingers	Gap actuator	66	
	Lateral actuator	-	66
	Capacitive sensing	160	
Optical path	Length	1800 µm	
	Width	10 µm	8 µm

displacement range was determined by the maximum out-of-plane misalignment reported with common chip integration techniques such as flip-chip bonding, i.e., ±0.5 µm. On the other hand, reported misalignments in the in-plane directions were on the order of ~5 µm in the direction of light propagation (y-axis) and 1 µm perpendicular to it (x-axis) (Matsumoto et al., 2019). Therefore, the piezoelectric actuators were designed to provide at least 1 µm of z-axis displacement, whereas the dimensions and numbers of combs drive for the in-plane electrostatic actuators were optimized for the in-plane displacement target of 5 µm. It is worth mentioning that the thicknesses of all of the layers used in the PiezoMUMPs process are predefined and fixed by the foundry, thus only the lengths and widths of the actuators were

adjusted to achieve the targeted displacements (simulations are presented in the next section). Table 4.2 summarizes the parameters of both designs.

4.4.6 Frequency response and mode shapes

Modal analysis was conducted by using the CoventorWare software to extract resonant frequencies and mode shapes. Three modes for the 2-DOF design are presented in Figure 4.4 at 5.8, 6.3 and 7.5 kHz. The 3-DOF design exhibited its first three modes at 4.1, 5.8 and 6.5 kHz. The resonant frequencies of the first six modes for each design will be presented in the results section and compared to the measurements.

4.4.7 Strategy for waveguide control and active-chip alignment

The FE simulation results presented in the previous section proved that the actuators can provide displacements along the z-, y-, and x-axes within the alignment accuracy required for chip-to-chip alignment. This section demonstrates the strategy followed to leverage these displacements to control the waveguide and align it to the fixed waveguide of the other chip (i.e., active chip) as illustrated in Figure 4.5(a). The active chip is placed in proximity with an initial distance (i.e., gap) from the platform that carries the suspended waveguide. When all the actuators are in idle state, the waveguides remain apart as shown in Figures 4.5(a)-(c). The y-axis actuator is then activated to gradually close the gap by moving the waveguide toward the fixed waveguide, as shown in Figure 4.5(d). Despite the closure of the gap, this alignment
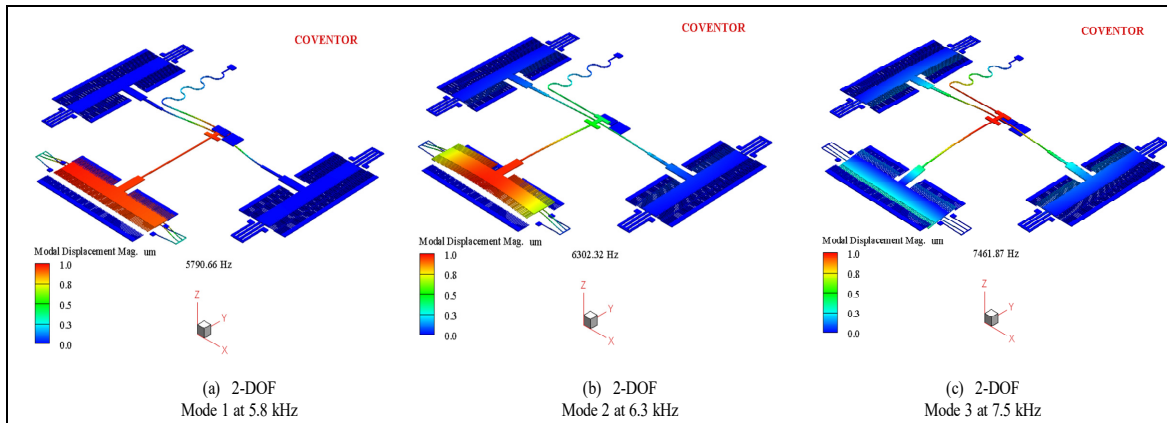
Figure 4.4 FE simulation showing the first three modes of the 2-DOF design: (a) Mode 1, 5.8 kHz, (b) Mode 2, 6.3 kHz, (c) Mode 3, 7.5 kHz
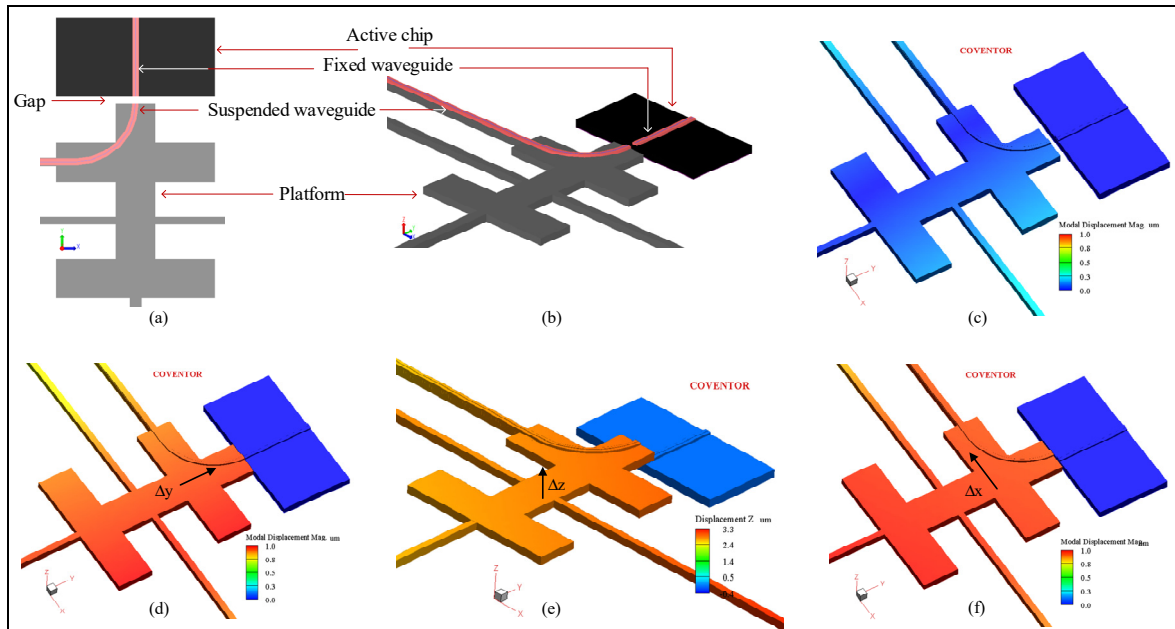
Figure 4.5 (a) and (b) schematic of the suspended and fixed waveguides, and FE simulation results showing the strategy for chip-to-chip alignment using the proposed design: (c) Gap open between the suspended and fixed waveguide when all the actuators are in idle state, (d) Activating the y-axis actuator to close the gap and make the initial alignment, while the other actuators are off, (e) activating the z-axis actuator for fine tuning in the z-axis, and (f) using the −x axis actuator to move the platform to the left for extra fine tuning

will be coarse as the cores of the two waveguides are generally small, therefore achieving complete coupling between the two waveguides will require fine tuning. This tuning is made using the z-axis and x-axis actuators. In Figure 4.5(e) the platform is moved in the upward direction with the z-axis actuator. If the tuning requires movement in the downward z-axis, the polarity of the piezoelectric actuators is changed to reverse the motion. The suspended waveguide can also be moved to the left or to the right by activating the x-axis actuators. Figure 4.5(f) shows the displacement of the suspended waveguide to the left (i.e., −x-axis).

From the linearity of the displacement-force relation and the high resolution, FE simulations predict a precise control of the waveguide positioning in the z-, y-, x- axes, and hence chip-to-chip alignment with high degree of accuracy within a few nanometers in each axis is possible. This is expected to greatly reduce the optical losses that occur with the commonly used flip-

chip integration methods due to the required safety air gap, and the lateral and horizontal misalignments (Theurer et al., 2019).

4.5   Microfabrication

The devices were fabricated using the commercial PiezoMUMPs process by MEMSCAP. The process involves five lithographic masks, following the steps detailed in our previously reported work (Rabih, Kazemi, et al., 2023) on the single DOF actuator. A simplified version of the fabrication process is shown in Figures 4.6(a)-(d). In summary, a 150 mm n-type, double-side-polished (100) oriented silicon-on-insulator (SOI) wafer with a handle layer thickness of 400 ± 5 μm and a 10 μm thick silicon device layer was used. AlN was used as a piezoelectric layer, whereas a metal stack of 20 nm of chrome and 1 μm of Al (Metal) was
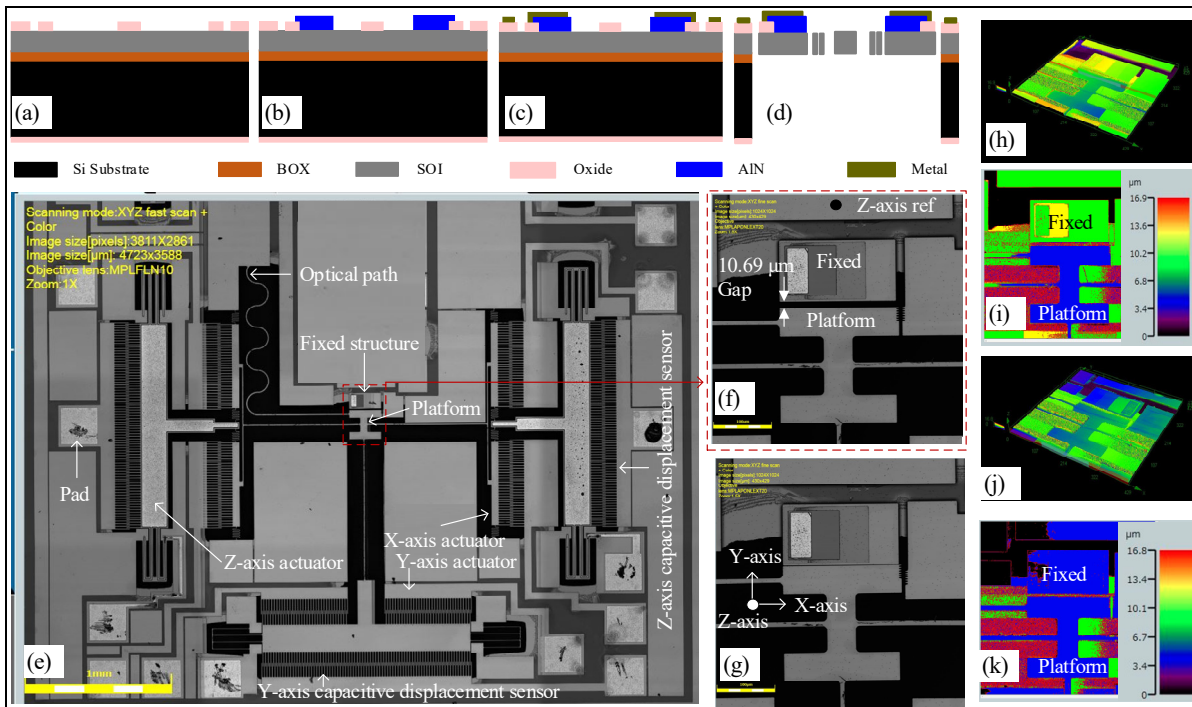
Figure 4.6 Simplified fabrication process and optical images of the fabricated device: (a) deposition and the patterning of pad oxide layer, (b) deposition and patterning of the AlN piezoelectric layer, (c) deposition and patterning of the Al pad metal layer, (d) release of the MEMS device, (e) optical images of the entire 3-DOF design, (f) platform with an initial gap of 10.9 μm from the fixed structure, (g) closing the gap by applying 140 V to the y-axis actuator, (h)-(i) and (j)-(k) the 3D profile of the platforms of the 3-DOF and 2-DOF designs, respectively

used for the pads and electrical routing. Figure 4.6(a) shows the patterning of a thermally grown 0.2 μm thick silicon dioxide layer used as a pad oxide layer. Figure 4.6(b) shows the deposition of a 0.5 μm thick AlN layer using reactive sputtering and patterning through wet etching. Figure 4.6(c) shows the deposition of metal layers by e-beam evaporation and the patterning is done using a liftoff process. Finally, the thermally grown oxide layer was removed by reactive ion etching, and the device layer was etched with deep reactive ion etching to release the structures, as shown in Figure 4.6(d). Figures 4.6(e)-(i) show images of the
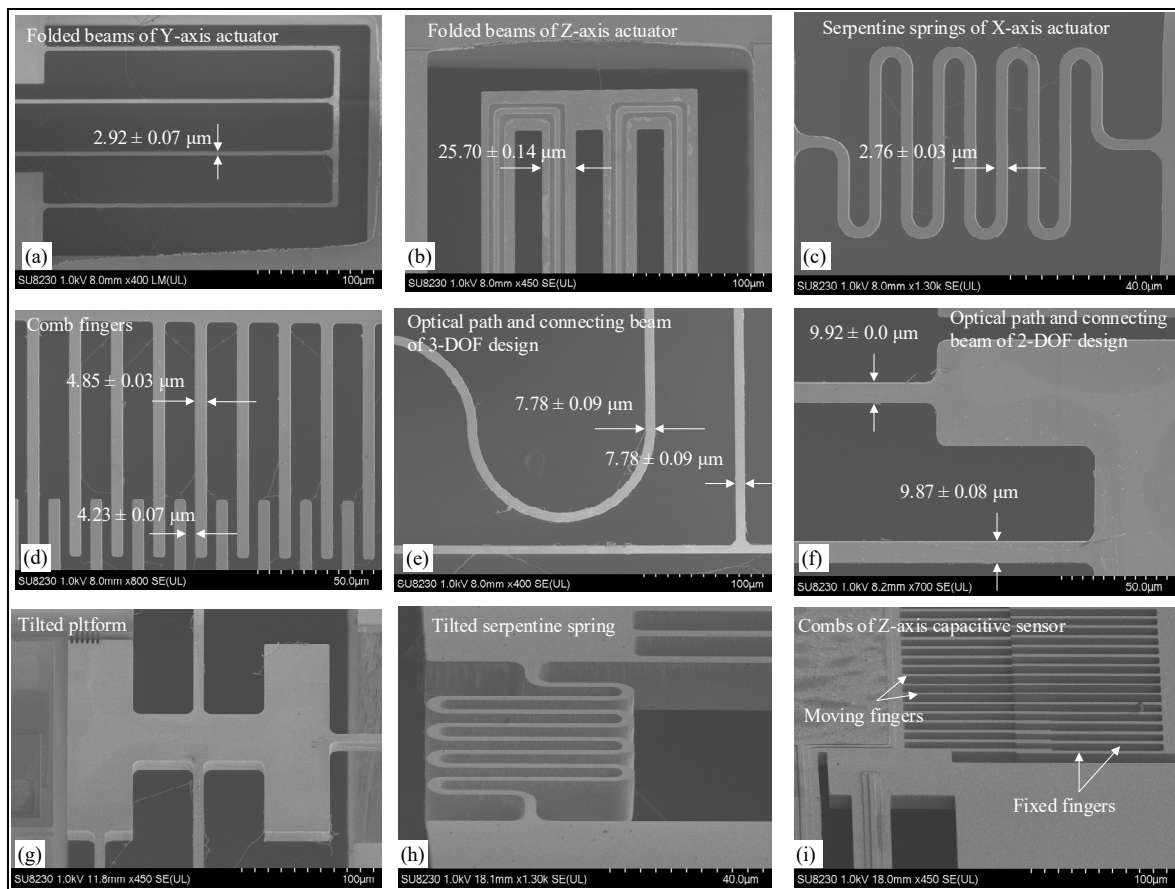
Figure 4.7 SEM images for various parts of the fabricated devices: (a) width of folded beam used to support y-axis actuator, (b) width of folded beams of the z-axis actuator, (c) width of serpentine spring of x-axis actuator, (d) width and spacing of comb fingers, (e) widths of optical path and connecting beam of 3-DOF design (f) widths of the optical path and connecting beam of 2-DOF design, and (g), (h) and (i) the tilted views of the platform, springs of x-axis actuator and comb fingers of the z-axis capacitive sensor, respectively

fabricated 3-DOF design, where in (e) the top view of the entire design is shown, (f) shows the initial gap between the platform and the fixed structure that mimics the active chip, (g) show an image of closing the initial gap by applying 140 V to the y-axis actuator, and (h) and (i) show the 3D profile of the platform for the 3-DOF design, in which the color indicates the platform is below the surface of the die. Finally, (j) and (k) give the 3D profile of the 2-DOF design platform, where it is slightly above the surface of the die.

Scanning electron microscope (SEM) micrographs of the two designs are shown in Figure 4.7. The dimensions of the connecting beams, folded beams, serpentine springs, and comb fingers and the optical path can be seen. The measured values were compared to the designed ones in Table 4.3. As shown in the table, the averaged measured dimensions indicate that the designed were subjected to over etching that caused the widths of all parts to come out smaller than their designed values. For instance, the width of connecting beams for both 2-DOF and 3-DOF

Table 4.3 Comparison of Designed vs Fabricated Values of Key Parts of 2-DOF and 3-DOF Designs

Part	Dimension	Value (µm)			
		Designed		Fabricated	
		2-DOF	3-DOF	2-DOF	3-DOF
Connecting beams	Width	10	8	9.87 ± 0.08	7.78 ± 0.08
Folded beams of Z-axis actuator	Width	26		25.70 ± 0.14	
Folded beams of Y-axis actuator	Width	3		2.92 ± 0.07	
Serpentine springs of X-axis actuator	Width	-	3		2.76 ± 0.03
Comb fingers	Width	5		4.85 ± 0.03	
	Spacing	4		4.23 ± 0.07	
Optical path	Width	10	8	9.92 ± 0.0	7.78 ± 0.09
Gap between platform and fixed part		10		10.77 ± 0.14	

designs were measured to be 9.87 ± 0.08 μm and 7.78 ± 0.09 μm compared to their nominal designed values of 10 μm and 8 μm, respectively. For the folded beams used to support the z-axis actuator, both designs used the same width of 26 μm, but the average measured widths of the fabricated devices were found to be 25.70 ± 0.14 μm. In addition, the folded beams used to support the y-axis actuators were also identical for both designs, and they were designed to be 3 μm, whereas the fabricated widths were found to be 2.92 ± 0.07 μm. These discrepancies contribute to some errors between the simulated and measured displacements and capacitances, as will be explained in the results and discussion sections.
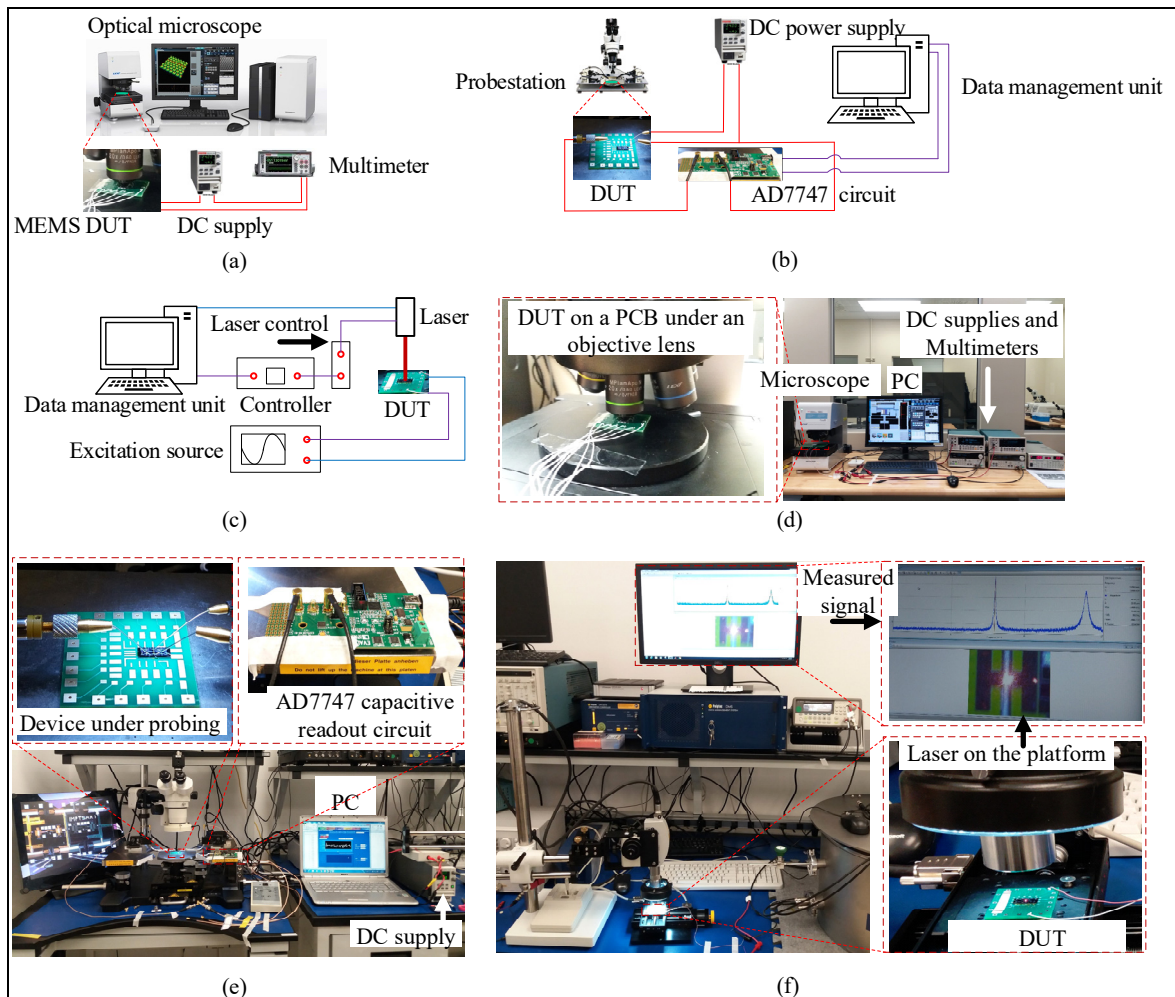
Figure 4.8 Experimental setups showing schematics of: (a) DC displacement measurement using a microscope, (b) capacitance measurement using a capacitance readout circuit, (c) dynamic test to extract resonant modes using a vibrometer. From (d), (e) and (f) are photos of the actual setups used

4.6   Measurement Methods

To experimentally characterize the fabricated hybrid MEMS actuators, their static and dynamic behaviors were investigated as follows. A LEXT OLS 4100 laser confocal microscope from Olympus (Tokyo, Japan) was used to measure the displacements provided by the actuators as depicted in Figure 4.8(a). As shown in this figure, the MEMS device dies were mounted and wirebonded onto a printed circuit board (PCB) and placed under the microscope. The devices were activated with a DC voltage source. The images were then analyzed to determine the deflection for different actuation voltages. To assess the out-of-plane displacement along the z-axis, which is generated by the piezoelectric actuators, voltages ranging from −60 V to 60 V were applied in 10 V increments. Conversely, for the in-plane gap closing displacement along the y-axis, voltages ranging from 0 V to 120 V were utilized in 20 V increments. For the lateral in-plane displacement along the x-axis, the maximum voltage used was 100 V, and the measurement was conducted using a Keyence VHX microscope (Itasca, IL, USA). It is worth noting that the z-axis displacement was assessed by scanning a vertical line through the center of the platform, and measuring its step height with regard to a reference point marked as z-axis ref in Figure 4.6(f).

The capacitance variations of the sensing combs utilized in the study were measured using a commercial capacitive readout circuit (AD7747EBZ) [28] manufactured by Analog Devices (Wilmington, MA, USA). This measurement was performed at various actuation voltages for both in-plane and out-of-plane actuation. To mitigate the impact of parasitic capacitances, the measurements were conducted using a probe station (EP6 model from Cascade), as depicted in Figure 4.8(b). This readout circuit, interfaced to a PC, has a high linearity (±0.01%) and a high resolution (±4 fF factory calibrated) that makes it possible to measure the static capacitance. The software was set to record the average of 100 samples for each measurement. The circuit was first calibrated prior to connecting the DUT, where the noise of the open input was recorded, and a level within the recommended range was achieved. Then the DUT was connected and the result of 100 averaged measurements was recorded prior to actuation and then measured again at various levels of the actuation voltage. Additionally, measurements

were also repeated five times for each case. The same probes were kept throughout the measurements; thus, the parasitic capacitance is expected to be constant for all the measurement cycles. Therefore, subtracting the subsequent measured capacitances from the initial value helped to eliminate the parasitic capacitance. In a productized application, the readout circuitry would be integrated with the MEMS device to reduce parasitics, in a similar fashion to what is done in MEMS accelerometers.

The dynamic responses of the hybrid MEMS actuators were measured using a laser doppler vibrometer from Polytec (Irvine, CA, USA) as shown in Figure 4.8(c). To excite the actuators and extract the resonant modes, a Keysight (Santa Rosa, CA, USA) function generator model 33250A was used to apply a $3 - 15$ kHz AC signal to the electrodes of the piezoelectric actuators, and the laser beam of the vibrometer was focused on the platform. A fast Fourier transform (FFT) was performed on the measured data to identify the resonant modes. The experimental setups for each of the aforementioned measurements are shown in Figures 4.8(d), (e) and (f).

4.7   Measurement results

Prior to activating the actuators, the suspended platforms of all the devices were found to exhibit an initial deformation, making them misaligned in the z-axis. The reference elevation was taken on a fixed point on the chip corresponding to where an active chip would be located. For all of the 2-DOF devices tested, their platforms were found to initially lie above the fixed surface in the range of $\sim 0.9 - 1.05$ μm. Figures 4.6(j) and (k) shows the 3D profile of the platform of a 2-DOF device. The color code indicates that the platform is slightly above the fixed surface on the opposite side of the gap. On the other hand, for the 3-DOF devices, the platforms of two devices were initially found to be below the fixed surface by $\sim -2.22 - -3.72$ μm as illustrated by the color code of the 3D profile in Figures 4.6(h) and (i), whereas one device was found to rest above the fixed surface by 1.22 ± 0.02 μm.

As shown in Figure 4.1, the platforms are connected to the actuators through suspended connecting beams, where the beam widths are 10 µm and 8 µm, for the 2-DOF and 3-DOF designs, respectively. Therefore, due to the smaller width of the 3-DOF design, minor fabrication variations in layer geometry could be the cause of the difference in initial deformations.

For the z-axis and y-axis displacements characterization, three devices from each of the two designs were tested, and tests were repeated five times for each individual device. The average value was calculated and compared to simulations. In the forthcoming analysis, we will use the labels 2-DOF and 3-DOF to represent the average results of the three tested devices of each design.

Capacitance at the same actuation voltages used to get displacements was also measured, and the change was plotted versus their corresponding displacements. It is worth mentioning that because of the high stray capacitance in the wirebonded devices, the measurement was conducted on devices that were probed directly on die. As such, only one device was characterized for each design, and is a different instance of the devices characterized to extract the displacements. The nominal simulated capacitance values for the z-axis capacitive sensors are 248 fF and 304 fF, respectively, for the 2-DOF and 3-DOF designs, whereas for the y-axis sensors, the two designs have nominal values of 231 fF and 187 fF, respectively. It should be noted that although the same comb geometry was used for both designs, the capacitances are different due to different initial deformations that resulted in a different initial effective overlap area.

4.7.1 Z-axis displacement and capacitance

Figure 4.9(a) shows the average z-axis displacements of both designs vs the applied voltage compared to the simulations. With reference to this figure, the average displacement for both designs increases with an increase in the absolute values of the actuation voltage. At the minimum applied negative voltage of -60 V, the 2-DOF design gives simulated displacement of -1.63 µm, while the average measured displacements for the three tested devices was -1.46 ± 0.34 µm, with a relative error of 10.8%. The larger relative error between the average

and simulation is due to the larger initial deformation (1.05 µm) of one device compared to the
other two devices (<1 µm), where the initial deformation is attributed to residual stress in the
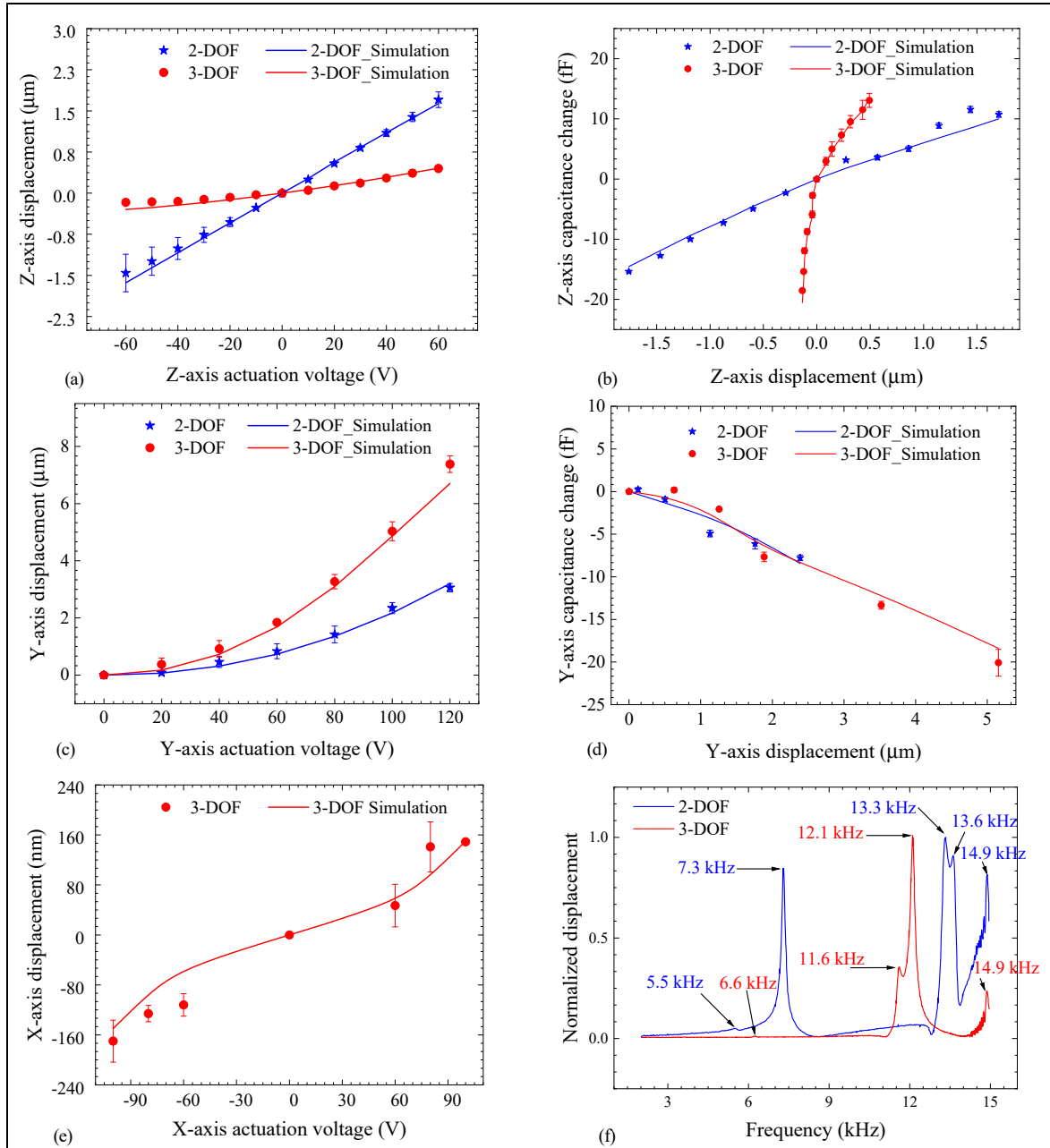
Figure 4.9 (a) Average platform z-axis displacement vs actuation voltage, (b) z-axis
capacitance change vs displacement, (c) average platform y-axis displacement vs actuation
voltage (d) average y-axis capacitance change vs displacement (e) average platform x-axis
displacement vs actuation voltage for the 3-DOF design, and (f) normalized displacement
frequency response showing the resonant peaks

devices. This has also led to a significant standard error (0.34 μm) from the average. For the 3-DOF design, the results follow the same trend as that of the 2-DOF design, but are of smaller magnitude, due to the presence of the additional springs that are used in the 3-DOF design to accommodate the lateral actuators along the x-axis, increasing the z-axis stiffness. These springs increased the stiffness of the 3-DOF design by more than twice that of the 2-DOF design, as presented in Figure 4.2(d). Therefore, the average displacement was found to be −0.17 ± 0.03 μm versus −0.30 μm in simulations, with a relative error exceeding 30%. The lower standard error from the average indicates that the results of all three devices for this 3-DOF design were significantly lower than the simulations. This disparity can be attributed to the presence of tensile residual stress in the devices (evidenced by the platforms being initially below the surface of the dies by more than 2 μm for the majority of the devices tested).

For positive voltages, at 60 V, simulations of the 2-DOF predict a displacement of 1.63 μm (symmetric with the negative voltage case), whereas the average measured displacement for the three devices was 1.70 ± 0.14 μm, with a relative error difference of 4.3%. The performance of the devices was observed to be better for positive voltages, resulting in lower discrepancies with simulation results. The same improvement was observed for the 3-DOF devices, where the simulation predicted a displacement of 0.45 μm, while the average measured displacement of the three devices was found to be 0.46 ± 0.04 μm. The improvement in the displacements for the positive voltages can be attributed to the initial deformation being in the opposite direction to that of the platform movement for the positive voltages. It is worth pointing out that residual stress is believed to be a significant source of the differences between the upward and downward displacement values for the same actuation voltage magnitude, as predicted by simulation. A stress study on a single DOF device done in (Rabih, Kazemi, et al., 2023) demonstrated that while the absence of residual stress can guarantee symmetry in the upward and downward displacements, applying tensile or compressive stresses can drastically change the behavior of the device.

Figure 4.9(b) shows the change in capacitance for both the 2-DOF and 3-DOF designs versus their predicted z-axis displacements. For the 3-DOF design, at the maximum measured downward platform displacement of −0.17 ± 0.03 μm, the average measured capacitance change was −18.53 ± 0.16 fF (−20.54 fF in simulations), whereas the maximum measured

upward displacement of 0.46 ± 0.04 µm gave a capacitance change of 13.06 ± 1.16 fF (13.38 fF in simulations). Despite the significant differences between the z-axis displacements of the 2-DOF and 3-DOF designs, the capacitance changes are on the same order. This is because identical capacitive sensors were used in both designs. The displacements for the two designs are different because of the different widths of the beams that connect the sensing combs to the platform, as indicated in Table 4.1 (i.e., 10 µm for the 2-DOF design versus 8 µm for the 3-DOF design).

4.7.2   Y-axis displacement and capacitance

The y-axis displacement was achieved by increasing the actuation voltage within the range of 0-120 V to close the gap. As shown in Figure 4.9(c), in the case of the 2-DOF design, at a voltage of 120 V, the average longitudinal displacements for the three devices was measured to be 3.06 ± 0.17 µm, in comparison, simulations predicted a displacement of 3.20 µm. This yields relative difference of 4.4%. For the 3-DOF design, in contrast to what was observed for the z-axis displacement, a larger displacement along the y-axis was achieved compared to the 2-DOF design. At the same actuation voltage of 120 V, the average displacement for the three devices of the 3-DOF design gives 7.38 ± 0.29 µm, compared to 6.71 µm predicted by simulations. This represents an error of 10.1%. The measurements also show that increasing the actuation voltage to 140 V fully closes the initial gap of 10.69 µm, as shown in Figures 4.6(f) and (g). This is due to the smaller width (8 µm) of the connecting beams and optical path in the 3-DOF design compared to the 2-DOF design (10 µm). Thus, the stiffness of the 3-DOF design along the y-axis is smaller (about half) than that of the 2-DOF design, as shown in Figure 4.2(e). As shown in Figure 4.6(g), when the gap is closed, the platform exhibits a small counterclockwise rotation of 0.09° in the z-axis. This is due to the presence of a single optical path, and adding another one to the right side of the platform would mitigate this rotation.

The change in capacitance caused by motion along the y-axis was also measured for both the 2-DOF and 3-DOF designs, as reported in Figure 4.9(d). Contrary to what was observed for

the z-axis capacitances, the y-axis capacitance decreases for both designs when the displacement increases. This is due to the decrease of the overlapping area. For the 2-DOF design, the average capacitance change was -7.77 ± 0.32 fF (-8.44 fF in simulations) when the y-axis displacement was 2.39 ± 0.34 µm at an actuation voltage of 100 V. On the other hand, at the same actuation voltage, the 3-DOF design achieved a displacement of 5.16 ± 0.28 µm, with an average capacitance change of -20.09 ± 1.56 fF (-18.39 fF in simulations). In contrast to the z-axis capacitance, the y-axis capacitance is directly proportional to the platform displacement. Therefore, higher displacements, such as seen in the 3-DOF design, produce higher capacitance changes.

4.7.3   X-axis displacement

The x-axis displacement for the 3-DOF design is presented in Figure 4.9(e). Due to small displacements along the x-axis, a microscope with a 6000X magnification (Keyence VHX microscope) was used. The displacement measured in the range of ± 100 V shows that at -100 V (100 V applied to the left lateral actuator), the average platform displacement in the left direction is -170 ± 33 nm versus -150 nm predicted by simulations. On the other hand, by applying the same voltage to the right lateral actuator, the platform moved to the right by 149 ± 10 nm, which is much closer to simulations.

4.7.4   Misalignment compensation

As stated earlier and demonstrated by Figure 4.5, the ultimate purpose of these hybrid piezoelectric-electrostatic MEMS actuators is for chip-to-chip alignment in PICs. Thus, more than one actuator will be activated at the same time to move the platform in different directions, i.e., z-, y-, and x-axis.

To demonstrate the alignment capability of the actuators, a procedure to level the platforms of a 2-DOF design and a 3-DOF design as they move towards the fixed section of the device layer is presented below. This allows to mitigate the initial out-of-plane deformation along the z-axis discussed previously while reducing the gap. With the embedded displacement sensors, it would be possible to create closed-loop self-aligned electro-optical systems to integrate active components on SiPh chips.

Figure 4.10(a) shows the activation of both the z-axis and y-axis actuators to control the platform of the 2-DOF design. The platform was initially above the surface of the die. It was observed that activating the y-axis actuator alone would not only close the gap along this axis, but also would cause undesired upward z-axis displacement. The initial deformation and the undesired displacement were caused by residual stress post-fabrication. Thus, a negative voltage was applied to the z-axis actuator to bring the platform downward and compensate for the misalignment caused by the y-axis actuator. As seen in Figure 4.10(a), the 2-DOF device showed an average upward z-axis displacement of 1.27 ± 0.02 µm when the platform was displaced by 3.06 ± 0.17 µm along the y-axis (as per Figure 4.9(c)) with a 120 V actuation
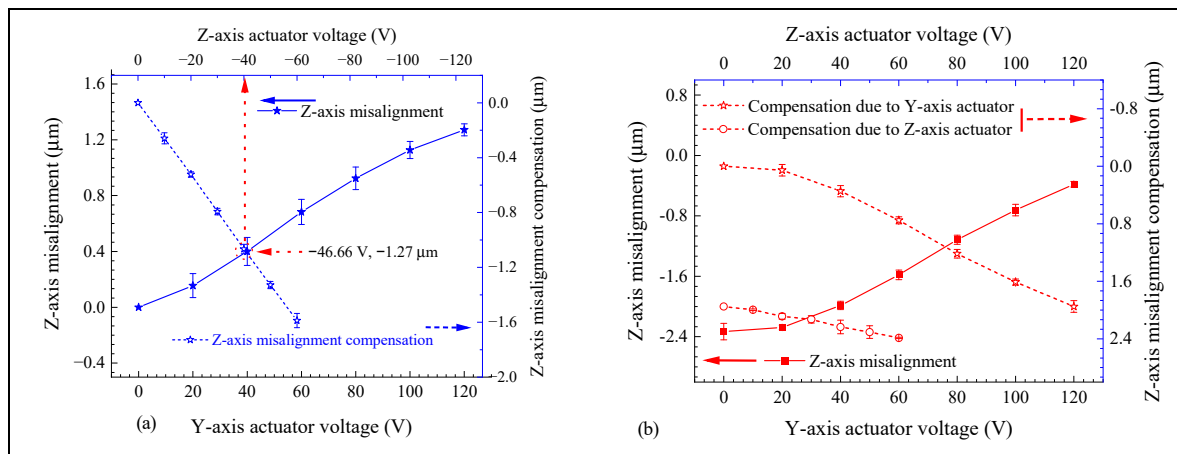
Figure 4.10 Simultaneous activation of z-axis and the y-axis actuators to close the initial gap in the y-axis and to compensate for the z-axis misalignment of the (a) 2-DOF design and (b) the 3-DOF design

voltage applied on the y-axis actuator. This misalignment was compensated by applying −46.66 V to the z-axis actuator.

Similarly, Figure 4.10(b) shows the alignment procedure for the platform of a 3-DOF device. As shown in this figure, the platform was initially below the surface of the die by -2.33 ± 0.11 µm. Closing the gap introduced, similarly to the 2-DOF design, an upward displacement along the z-axis, which helped to reduce the z-axis misalignment, as shown by the y-axis compensation curve. Thus, at a 120 V longitudinal actuation voltage when the platform was displaced by 7.38 ± 0.29 µm along the y-axis (as per Figure 4.9(c)), the initial z-axis misalignment was reduced to only -0.38 ± 0.04 µm through the y-axis actuator-induced

z-axis displacement of 1.95 ± 0.08 µm. The z-axis actuator was used to remove the remaining misalignment and therefore level the platform. This required an additional upward motion of 0.44 ± 0.01 µm at 60 V to reach a total z-axis displacement of 2.39 ± 0.01 µm, which was sufficient to completely compensate the initial z-axis misalignment.

In order to illustrate the repeatable behavior of the actuator, Figure 4.11 demonstrates a simultaneous activation sequence of the z-axis and y-axis actuators of the 2-DOF design. Four activation cycles were performed, each consisting of nine actuation steps (AS). At AS 1, all the actuators were inactive. Note that the initial z-axis misalignment of the platform was measured to be 0.93 µm above the fixed surface. Then at AS 2, only the y-axis actuator was activated at 120 V, and the initial misalignment increased to 1.62 µm. From AS 2 to AS 3, the downward z-axis actuator was activated by applying −10 V to −60V. This reduced the z-axis misalignment from 1.62 µm to only 0.01 µm. At AS 4, the z-axis actuator was de-activated while maintaining the y-axis actuator on which brought the z-axis misalignment back to 1.62 µm. At AS 5, all of the actuators were deactivated returning the z-axis misalignment to the initial 0.93 µm. AS 5 to AS 9 repeated the same process, however with a positive voltage applied to the z-axis actuator at AS 6 to AS 7, leading to a z-axis misalignment increase to 3.13 µm. Then, switching off the z-axis actuator while maintaining the y-axis actuator on returned the misalignment to 1.62 µm at AS 8. The first cycle was terminated by turning off the y-axis actuator to bring down the out-of-plane misalignment to the initial value of 0.93 µm at AS 9. Cycles 2, 3 and 4 were performed following the same actuation sequence, resulting in a similar
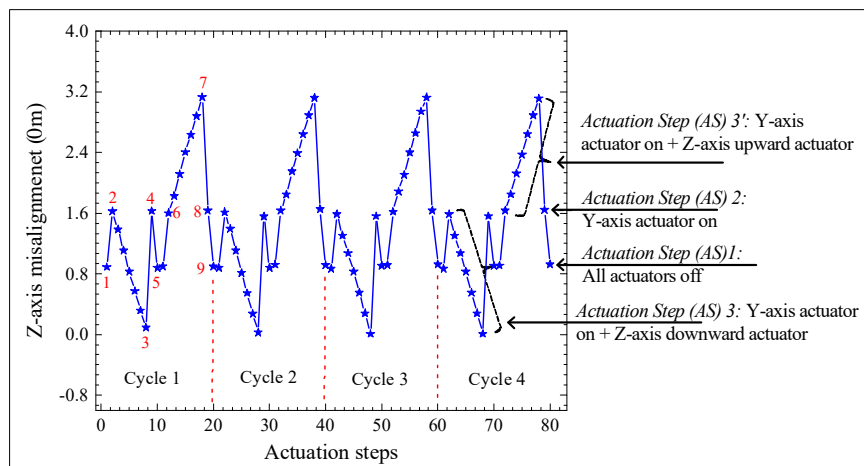
Figure 4.11 Four actuation cycles of the 2-DOF design each composed of the same sequence of actuation steps

displacement for each cycle, outlining the repeatability of the actuation. Note that these 4 cycles are not sufficient to establish the long-term reliability of the device.

4.7.5 Measurement of frequency response

The resonant response of the 2-DOF and 3-DOF designs were measured and are compared with the simulated values in Table 4.4. It is important to note that certain resonant modes observed in the simulations did not show detectable out-of-plane motions of the platform. Therefore, these specific modes could not be measured experimentally. For instance, in the case of the 2-DOF design, it was observed that the 2nd mode was not detected by the vibrometer. It is worth mentioning that for the 1st and 4th modes, despite their primary in-plane motions, they have small but detectable out-of-plane components. Thus, they were measured. Similarly, for the 3-DOF design, the 1st and 3rd modes could not be measured. However, despite the over etching of some parts that reduced the dimensions, the modes that were captured during the experiments were still found to closely match simulations, exhibiting a maximum discrepancy of less than 22%. In Figure 4.9(f), the frequency response of the displacement extracted by the vibrometer shows the resonant peaks of both designs.

Table 4.4 Resonant modes of the 2-DOF and 3-DOF designs

| Mode | Resonant frequency (kHz) | | | | | |
| | 2-DOF Design | | | 3-DOF Design | | |
	Measured	Simulated	Error %	Measured	Simulated	Error %
1st	5.5	5.8	5.4	-	4.1	-
2nd	-	6.3	-	6.2	5.8	6.5
3rd	7.3	7.5	2.7	-	6.5	-
4th	13.3	11.8	12.4	11.6	10.1	14.7
5th	13.6	12.4	10.1	12.1	10.3	17.1
6th	14.9	14.0	6.1	14.9	12.2	22.0

4.8   Discussion

The results demonstrated that adding the capability to move in the lateral direction leads to an important trade-off with the range of motion achievable in the vertical direction. This happens because of the additional anchor points required for the 3-DOF design, as shown in Figure 4.1(b). Therefore, the stiffness increased and it directly impacted the displacement; the 3-DOF design moved by only ~0.63 μm in the z-axis, whereas the designs 2-DOF design achieved more than twice that value.

The inclusion of narrower serpentine springs in the 3-DOF design affected the initial deformation caused by residual stress. However, the longitudinal displacement in the y-axis was not affected by the addition of the x-axis actuators. Since the 2-DOF design did not include serpentine springs, reducing the widths of the optical path and connecting beams to 8 μm will reduce the stiffness in the y-axis by more than half, and thus the 2-DOF design is expected to perform better than the 3-DOF design. However, the reduction of these long structures' widths can lead to mechanical failures and shortened lifetimes.

A significant advantage of the 3-DOF design over the 2-DOF design is its ability to provide 300 nm of lateral displacement at ±100 V, beyond which the moving combs come into contact with the fixed ones at ~120 V. Although this displacement is smaller than the target of ±0.5 μm, the performance could be further enhanced by optimizing the comb fingers and the springs to increase the x-axis voltage at which the moving combs will come into contact with the fixed ones. This is expected to result in a trade-off in the voltages required by the other actuators.

The fabricated devices from both designs experienced tensile stresses of ~ 165 MPa that caused the z-axis actuators to bend down, as shown by the misalignment of comb fingers in Figure 4.7(f). The value of the stress was determined by FEA by simulating the designs without loads or voltages and measuring the platform initial deformation that matches the initial deformation obtained by the measurements. The capacitance measurements in the y axis was found to correlate well with the tracked displacement for both designs.

It is worth noting that in the z-axis, despite the lower displacement for the 3-DOF design, the measured capacitance changes were almost the same for both designs. This is because the displacement of the platform for the 3-DOF design is not correlated through the connecting

beams in the same fashion to the capacitive sensors' motion. Bringing the capacitive sensors closer to the platform in both designs could remove this difference.

Hybrid piezoelectric-electrostatic systems were reported previously for applications other than chip-to-chip alignment. For instance, (Ikehashi, Ogawa, Yamazaki, & Ohguro, 2007) used this principle to control an RF MEMS capacitor, where a piezoelectric actuator is initially used to bring a platform downward to a certain position then an electrostatic actuator is used to pull the platform to a bottom contact. In (Pengwang, Rabenorosoa, Rakotondrabe, & Andreff, 2013), the two actuation principles were integrated in robotic surgery for medical applications. Table 4.5 summarizes state-of-the-art MEMS actuators published in the literature for various silicon photonic applications. The actuators are compared by specifying their out-of-plane displacement in z-axis, beside the in-plane displacements along the y and x axes, in addition to their footprint. In (Sharma et al., 2023b), hybrid piezoelectric-electrostatic actuators fabricated by the PiezoMUMPs process were used to implement a 1×5 planar optical switch. The design has a 4.32 mm^2 footprint and provides displacements in all of the three axes, with a maximum value of 11.7 μm at 150 V provided by electrostatic parallel plate actuators in the x-axis. The z-axis displacement generated by piezoelectric actuators is 300 nm, whereas the y-axis displacement given by another electrostatic actuator is 2.2 μm at 80 V.

For optical scanning applications, high displacement is required. Thus, electrothermal actuation techniques are preferred, as demonstrated in (Jovic et al., 2018) and (Barrett et al., 2019). However, electrothermal actuation is known for its high-power dissipation, compared to the piezoelectric and electrostatic methods used in this work. In (Barrett et al., 2019), hybrid electrostatic-electrothermal actuators were used to design a MEMS scanner. As high as 39.5 μm, 14.1 μm, 14.1 μm displacements were achieved in the z-axis, y-axis and x-axis at 52 V, 130 V and 130 V, respectively. However, very long and thin ~2 μm tethers were used to support a circular plate that has the same thickness and a diameter of 100 μm.

For chip-to-chip alignment, in (T. Peters & Tichem, 2017) bimorph electrothermal actuators were proposed to align an array of suspended waveguides to vertically compensate 4 – 5 μm of out-of-plane misalignment and align the waveguides to laser diodes. In another study, (Q. X. Zhang et al., 2010) incorporated large-two-axis in-plane electrothermal actuators in a flip-

Table 4.5 State of the art mems actuators compared to the proposed 2-DOF and 3-DOF designs

Application	Footprint (mm²)	Actuation axis						Ref.
		Z		Y		X		
		Voltage (V)	Disp. (μm)	Voltage (V)	Disp. (μm)	Voltage (V)	Disp. (μm)	
Switch	4.32	10	0.3	80	2.2	150	11.7	(Sharma, Nabavi, Rabih, Ménard, & Nabki, 2023b)
Splitter	-	-	-	-	-	13	0.6	(Bishop et al., 2018)
Phase shifter	-	15	0.2	-	-	-	-	(Marcel W. Pruessner, Park, Stievater, Kozak, & Rabinovich, 2016)
Resonator	-	70	1.4	-	-	-	-	(M. M. Lee & Wu, 2005)
Scanner	6.45	52	39.5	130	14.2	130	14.2	(Barrett et al., 2019)
	1.5	100	6	100	0.4	100	0.2	(T. Kim & Gorman, 2022)
	70	170 mW	1000	170 mW	2000	-	-	(Jovic et al., 2018)
Alignment	121.5	25	170	14	138	14	83	(Kong, Cao, Zhu, Nie, & Xi, 2023)
	16.61	-	-	>23	50	>18	25	(Q. X. Zhang et al., 2010)
	14.44	60	3.47	120	3.14	-	-	This work-2-DOF
	14.44	60	0.63	140	10.69	100	0.30	This work-3-DOF

chip bonded SOI platform to align a discrete laser diode to a Si waveguide. Displacements greater than 50 μm were achieved in both the y-and x-axes using chevron type electrothermal actuators. In (Kong et al., 2023) two optical fibers were aligned by using three electrothermal actuators, which required a footprint exceeding 100 mm². For other applications, such as beam splitting, phase shifting and tunable optical resonators presented in (Bishop et al., 2018),

(Marcel W. Pruessner et al., 2016), and (M. M. Lee & Wu, 2005) respectively, displacements of only a few nanometers to sub-microns are required, thus small structures are used. As such, they require small actuation voltages.

Our proposed designs compare favorably to the reported works. The 2-DOF design exhibits higher z-axis displacement for the intended application, and the 3-DOF design allows for 3-axis operation. However, the proposed designs required relatively high actuation voltages of up to 140 V to close the gap. It is worth noting that the integration of the 8 μm and 10 μm-wide optical paths in the 3-DOF design and the 2-DOF design, respectively, advantageously allows for multiple waveguides to be integrated within the devices, by using waveguide cores of different size to enable compact devices, such as demonstrated in (Q. Han et al., 2020). Despite the fact that the 3-DOF design provide less than ±0.5 μm along the z- and x-axes because of the impacts of higher stiffnesses and mechanical stress, our proposed designs based on a dual hybrid piezoelectric-electrostatic actuation mechanism are expected to pave the way to integrated low power and low-cost MEMS positioners for active chip alignment in PICs.

4.9 Conclusion

We demonstrated 2-DOF and 3-DOF MEMS hybrid piezoelectric-electrostatic actuators with the capability of housing optical waveguides on their structures for potential use in chip-to-chip alignment in PICs. The integrated comb fingers track the platform displacement in both the z- and y-axes, where upward and downward z-axis displacement with a total travel range of 3.16 ± 0.34 μm at ±60 V was measured for three devices with the 2-DOF design, whereas the average results of three devices with the 3-DOF design show a 0.63 ± 0.04 μm z-axis displacement at the same voltage. In the y-axis, average displacements of 3.06 ± 0.17 μm at 120 V and 10.69 μm at 140 V were achieved by the 2-DOF and 3-DOF designs, respectively. Additionally, in the x-axis, the 3-DOF design exhibits a displacement of 300 nm at ±100 V. The devices have capacitive displacement sensors, and good correlations between the capacitance and the tracked displacements along the z- and y-axes were observed.

Simultaneous activation of two actuators eliminated the initial deformation of the suspended platform and leveled it in the z-axis with a good repeatability. Despite their good performance, the results of both designs were influenced by the residual stress caused by the piezoelectric and top electrode layers, and therefore, stress control can help improve further the performance of the devices.

This hybrid piezoelectric-electrostatic drive mechanism has the potential to enable efficient chip-to-chip alignment by reducing the size of safety air gaps and eliminating misalignments arising when integrating different chips. This can be achieved not only during packaging, as is common practice, but also during device operation. Therefore, these devices could improve the performance and fabrication yield of advanced photonic systems. Moreover, by relaxing the alignment requirements during assembly, these micropositioners simplify packaging, which could reduce cost.

4.10   Summary of chapter 4

This chapter detailed the advancement of positioner technology to include 2DOF and 3DOF hybrid piezoelectric-electrostatic designs, each equipped with capacitive displacement sensors for precise tracking of waveguide-carrying platforms. These positioners represent evolved iterations of the 1DOF model introduced in Chapter 3. A common challenge identified across all designs was the significant residual stress experienced, attributed primarily to the use of lengthy beams connecting the waveguides to the actuators and the comparatively minimal thickness of the device layer, set at 10 μm. Additionally, the displacement capabilities of the piezoelectric and electrostatic actuators were found to be inadequate across all three axes.

Addressing these limitations, the forthcoming chapter will introduce the use of electrothermal actuators. These actuators are selected for their superior displacement abilities and will be utilized to develop a MEMS positioner characterized by a compact footprint and minimized residual stress impact. This approach aims to enhance the performance and reliability of MEMS positioners in aligning optical waveguides within photonic integrated circuits.

CHAPTER 5

A 3 DEGREES-OF-FREEDOM ELECTROTHERMAL MICRO-POSITIONER FOR OPTICAL CHIP-TO-CHIP ALIGNMENT

Almur A S Rabih, Student member, IEEE, Seyedfakhreddin Nabavi, Member, IEEE, Michaël Menard, Member, IEEE and Frederic Nabki, Member, IEEE

5.1   Preface

This chapter presents 3DOF positioner based on electrothermal actuators. The contribution of this positioner is using electrothermal forces to generate motion in the x-, y-, z- axes, where to generate the out-of-plane motion in the z-axis, a novel method involving two opposite in-plane electrothermal forces in the x-axis is implemented. AASR designed and simulated the devices. SN tested the fabricated devices. MM and FN supervised the work. Chapter 6 which follows this chapter presents the 2DOF version of this positioner with an integrated suspended silicon nitride optical waveguide to demonstrate not only an actuator, but also integrated optical functionality.

5.2   Abstract

This chapter proposes an electrothermal three-degrees-of-freedom (3-DOF) micro-positioner equipped with a waveguide path, which can potentially be used for chip-to-chip alignment in photonic integrated circuits. The micro-positioner provides translational displacements along the x-, y- and z- axes with manageable levels of cross-sensitivity between axes. A fabricated prototype provides displacements of ±3.35 μm at 105 mW along the x-axis, and +4.5 μm at 140 mW along the y-axis. Moreover, +7 μm of out-of-plane displacement is achieved along the z-axis when 210 mW is applied to the x-axis actuators to buckle the structure. The AC

response of the micro-positioner shows that the fundamental resonance mode occurs at 18.8 kHz.

Index Terms—3-axis micro-positioner, optical alignment, 3 degrees of freedom (3-DOF), electrothermal, beam buckling

5.3 Introduction

Silicon photonics has emerged as a preeminent platform for photonic integration, offering a suite of distinctive advantages. These include the potential for large-scale integration, cost-effective production methods (Suzuki et al., 2017), superior optical properties, and compatibility with complementary metal-oxide-semiconductor (CMOS) technology (Wenqi et al., 2022). Despite the excellent properties of silicon-based platforms, the indirect bandgap structure of silicon prevents the efficient emission of light (Y. Han et al., 2022; Siew et al., 2021). Future advanced applications require multiwavelength laser sources on silicon chips (Marinins et al., 2023).

Efforts were made to monolithically build active devices such as laser sources and semiconductor optical amplifiers (SOAs) directly onto the silicon photonics layer (Franck Chollet, 2016). However, the lattice mismatch between the silicon and active device layer causes defects that shorten the lifetime of the devices (Kaur et al., 2021). Also, this method has low yield (Billah et al., 2018). Thus, active devices are generally made on external substrates that have a direct bandgap, such as indium phosphide (Richard et al., 2019). Therefore, there is a need to integrate externally fabricated chips into silicon-based platforms, and approaches such as heterogeneous (Chao Xiang et al., 2023) and hybrid (Theurer et al., 2020) integration are commonly used. Heterogeneous integration, whether it is based on die/wafer bonding or micro-transfer printing, bonds the active chip during the wafer bonding cycle. Due to the fact that active devices are not completely processed before integration, this method presents a limitation in pre-testing the active chip prior to its integration. Consequently, it is challenging to assure the functionality of the active chip, as its performance cannot be fully verified in advance. Besides, the throughput is also low (Y. Han et al., 2022). Hybrid integration is

normally based on flip-chip or wafer bonding techniques made with fully processed active chips, therefore it gives the opportunity to only integrate functional devices. Hybrid integration of lasers outperforms all the other methods with respect to linewidth (C. Xiang et al., 2022). Nevertheless, this method requires a stringent assembly process to maintain alignment during the bonding of the active devices (Bian et al., 2023). The alignment accuracy depends on both the fabrication tools and the bonding equipment (Li et al., 2022), which makes the alignment quite challenging (Moody et al., 2022), expensive (Z. Zhou et al., 2023) and time-consuming (Shakespeare, Pearson, Grenestedt, Hutapea, & Gupta, 2005). Recently, photonic wire bonding was developed to mitigate alignment issues. However, this technique requires a complex manufacturing process with several elaborate steps (Billah et al., 2018). Hence, the availability, reliability and production yield need further investigation. As such, the efforts to achieve high laser attach throughput and high precision alignment persist to solve this major challenge to the deployment of silicon photonics (Bian et al., 2023).

Therefore, there is a need for an accessible and reliable dynamic integration method that does not rely on the accuracy of bonding equipment, and that is able to integrate known-good active chips. Microelectromechanical systems (MEMS) could be the right candidate for this approach.

MEMS actuators with multiple degrees-of-freedom (DOF) were reported previously in the literature (Ba-Tis & Ben-Mrad, 2015; Espinosa et al., 2014; Mukhopadhyay, Dong, Pengwang, & Ferreira, 2008). These devices are referred to as positioners or aligners. They have been used in a variety of applications that include waveguide or optical fiber control, due to their small size, manageable power consumption and ease of fabrication using well-developed semiconductor fabrication facilities (Maroufi, Fowler, & Moheimani, 2017). For instance, in (Sharma, Kohli, Brière, Nabki, & Ménard, 2022), a MEMS-driven silicon photonic switch was reported, where an optical signal is selectively passed to one of three output channels. In (Bezzaoui & Voges, 1991) a silicon-oxide-nitride waveguide was proposed for optical/micromechanical sensors. In (Hamed et al., 2022; Ikeda & Hane, 2013b), MEMS

tunable optical filters were proposed. The MEMS actuators were used to displace freestanding waveguides to change the optical path length of microrings, which leads to a change in the resonant wavelength. In (Haake & Beranek, 1998; Henneken, Tichem, & Sarro, 2006), MEMS actuators were used to control an optical fiber and align it to a laser diode chip to improve coupling efficiency. For photonic hybrid assembly applications, a MEMS positioner was proposed in (Wörhoff et al., 2016), where in-plane and out-of-plane MEMS actuators were used to control silicon-based waveguides and align them to an indium phosphide active chip, on a common carrier. With the help of eutectic AuSn bonding and a pick-and-place tool, the active and silicon chips were assembled onto the carrier by using flip-chip-bonding within an initial alignment accuracy of 2 to 5 µm. Due to the fine alignment carried by the MEMS actuators, a final alignment between the active chip and silicon chip waveguides within ±100 nm was achieved. In (X. Liu et al., 2007), a 3-DOF electrostatic nano-positioner was reported for applications in micro and nanotechnologies. In (Niels Quack et al., 2023), several MEMS tuned photonic devices were fabricated using IMEC's iSiPP50G platform (Pantouvaki et al., 2017), and experimentally demonstrated for different applications that involve physical displacements, such as optical power distribution (Sattari et al., 2020) and switching, phase shifting (Edinger et al., 2021), and wavelength selective operations (Hamed et al., 2022). For the optical power distribution detailed in (Sattari et al., 2020), out-of-plane MEMS actuators were used to control directional couplers suspended in air in order to change the coupling gaps, making the input power available in the desired output waveguide. For phase shifting (Edinger et al., 2021), a MEMS-controlled waveguide was used to tune the phase by changing the effective index as the gap between suspended and fixed waveguides was changed.

Despite extensive research on multiple DOF positioners, the incorporation of out-of-plane and in-plane translations remains relatively uncommon, primarily due to the intricate design and fabrication differences between the two motion types (Y. S. Kim et al., 2014). Accordingly, this is the focus of this work, specifically for application in optical chip-to-chip alignment for photonic integrated circuits (PICs). In contrast to commonly used integration methods that cannot mitigate any misalignment that occurs after packaging, MEMS positioners can be leveraged during the packaging of PICs and throughout their lifetime to improve the ±1 µm

alignment accuracy provided by conventional flip-chip-bonding (FCB) (C. Yang et al., 2023). The success of co-integrating movable waveguide systems with mechanically controlled switches inspired this work to design MEMS actuators to control suspended waveguides for efficient chip-to-chip alignment.

Regarding actuator design, to achieve out-of-plane motion, piezoelectric actuators exhibit nonlinear behavior, and cannot readily provide large displacements (Algamili et al., 2021). Alternatively, electrostatic actuators require the use of top and bottom parallel plates (Aryal & Emadi, 2020; Sano, Ataka, Hashiguchi, & Toshiyoshi, 2020), or staggered comb fingers (T. Kim & Gorman, 2022; Nabavi, M, x00E, nard, & Nabki, 2022). While electrostatic actuators have been widely used due to their low power consumption, high speed, and support for large displacements (Manosalvas-Kjono, Quan, & Solgaard, 2022), the need for high actuation voltages limits their practicality (Sano et al., 2020). In contrast, electrothermal actuators, which can be manufactured relatively simply, require a low actuation voltage and can generate significant deflections (Potekhina & Wang, 2019). Consequently, this type of actuators will be considered here.

Buckled beam electrothermal actuators (Cragun & Howell, 1999; Syms & Liu, 2022) have been used to generate in-plane motion, where a set of V-shaped or commonly-known as chevron-type thermal actuators are employed. These actuators exhibit high thermal forces (Que, Park, & Gianchandani, 1999; Sinclair, 2000), resulting in large deflections. Generally, they are composed of two joined arms angled to guide the direction of the motion in-plane upon joule heating (Sanjay Joshi, Mohammed, & Kulkarni, 2018). In (Barazani et al., 2023), three chevron actuators were used to drive the waveguides of an optical switch. Two back-to-back chevron actuators were used to compress and amplify the in-plane displacement of a middle chevron that is attached to a waveguides-carrying movable platform. To generate out-of-plane motions using electrothermal actuators, a common thermal bimorph is used in (T.-J. Peters & Tichem, 2016a) for chip-to-chip alignment.

Accordingly, this chapter proposes an electrothermal 3-DOF micro-positioner. While the device can have potential application as an optical aligner in PICs, this work focuses of the design and mechanical characterization of the actuators. The device relies on push-push in-plane thermal chevron actuators to buckle supporting beams and generate out-of-plane motion. The chapter is structured as follows: section 5.2 presents the design and the simulation. Section 5.3 describes the device fabrication and characterization. Section 5.4 presents and discusses the measurement results, and is followed by a conclusion and a summary of the chapter.

5.4   Device design and simulation

A 3D schematic of the electrothermal micro-positioner is shown in Figure 5.1. The micro-positioner consists of a platform anchored in four distinct locations by three thermal chevron actuators and a serpentine beam. The thermal chevron actuators are used to displace the platform along 3 axes, i.e., the x-, y-, and z-axis.

The serpentine beam is 10 μm-wide and 10 μm-thick (i.e., same thickness as the device layer). It is employed to provide an optical path that can support an integrated waveguide, as described in the alignment strategy sub-section. Its design, characterized by multiple 180º bends,
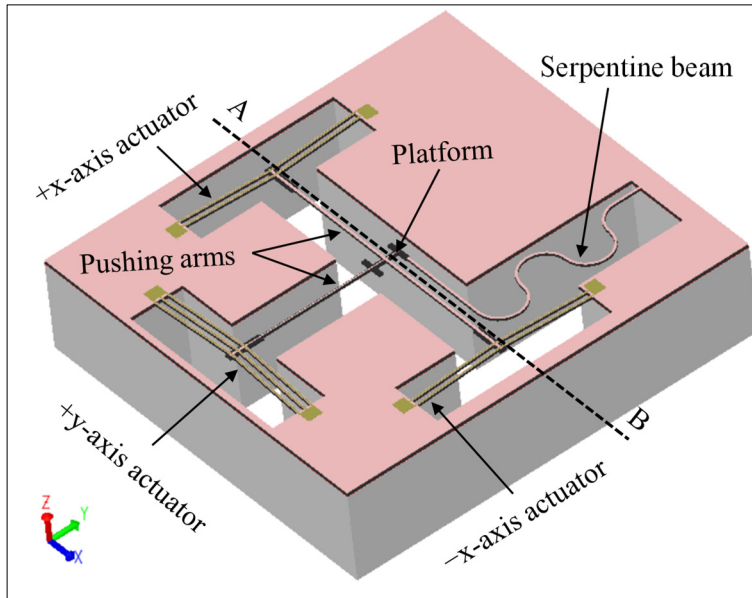
Figure 5.1 3D schematic of the electrothermal micro-positioner

emanates from the dual necessity of a waveguide support with low stiffness in all three principal motion axes and the constraints imposed by the minimum bending radius to ensure minimal optical losses due to waveguide bends. This allows to fulfill both mechanical and optical prerequisites simultaneously. This ensures that the beam supporting the waveguide does not require large forces to be displaced, and that it can thus provide sufficient displacements with the included actuators.

The integration of the waveguide could be performed in a similar fashion to that presented in (Sharma et al., 2022). The individual thermal chevron actuators are labeled +x-axis actuator, −x-axis actuator and +y-axis actuator, respectively, in Figure 5.1. The later actuator consists of three chevron legs whereas the x-axis actuators have only two legs to reduce the x-axis stiffness. As delineated in (Rabih, Sharma, Pita, Ménard, & Nabki, 2023), a linear augmentation in the count of chevron beams correlates with an increase in actuation power. However, the resultant displacement enhancement is relatively modest when contrasted with the escalation in power consumption. This limited displacement can be attributed primarily to the concomitant increase in stiffness. In a related observation, variations in the width of the beams connecting the x-axis actuators to the platform, specifically ±2 μm from their nominal 10 μm width, were found to exert negligible impact on the overall performance. The actuation of the +x-axis actuator and −x-axis actuator results in deformation of the platform along the positive and negative x-axes, respectively. Similarly, activating the +y-axis actuator provides positive movement along the y-axis. In order to achieve an out-of-plane deflection, the +x-axis and −x-axis actuators are actuated simultaneously with the same actuation power to generate opposing forces (i.e., along the positive and negative x-axis). This results in a buckling phenomenon that moves the platform vertically towards a point away from the substrate. To manage the power consumption, it could be warranted to include locking or latching mechanisms that could temporarily fix the aligned waveguides during operation while disabling the actuators. This could be the focus of future work.

5.4.1   Operating principle of the out-of-plane actuation

A diagram illustrating how the out-of-plane displacement of the platform is generated is shown in Figure 5.2. As shown in Figure 5.2(a), the platform is attached to two pushing arms connected to the two x-axis actuators.

All suspended structures exhibit an inherent residual stress that leads to deflections of the arms in the out-of-plane direction, resulting in an initial offset angle θ, as illustrated in Figure 5.2(b) (Chien, Su, Wang, Gan, & Wang, 2017). The offset angle is approximated based on the radius of curvature R and the original length of the deformed arm L, as given by (Chien et al., 2017):

$$\theta = L/R \tag{5.1}$$

When R is significantly larger than L, R can be determined from the initial vertical deflection, Δz, of the deformed structure using:

$$R = L^2/2\Delta z \tag{5.2}$$
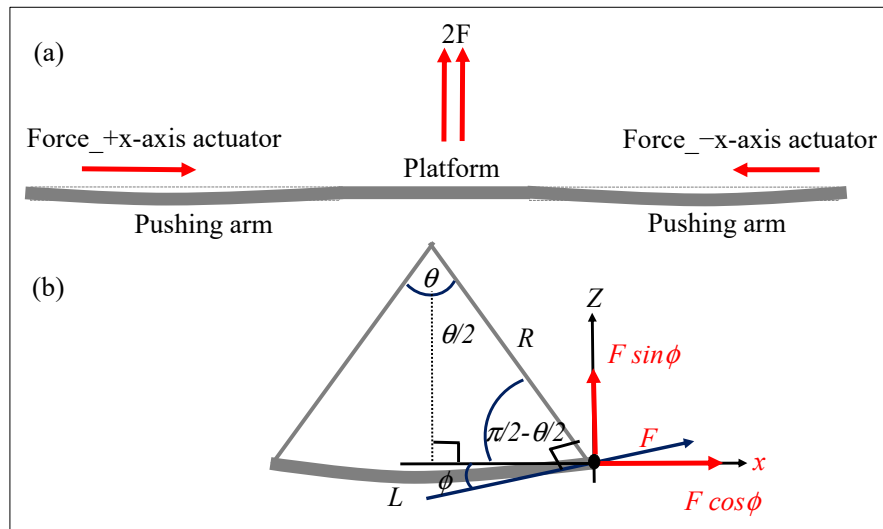
Figure 5.2 Side view diagram outlining (a) the two opposing in-plane forces acting on the platform to generate the out-of-plane buckling forces and (b) illustration of the arms bending under stress and of the x and z-axes components of the generated lateral force

The relation between θ and ϕ, the complementary angle of $\theta/2$, to decompose the lateral force into its x- and z-axes components is based on trigonometric principles illustrated in Figure 5.2(b), and can be given by:

$$F_{total} = 2F \sin\left(\theta/2\right)$$ (5.3)

The z-axis force that generates the out-of-plane motion of the platform, F_{total}, can thus be isolated. This force is equal to twice the net force in the out-of-plane direction, due to the cancelation of the two opposite in-plane (i.e., x-axis) forces.

5.4.2   Finite element analysis (FEA) simulations

The electrothermal actuator is designed using a silicon-on-insulator (SOI) device layer with a thickness of 10 μm following the PiezoMUMPs process design rules provided by MEMSCAP (Cowen et al., 2014). This process has been selected to fabricate the proposed devices and will be described later. The dimensions of the electrothermal actuator are summarized in Table 5.1.

 The behavior of the electrothermal actuator was surveyed using FEA simulations carried out with the CoventorWare software. Figure 5.3 (a) shows the undeformed shape with a 0.3 μm initial out-of-plane deformation due to residual stress. Figures 5.3(b) and (c) show the first two resonant modes of the micro-positioner. In Figure 5.3(b), simulations predict that the fundamental mode is at 21.77 kHz, whereas in Figure 5.3(c), the second mode occurs at 33.55 kHz. As explained above, the out-of-plane displacement along the z-axis is generated by applying two equal and opposite in-plane forces along the x-axis. This phenomenon is shown in Figure 5.3(d), where applying 0.5 V leads to over 7 μm of upward displacement of the platform. Before 0.4 V and prior to buckling, the displacement is very small as shown in Figure 5.3(e). This upward displacement confirms the direction of the buckling as demonstrated by the following experimental data, and shows the novelty of the design. Note that displacements along the other axes, while buckling is achieved, is minimal as shown in Figure 5.3(e).
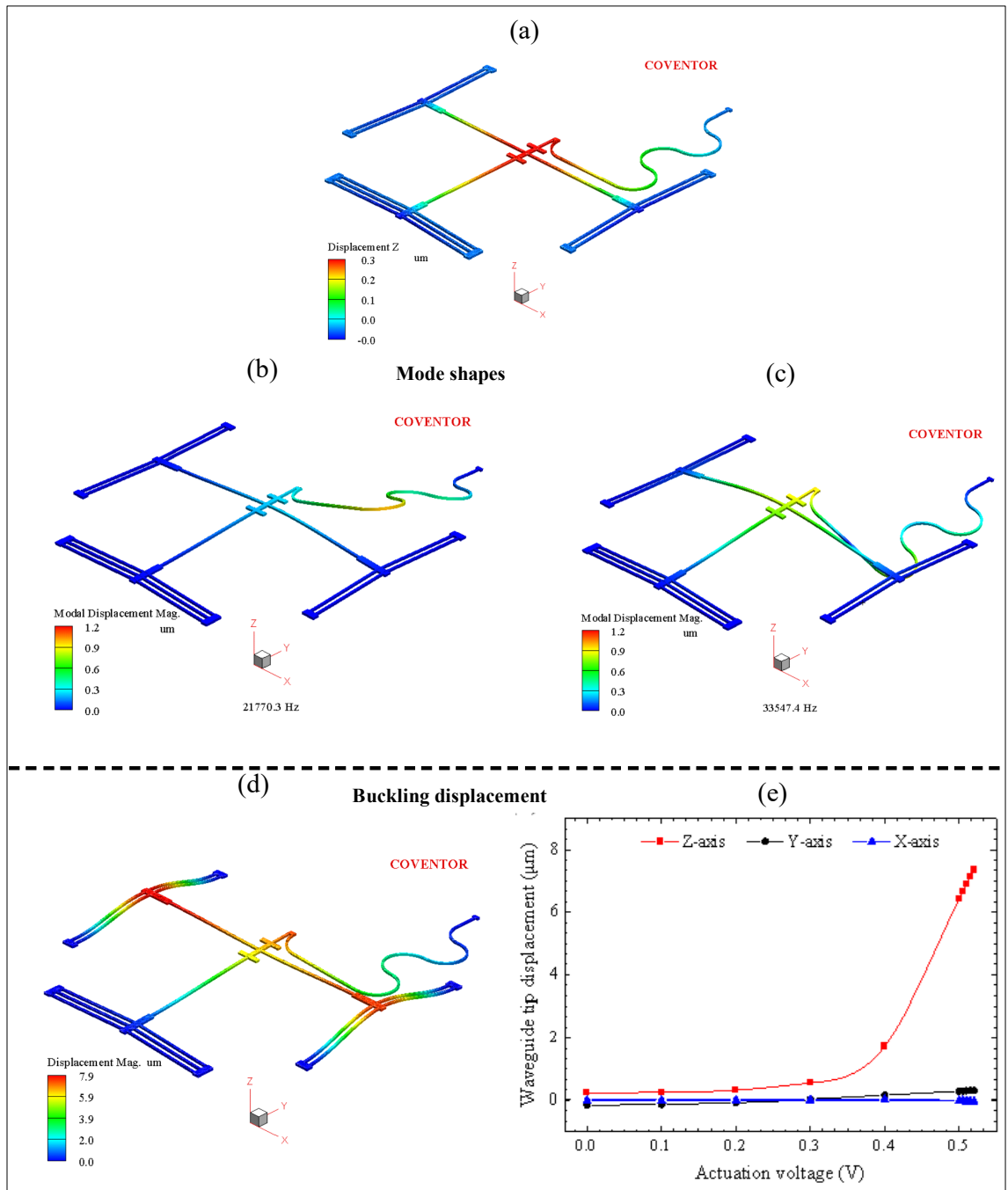
Figure 5.3 FEA simulations showing the (a) undeformed shape with 0.3 µm initial out-of-plane deformation due to residual stress, (b) the first resonant mode, (c) the second resonant mode, (d) the static actuation to buckle the structure at 0.5 V, and (e) the waveguide tip displacement vs. the actuation voltage

5.4.3   Alignment strategy and displacement cross-sensitivity

The ultimate goal of this work is to develop a waveguide positioner for chip-to-chip alignment in PICs. The success of co-integrating movable waveguide systems with mechanically controlled switches inspired this work to design MEMS actuators to control suspended waveguides for efficient chip-to-chip alignment. Therefore, in this section the methodology that will be used to achieve this objective is explained.

Figures 5.4(a) and (b) show diagrams of how the waveguide (WG) would be integrated onto the device. Figures 5.4(c)-(g) show simulation results of the displacement and cross-sensitivity with and without the waveguide structure, the latter being what is experimentally tested in section IV, and Figures5.4(h)-(l) show a close-up view of the waveguide in different actuation states.

The structure of the suspended WG on top of the serpentine beam is a 500 nm-wide and 400 nm-thick nitride core on top of 8 μm-wide and 3 μm-thick oxide. This WG is made on the silicon chip to align it to a fixed WG of an active chip placed slightly away from the suspended WG in the longitudinal direction, which results in a gap between the chips, as shown in Figures 5.4(a) and (h). In previous heterogenous integration demonstrations, this gap, which is necessary to avoid damaging the facets of the WGs, was 3 – 7 μm (Matsumoto et al., 2019), and it is a source of optical losses. Moreover, since the micro-positioner can move over large vertical distances, but only in the positive direction, the integration process for the active chip with the silicon photonics chip, encompassing the suspended waveguide and MEMS actuators, involves utilizing a common platform designed with etched grooves to house the active chip. Initially, alignment tools are employed to position the waveguide of the active chip approximately 4.0 ± 1.0 μm above the silicon chip. To accommodate the active device, the depth of the cavity etched into the silicon aims to align closely with this specified height. This

Table 5.1 Dimensions of the device

Part	Dimension (μm)
Actuator beam length	400
Actuator beam width	10
Pushing arms length	500
Pushing arms width	10
Device thickness	10

adjustment falls within the linear operational range of the actuators, thereby ensuring their effective use. Subsequent to this initial alignment, the chips undergo a second phase of alignment. In this phase, the actuators are activated to finely adjust the position of the suspended waveguide along the xyz-axes, ensuring precise alignment.
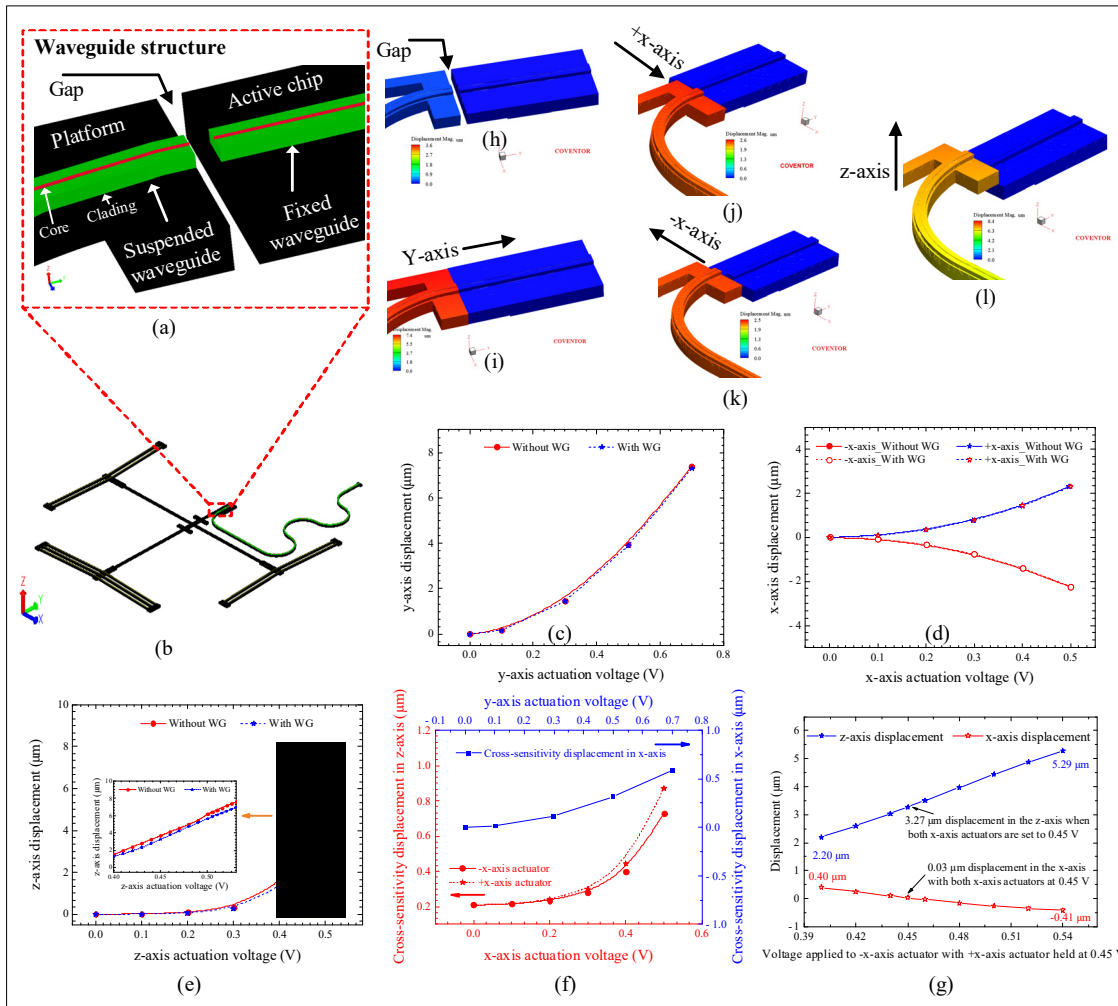
Figure 5.4 Alignment strategy: (a) and (b) schematic of the waveguides and the entire positioner, respectively, (c) in-plane displacement in the y-axis, (d) in-plane displacement in the x-axis ,(e) out-of-plane displacement in the z-axis, (f) cross-sensitivity displacements in the z-axis due to x-axis actuation and in the x-axis due to y-axis actuation, (g) displacements in the x-axis and z-axis due to different voltages at -x-axis actuator, (h) waveguides at rest state with gap open, (i) activating the y-axis actuator and closing the gap, (j) and (k) moving the waveguide in the x-axis, and (l) moving the waveguide in the z-axis.

To mitigate the loss due to the gap, the y-axis actuator is activated to gradually close it (Figure 5.4(i)) and bring the suspended WG into close contact with the WG of the active chip. Figure 5.4(c) shows the WG displacement versus the actuation voltage. To close a 7 μm gap, less than 0.7 V is required. When there is no WG (Without WG) on top of the serpentine beam, a displacement of 7.39 μm was achieved, whereas with the WG (With WG) a displacement of 7.16 μm was obtained. To tune the light coupling between the WGs, fine lateral and vertical adjustments are performed by activating the x-axis and z-axis actuators. Figure 5.4(d) shows displacements in both the positive and negative x-axis, where more than ±2 μm is achieved at 0.5 V. Figures 5.4(j) and (k) demonstrate moving the WG in the x-axis. Finally, to align the WGs vertically, both x-axis actuators are activated and the suspended WG is moved upward, where large deflections with a linear response are obtained beyond 0.4 V, as shown in Figure 5.4(e). To have efficient vertical alignment, this positioner is operated in the linear region, where in this region the resolution of the z-axis actuator is ~45 nm/mV. Therefore, a precise control of the actuation voltage is required to get efficient coupling. Figure 5.4(l) shows the WG moving vertically along the z-axis.

Figures 5.4(c)-(e) show that the addition of the WG did not significantly influence the displacements, in the y-, x- and z-axes. Furthermore, the cross-sensitivity displacements that occur along the axes other than the axis of actuation were found for the case when the waveguide is implemented on top of the serpentine beam and are shown in Figures 5.4(f) and (g). In Figure 5.4(f), the cross-sensitivity displacements in the z-axis due to activation of the x-axis in both negative and positive directions, and in the x-axis due to actuation of the y-axis are reported. For the displacement in the z-axis, at 0.5 V the lateral displacement is ±2.29 μm (Figure 5.4(d)) whereas the z-axis displacement is 0.59 ± 0.10 μm (Figure 5.4(f)). This out-of-plane cross-sensitivity is due to the heating of the layers with different coefficients of thermal expansion, leading to a thermal bimorph effect that generates out-of-plane deflections (X. Zhang et al., 2016). Nevertheless, this vertical displacement still puts the waveguide below the 4 μm target z-axis range of the fixed waveguide. Thus, by controlling the relative voltage difference between both lateral actuators, the waveguide on the silicon chip can be aligned

laterally and vertically with the fixed one. For the displacement in the x-axis due to y-axis actuation, at 0.7 V, which provided a longitudinal displacement of 7.16 μm (Figure 5.4(c)), a cross-sensitivity lateral displacement of 0.60 μm (Figure 5.4(f)) in the x-axis was seen. This can be compensated by increasing the voltage on the -x actuator. The lateral displacement is caused by a rotation around the z-axis caused by the single serpentine beam used to carry the WG. Adding another serpentine beam could resolve this cross-sensitivity without having to significantly increase the actuation power.

Figure 5.4(g) illustrates the simulated displacement of the device along the z- and x-axes under varied x-axis actuator voltages. Initially, both actuators were set at 0.45 V, achieving a 3.27 μm displacement along the z-axis with minimal cross-sensitivity (i.e., 0.03 μm) in the x-axis. Subsequently, while maintaining the +x-axis actuator at 0.45 V, the -x-axis actuator voltage was adjusted above and below this value. At a reduced -x-axis actuation of 0.4 V, we observed 0.4 μm and 2.2 μm displacements in the x- and z-axes, respectively. Interestingly, setting both x-axis actuators to 0.4 V resulted in displacements of 0.03 μm (x-axis) and 1.51 μm (z-axis). Increasing the -x-axis actuator to 0.54 V led to displacements of -0.41 μm (x-axis) and 5.29 μm (z-axis), with equal 0.54 V actuation on both x-axis actuators yielding -0.04 μm (x-axis) and 7.58 μm (z-axis) displacements. This detailed examination underscores the intricate balance between actuator voltage adjustments and their resultant displacements, offering valuable insights for optimizing the performance of the device. Table 5.2 presents a summary of the x- and z-axes displacements as a function of the voltages applied to the x-axis actuators. The data clearly indicates that activating both x-axis actuators simultaneously is effective in minimizing undesired lateral displacements along the x-axis. Moreover, varying the voltages on the actuators influences the buckling behavior, thereby altering the z-axis displacement. This underscores the necessity for precise voltage control to achieve targeted displacements along one axis while maintaining the position along the orthogonal axis, ensuring high-precision actuation within the system operational parameters.

Table 5.2 Displacements along the x- and z-axes for different
voltages applied to the x-axis actuators

Actuation voltage (V)		Displacement (μm)	
−x-axis actuator	+x-axis actuator	x-axis	z-axis
0.40	0	-1.41	0.25
0.40	0.40	0.03	1.51
0.40	0.45	0.40	2.20
0.45	0	-1.81	0.30
0.45	0.45	0.03	3.27
0.54	0	-2.54	0.93
0.54	0.45	-0.41	5.29
0.54	0.54	-0.04	7.58

A 3D finite-difference time-domain (FDTD) optical simulation at a telecom wavelength of 1550 nm was performed using the Lumerical software to assess the effects of 2D misalignments, while maintaining constant alignment along the third axis. The results, depicted in Figure 5.5(a), present the loss along the y- and z-axes, assuming perfect alignment along the x-axis. It is important to note that light propagation occurs along the y-axis, with the z-axis representing an out-of-plane direction and the x-axis indicating lateral in-plane alignment. For maximum misalignments of ±1 μm in both the y- and z-axes, a loss ranging from
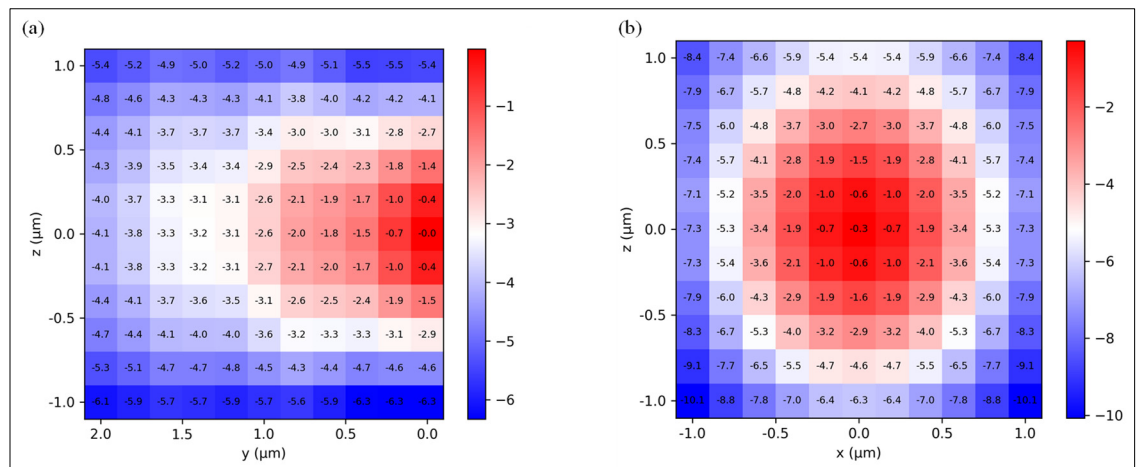
Figure 5.5 Loss in optical waveguides at 1550 nm due to (a) misalignments along the y- and z-axes, with perfect alignment assumed along the x-axis, and (b) misalignments along the x- and z-axes, with a constant 0.1 μm gap maintained along the y-axis.

approximately -5.7 dB to -5.0 dB was observed. By minimizing misalignments to within ±0.1 μm in both axes, the loss could be reduced to below -1.0 dB. Further analysis shown in Figure 5.5(b) examines the loss along the x- and z-axes, with a fixed gap of 0.1 μm between the waveguides along the y-axis. Achieving a misalignment of ±0.1 μm across all three axes yielded a loss of less than -0.6 dB. Note that reducing the 0.1 μm gap further could be feasible through precise etching of the waveguide facets at right angles, indicating that gaps and misalignments smaller than those achievable with conventional pick-and-place equipment are attainable.

When the optimal alignment is reached, having a locking mechanism that allows for the deactivation of the actuators would significantly reduce the power consumption. This can be done in different ways. For instance, in (Unamuno, Yao, & Uttamchandani, 2005), ultraviolet curing of optical quality adhesives was used to permanently fix a movable optical fiber after optimally aligning it to another fixed fiber using electrothermal actuators. In (Henneken et al., 2008) and (Q. X. Zhang et al., 2010), mechanical locking mechanisms were used to maintain the alignment after deactivating the actuators. In (Henneken et al., 2008), electrothermal actuators were used to align two optical fibers to each other, whereas in (Q. X. Zhang et al., 2010) a discrete-laser diode was aligned to a silicon waveguide.

5.5   Microfabrication

As mentioned in section 5.4.2, the electrothermal micro-positioner was fabricated using the PiezoMUMPs process. This process starts with a 150 mm handle wafer with a (100) orientation and a thickness of 400 μm. As shown in the cross-section view in Figure 5.6, the silicon device layer is 10 μm thick and the buried oxide (BOX) insulation layer has a thickness of 1 μm. To form the pads and make electrical connections, a metal stack of 20 nm of chrome and 1 μm of aluminum (Al) is used. The stack is deposited over a 0.2 μm-thick oxide serving as an insulator. After fabricating the devices, scanning electron microscope (SEM) micrographs were taken to investigate fabrication variations by comparing the fabricated dimensions to their designed values, as shown in Figure 5.7. Variations from the designed dimensions, given in parenthesis

in the figure, were observed. For example, in Figure 5.7(b), the gap was measured to be 5.8 ± 0.1 μm compared to the designed value of 6 μm. In Figure 5.7(c), the widths of the serpentine beam and pushing arm were measured to be 9.4 ± 0.1 μm and 10.4 ± 0.07 μm, respectively, compared to their designed value of 10 μm. In Figure 5.7 (d) the length of the −x-axis actuator was measured to be 395.5 ± 0.7 μm compared to the designed value of 400 μm. These variations were not deemed to be significant, as will be seen in the experimental results.

The focus of this article is on characterizing the actuators to confirm their ability to provide sufficient displacements in the xyz-axes required to resolve the misalignment issues encountered by the current heterogeneous photonic systems. Therefore, the fabricated positioner did not integrate the aforementioned WG. Details on how silicon nitride waveguides are integrated with MEMS actuators to mitigate optical loss is reported in (Rabih, Sharma, et al., 2023). Thus, this work represents the first step towards the creation of an integrated chip-to-chip alignment system, as it presents the groundwork to move the waveguide and optically align it with an adjacent chip in future work. In prior work, we experimentally demonstrated that the optical transmission between waveguides is significantly influenced by out-of-plane misalignments and the size of the residual longitudinal gap. Reducing the gap between the waveguides from ~ 6.9 μm down to ~ 0.6 μm, led to an average decrease in the transmission loss of 6.3 dB, as demonstrated in (Rabih, Sharma, et al., 2023). Furthermore, the three 2D
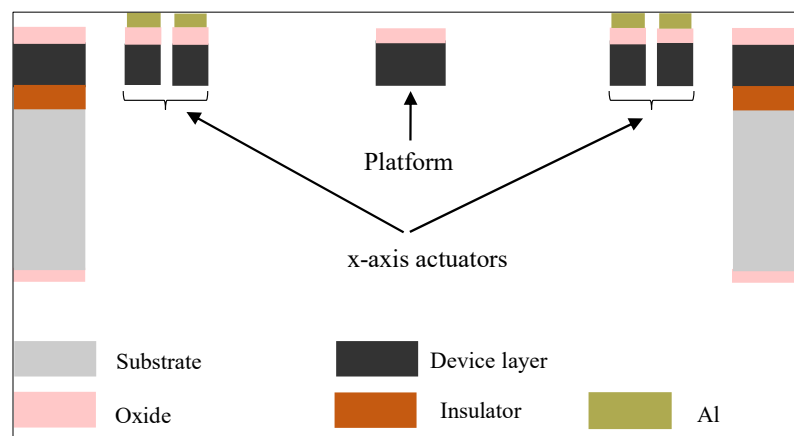
Figure 5.6 Cross-section A—B of the positioner shown in Figure 5.1, showing the layers used to fabricate the device
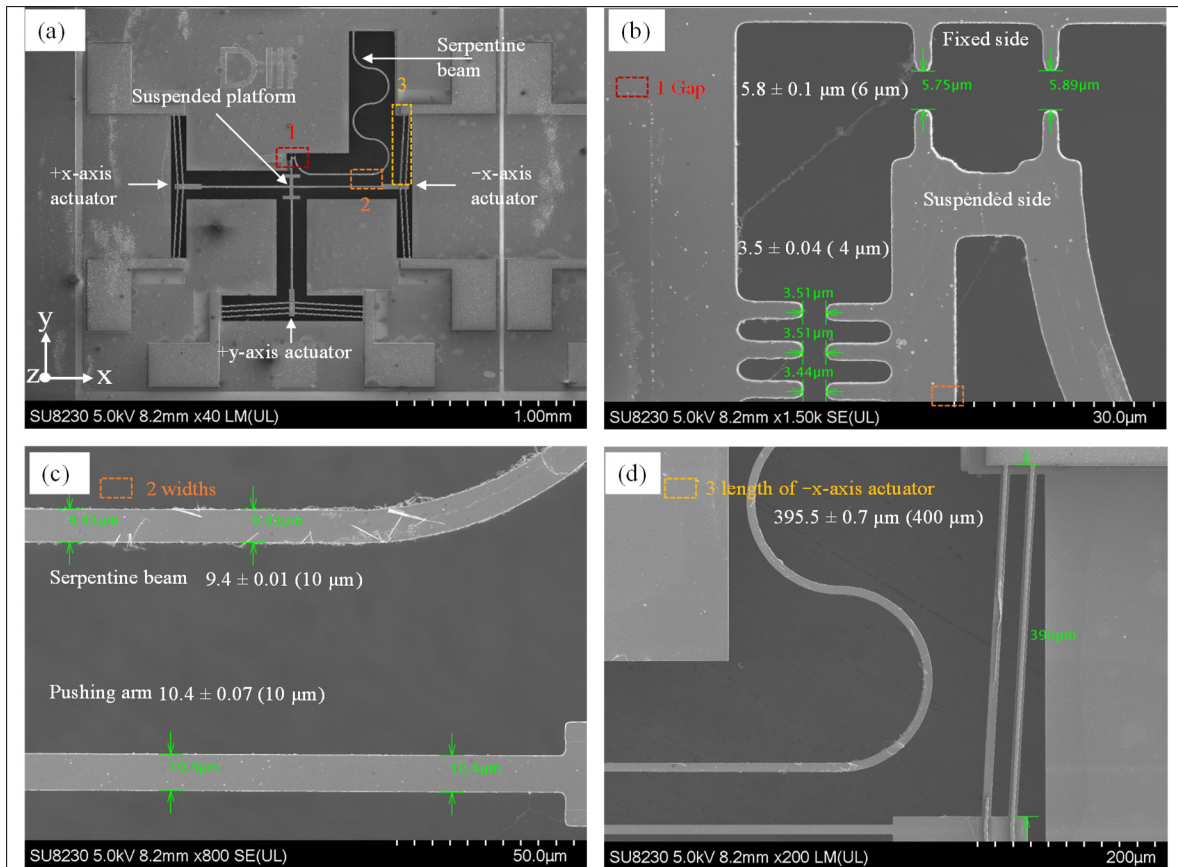
Figure 5.7 SEM micrographs showing the platform and optical path of the fabricated device, (a) the entire micro-positioner (b), the gap between the suspended platform and the fixed side of the micro-positioner, (c) the widths of serpentine beam and pushing arm and (d) the length of −x-axis actuator

positioners that were characterized had different out-of-plane misalignments due to fabrication variations. The values measured for the three devices were 345 ± 52 nm, 482 ± 29 nm and 521 ± 43 nm, respectively. They resulted in average normalized optical transmissions of -1.60 ± 0.06 dB, -1.70 ± 0.03 dB and -1.86 ± 0.02 dB, respectively. This clearly shows that incorporating 3D MEMS positioners that could mitigate the out-of-plane misalignment will improve the transmission loss as the simulation also predicts. Thus, this work represents the first step towards the creation of an integrated chip-to-chip alignment system, as it presents the groundwork to move the waveguide and optically align it with an adjacent chip in future work.

5.6   Experimental results and discussion

5.6.1   Experimental setup

A schematic of the experimental setup employed to characterize the fabricated electrothermal actuator is shown in Figure 5.8. The MEMS device under test (DUT) was bonded onto a specially-designed printed circuit board (PCB). The PCB facilitated handling of the micro-positioner and provided connections to external voltage sources. During the characterization process, actuation voltages ranging from 0 to 1 V were applied to the terminals of the actuators in 0.1 V increments. Ammeters were used to measure the resulting power consumption. To measure the displacement along the 3 axes, a LEXT 3D microscope was used to capture images of the device in its initial state (when the actuators were inactive) and under different actuation conditions. Each image was then processed using the microscope image analyzer software on a PC to measure the displacement. The LEXT 2100 laser microscope used employs a dual confocal system, incorporating two confocal optical light paths. This is done in combination with a high sensitivity detector for precise 3D microscope images from a sample consisting of materials with different reflectance characteristics, as described in ("LEXT OLS4100 3D measuring Laser microscope," 2005). The in-plane displacements along the x- and y-axes were
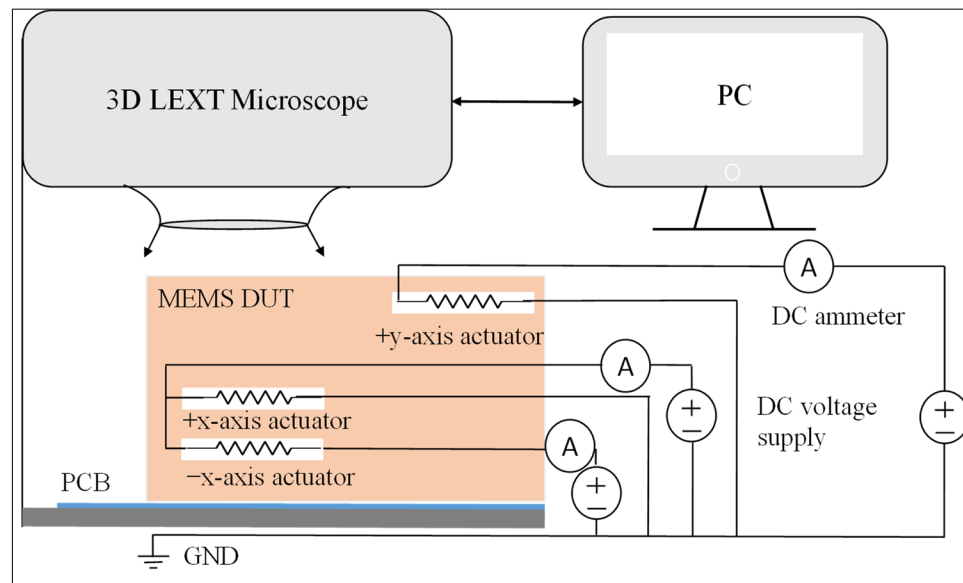
Figure 5.8 Schematic of the experimental setup

measured on the captured image using the length of a line between two points, one being the edge of the platform, whereas the out-of-plane displacement in the z-axis was measured from the step height of the platform with regard to a reference point on the surface of the die, as shown in Figure 5.9(a). A thorough explanation of the z-axis displacement measurement is reported in (Rabih, Kazemi, et al., 2023).

The AC characterization was done with a laser Doppler vibrometer (OFV2570 controller and OFV-534 laser unit) manufactured by Polytec. In this regard, the y-axis actuator was driven by an AC signal with an amplitude of 0.1 V and a frequency varying from 13 to 25 kHz.
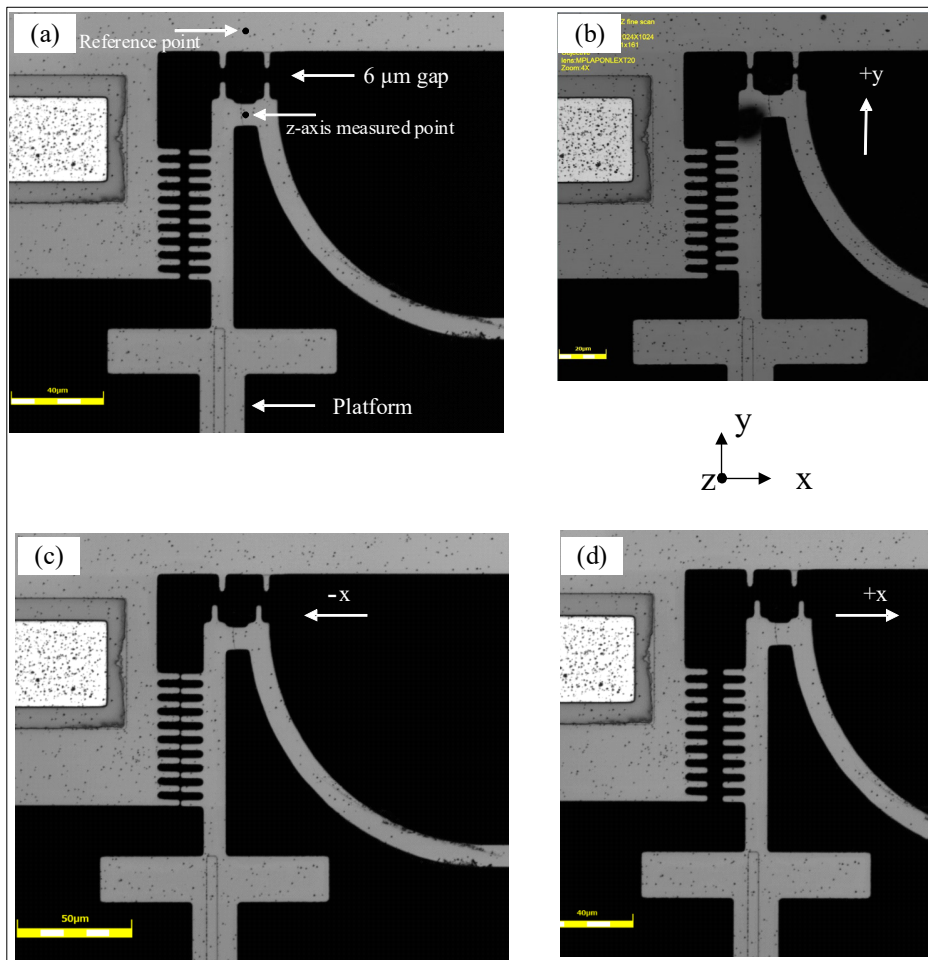
Figure 5.9 Optical images showing (a) the initial state when all actuators are inactive, (b) the 1 V activation of +y-axis actuator, (c) the 1 V activation of −x-axis actuator, and (d) the 1 V activation of +x-axis actuator

5.6.2   Results and discussions

To illustrate the ability of the 3D electrothermal micro-positioner to provide both in-plane and out-of-plane motions, optical images captured by the microscope are shown in Figure 5.9. In Figure 5.9(a), all of the actuators were inactive, showing the initial gap of 6 μm. In Figure 5.9(b), only the +y-axis actuator was activated to close the initial gap in the direction of the positive y-axis. In Figure 5.9(c), the platform was displaced towards the negative x-axis by activating the −x-axis actuator, whereas in Figure 5.9(d), the platform was displaced in the direction of the positive x-axis by activating +x-axis actuator.

Figure 5.10(a) illustrates the measured and simulated in-plane displacement along the x-axis for various actuation voltages. In this graph, the −x-axis actuator and +x-axis actuator were actuated separately. It can be seen that both actuators are able to provide the same in-plane motion, i.e., 3.35 μm, but in a different direction, once activated by a DC voltage of 1 V. This is due to the two similar thermal chevrons along the x-axis, and the symmetrical structure of the micro-positioner along this axis. Considering motion in both directions, the device offers a total travel range of 6.7 μm along the x-axis. In Figure 5.4(d), the simulations demonstrate that a voltage of only 0.5 V is required to achieve a displacement of approximately 2.3 μm in the x-axis. The necessity for higher voltages in the experimental devices is primarily due to the voltage drop across the pads and connecting wires, which exhibit a resistance of approximately 7 Ω. This resistance was considered in the simulations, as shown in Figure 5.10(a) and the subsequent figures. Moreover, the remaining difference between the experimental results and the simulations may be attributed to other factors not included in the model, such as heat convection and the temperature dependence of material properties.

Figure 5.10(b) demonstrates the power dissipated by these two actuators under different actuation voltages. According to this figure, at the maximum input voltage of 1 V, which results in a deflection of ±3.35 μm, the electrothermal micro-positioner consumes 105 mW. In addition, for different excitation voltages, as expected, both thermal chevrons have similar power consumptions since their geometry is identical.
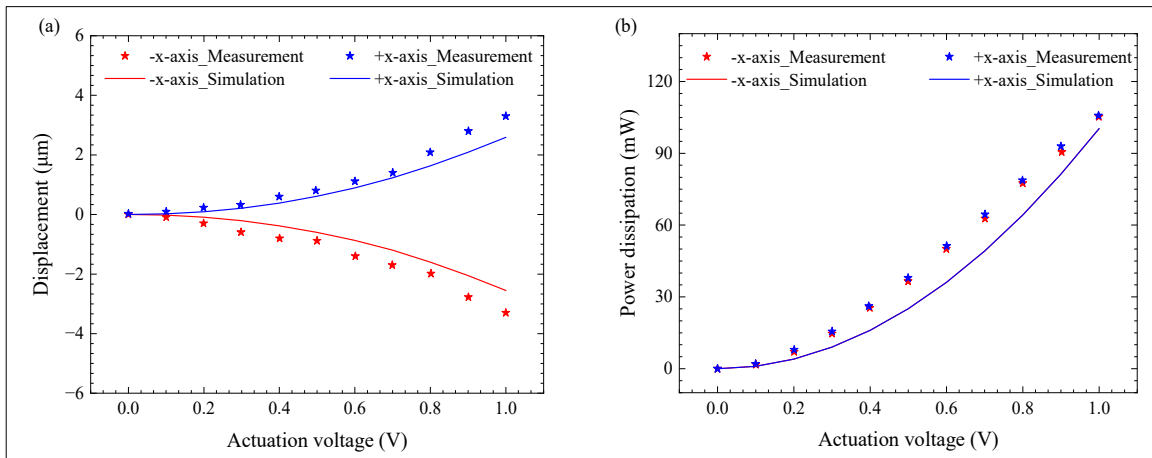
Figure 5.10 Measured and simulated (a) in-plane displacement along the x-axis when the +x-axis actuator and −x-axis actuator are actuated with different DC voltages, and (b) the corresponding power dissipation

Figure 5.11(a) shows the displacement of the electrothermal micro-positioner platform when the +y-axis actuator was excited with different DC voltages. With reference to this figure, the micro-positioner was capable to provide a maximum in-plane displacement of 4.5 µm along the y-axis when it was excited by 1 V. The power dissipated by the +y-axis actuator is shown in Figure 5.11(b). At the maximum input voltage of 1 V, the actuator consumes 140 mW. A comparison between the measured displacements and the power dissipations of the x-axis actuators and the +y-axis actuator indicates that, although the +y-axis actuator can provide a larger displacement, it consumes a higher power because its dimensions are larger than its counterparts.

The ability of the 3D electrothermal micro-positioner to provide out-of-plane motion based on the buckling phenomenon described in Section 5.4.3, is shown in Figure 5.12(a). In this context, both x-axis actuators were operated with identical DC voltages at the same time, and the platform deflection was measured. With reference to this figure, it is clear that upward buckling occurs when the voltage applied to the thermal chevron beams of the x-axis actuators is sufficiently large. In other words, no vertical movement was observed for voltages below 0.3 V, whereas the micro-positioner platform moved considerably upon reaching a voltage of about 0.7 V. Such a nonlinear behavior confirms the buckling phenomenon is occurring in this device. Beyond 0.7 V, the response of the device is linear. The same trend was observed in

simulations. However, the linear range starts at a lower actuation voltage of ~0.4 V. This could be due to the application of the voltage directly at the terminals of the actuators in the simulations, contrary to the measurement where part of the voltage is dropped across the connecting wires prior to reaching the actuators. In addition, simulations did not account for the heat dissipated by air convection, whereas in reality part of the heat will be dissipated
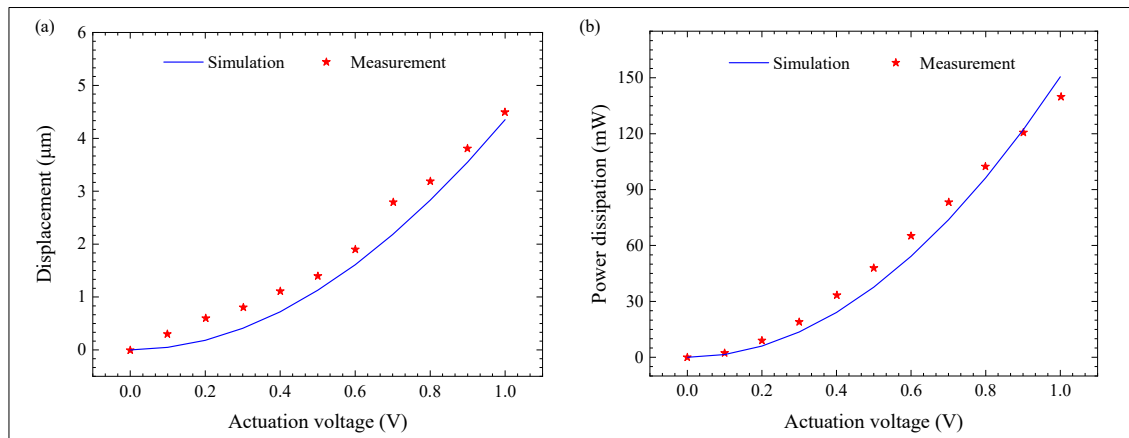
Figure 5.11 Measured and simulated (a) in-plane displacement along the y-axis when the +y-axis actuator is actuated with different DC voltages, and (b) the corresponding power dissipation
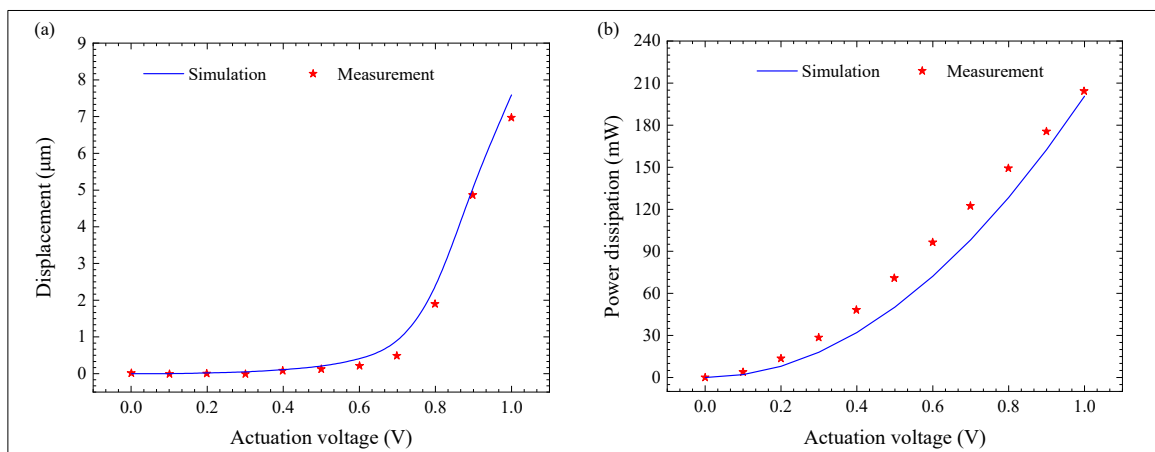
Figure 5.12 Measured and simulated (a) out-of-plane displacement along the z-axis when both +x-axis and −x-axis actuators are activated simultaneously for different DC voltages, and (b) the corresponding power dissipation

causing the displacement to vary for a given voltage, and thus more power will be required to offset the heat convection (i.e., leading to larger voltage requirement).

Figure 5.12(b) shows the power dissipated by the micro-positioner to produce the out-of-plane motion for different excitation voltages (i.e., the power consumed by both x-axis actuators). It is evident that as the input voltage increases, the power dissipation increases in a mostly linear fashion. At the maximum input voltage of 1 V, the power consumption is 210 mW, and a
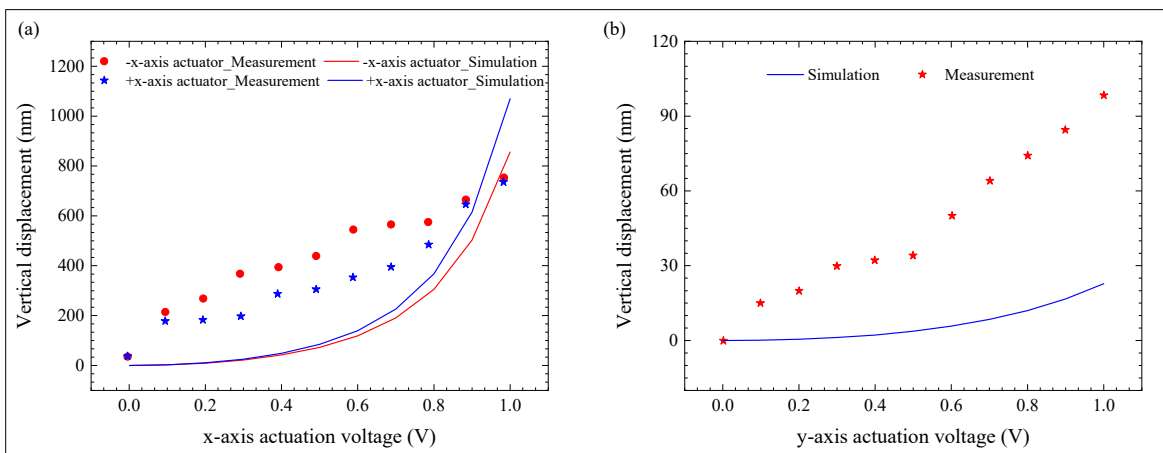
Figure 5.13 Cross-sensitivity of the displacement along the z-axis due to (a) the x-axis actuators, and (b) the y-axis actuator
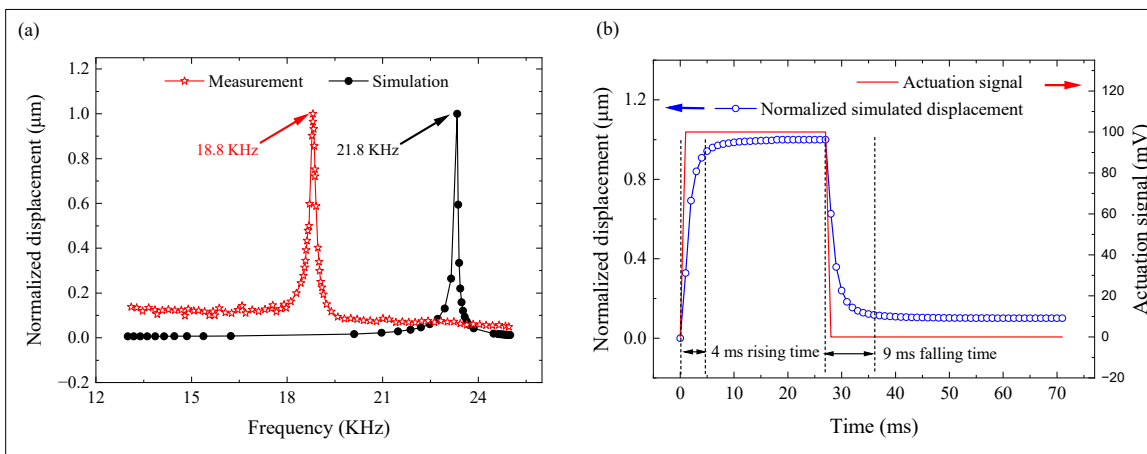
Figure 5.14 Frequency response of the positioner showing (a) the z-axis frequency response obtained by a vibrometer with a measured fundamental mode at 18.8 kHz, and (b) the simulated response time of the z-axis motion in response to a step actuation signal.

vertical deflection of 7 μm is observed. Note that the buckling phenomenon used to produce the vertical motion has no impact on the power consumption of the micro-positioner. The power dissipated for the out-of-plane motion is simply equal to the cumulative power consumed by each of the two x-axis actuators to provide the in-plane motions resulting in the out-of-plane buckling.

Cross-sensitivity between different axes is present, as was predicted by simulations. As illustrated in Figure 5.13(a), the activation of the x-axis actuators induces vertical displacement along the z-axis. Specifically, an x-axis actuator voltage input of 1 V results in a cross-sensitivity displacement of 0.8 μm along the z-axis, while delivering a ±3.35 μm displacement in the x-axis. Conversely, y-axis actuation exhibits negligible cross-sensitivity with vertical displacements. As depicted in Figure 5.13(b), even at the peak y-axis actuator voltage of 1 V, which leads to a +4.5 μm displacement along the y-axis, the cross-sensitivity vertical displacement remains under 100 nm.

Although the simulated and measured displacements closely align in Figures 5.10, 5.11, and 5.12, Figure 5.13 reveals a significant discrepancy between the measured and simulated cross-sensitivity displacements. Given that these displacements occur at the sub-micrometer scale, the observed discrepancy may stem from diminished measurement system accuracy at lower displacement levels. Nonetheless, the overall trend remains similar across both measurements and simulations. Moreover, the remaining difference between the experimental results and the simulations may be attributed to other factors not included in the model, such as heat convection and the temperature dependence of material properties.

5.6.3   Frequency and time responses

Figure 5.14(a) shows the frequency response of the micro-positioner first resonant mode. According to this figure, the micro-positioner is able to provide the maximum out-of-plane deflection at a frequency of 18.8 kHz. A comparison between the resonant frequency estimated

from simulations and the measured one indicates that the simulation model can predict the dynamic behavior of the micro-positioner within a margin of error of 13.6%. It is important to note that the FEM simulator was not configured to extract the quality factor of the device, and a damping ratio of 0.002 was applied to match the measured frequency response shown in Figure 5.14(a).

The response time of the electrothermal actuators is an important characteristic that can be used to determine the speed at which they can be driven. Figure 5.14(b) illustrates the simulated step response of the micro-positioner when both x-axis actuators are subjected to an actuation signal of 100 mV amplitude. Analysis of this figure indicates that the micro-positioner requires approximately 4 ms to attain 90% of its maximum response. Conversely, the simulated fall time to reach 10% of the maximum response post voltage removal is observed to be around 9 ms. Notably, the simulated fall time is more than twice the simulated rise time, potentially attributable to the delayed dissipation of heat accumulated in the actuators. Incorporating heat sinks and modeling heat convection in the design could potentially enhance the fall time.

As mentioned earlier, several micro-positioners that provide motions along multiple axes were reported in the literature. However, micro-positioners that provide translation along three axes are limited. The proposed micro-positioner was compared to published works that report 3-DOF translational motions, as shown in Table 5.3. In this table, the x-axis and y-axis correspond to the in-plane directions, whereas the z-axis corresponds to the out-of-plane direction. The devices were compared based on their displacement (D) provided along the three axes, their actuation voltage (V_{act}) and footprint. As shown in the table, the displacements generated depend on the footprint of the micro-positioner, where micro-positioners with a larger footprint have larger displacements. In (T. Kim & Gorman, 2022), as much as 30 V was required to provide a 0.4 µm out-of-plane displacement along the z-axis, whereas 0.2 µm and 6 µm of in-plane displacements were achieved at 100 V, along the x- and y-axes, respectively. To generate the out-of-plane displacement, the handle layer was used as an electrode to create the bottom comb fingers. The other micro-positioners reported in (Cai et al., 2017; Kazuhiro et al., 2007; Yong Sik Kim et al., 2012; Y. S. Kim et al., 2014; X. Liu et al., 2007; Tian et al.,

2020) provide higher in-plane and out-of-plane displacements at relatively higher actuation voltages. Furthermore, these micro-positioners have very large footprints, and are challenging to fabricate. For instance in (X. Liu et al., 2007), while the in-plane displacements are generated by in-plane comb-drives, to generate the out-of-plane displacement, top and bottom parallel plates were used to generate an out-of-plane force. Therefore, since multiple layers are required, the fabrication process is more complex. Also in (Kazuhiro et al., 2007), the out-of-plane displacement was generated by a complex fabrication process that uses double SOI layers with a thickness of 50 μm and 40 μm and a substrate of 100 μm. Deep ion reactive etching was performed on all these three layers to form staggered combs and realize the out-of-plane displacement. The piezoelectric based positioners shown in (Cai et al., 2017; Tian et al., 2020) are bulky devices due to their applications in scanning probe microscopy that requires large displacements. In addition, the actuators were activated in their dynamic modes. As our positioner exhibits a 4 ms simulated response time and a fundamental resonance frequency of 21 kHz, it will be sufficiently fast to react to drift and most mechanical motions affecting the active chip. Environmental mechanical vibrations typically occur in the range of 2 Hz to 2 kHz (Tanner et al., 2000). Previous positioners described in (Cai et al., 2017) and (Tian et al., 2020) reported 62 ms and 9 ms settling times, respectively, which is significantly longer than the 4 ms simulated response time of the device presented here.

A figure of merit (FOM) defined by the maximum displacement along any of the three axes divided by the product of the actuation voltage along that axis and the footprint was calculated as shown in Table 5.3 for a better comparison of the positioners. Our proposed positioner has a FOM greater than 1 in each of the three axes, whereas the majority of the positioners have a much lower FOM due to larger footprint and actuation voltage.

On the other hand, the electrothermal based positioners reported in (Yong Sik Kim et al., 2012; Y. S. Kim et al., 2014) provided large displacements at reasonable voltages. However, the dissipated powers were not reported. As demonstrated, our proposed micro-positioner with capability to provide 6.7 μm, 4.5 μm and 7 μm displacements along the x-, y- and z-axes,

respectively, including the serpentine beam, compares favorably and requires low voltages to operate. It represents a good potential candidate for chip-to-chip alignment.

The integration of active optical components, such as laser sources and semiconductor optical amplifiers (SOAs), with silicon photonics is a key challenge to resolve in order to reduce the optical loss in PICs. Using FCB to integrate different chips resulted in as much as 5.1 dB of excess loss due to misalignments along the x-, y- and z- axes (Matsumoto et al., 2019). A lateral alignment tolerance of ±1 μm is required in the x-axis. However, in the direction of light propagation (i.e., y-axis), gaps as large as ~ 5 μm are kept between the waveguides of the different chips to avoid damaging their facets. This is a significant source of light loss and warrants the use of such a micro-positioner. Moreover, an out-of-plane alignment tolerance of ±0.5 μm is also required for minimizing optical losses. Thus, with the current performance of the proposed micro-positioner, a suspended optical waveguide could be integrated on top of the serpentine beam to provide fine alignment after the initial integration of the chips using FCB or another method. By having a closed loop system, control circuits could be designed to create a self-alignment procedure to maintain the optimum coupling efficiency during operation. Compared to the published works listed in Table 5.3, the proposed micro-positioner is characterized by its simple fabrication, low actuation voltage, i.e, 1 V, moderate power dissipation of less than 210 mW, relatively small area of 4 mm^2 and reasonable simulated response time of 4 ms. It also shows the ability to provide displacements within the required ranges in the x-, y- and z-axes to pave the way to address chip-to-chip misalignment in PICs.

Table 5.3 State-of-the-art of multi DOF MEMS actuators

Ref	Actuation type	Application	Footprint (mm²)	Performance (D: displacement V: actuation voltage)								
				x-axis		y-axis		z-axis		FOM[1]		
				D (µm)	V_{act} (V)	D (µm)	V_{act} (V)	D (µm)	V_{act} (V)	x-axis	y-axis	z-axis
(T. Kim & Gorman, 2022)	Electrostatic	STM[2]	~1.84	0.2	100	~ 6	100	0.4	30	0.00	0.03	0.01
(X. Liu, Kim, & Sun, 2007)	Electrostatic	Positioner	16	12.5	30	12.5	30	3.5	14.8	0.03	0.03	0.01
(Kazuhiro, Makoto, Hiroyuki, & Hiroshi, 2007)	Electrostatic	SPM[3]	10.24	19	~ 110	19	~ 110	2.12	200	0.02	0.02	0.00
(Sharma, Nabavi, Rabih, Ménard, & Nabki, 2023a)	Electrostatic/Piezoelectric	Switch	4.32	17.3	150	2.2	80	0.3	10	0.03	0.01	0.01
(Cai et al., 2017)	Piezoelectric	Positioner	> 1000	8.2	100	10.5	100	13.0	100	0.00	0.00	0.00
(Barazani, Gascon, Coia, Nabki, & Ménard, 2023)	Electrostatic/Ellectrothermal	Switch	1	4	70	12	10	-	-	0.06	1.2	-
(Cai et al., 2017; Tian et al., 2020)	Piezoelectric	Positioner	> 1000	177.33	150	179.3	150	17.45	150	0.00	0.00	0.00
(Yong Sik Kim, Dagalakis, & Gupta, 2012; Tian et al., 2020)	Electrothermal	Positioner	28	23.9	8	25.3	7	21.2	6	0.11	0.13	0.13
(Yong Sik Kim et al., 2012; Y. S. Kim, Dagalakis, & Gupta, 2014)	Electrothermal	Positioner	~ 9	53.98	7.62	49.15	8	22.91	12.01	0.79	0.68	0.21
This work	Electrothermal	Positioner	4	± 3.35	1	4.5	1	7	1	1.68	1.13	1.75

[1] Figure Of Merit   [2] Scanning Tunneling Microscope   [3] Scanning Probe Microscope

5.7 Conclusion

In this work, a novel 3-DOF electrothermal micro-positioner was demonstrated. The micro-positioner consists of a platform affixed to a serpentine beam. To generate in-plane displacements along the x- and y-axes, chevron type electrothermal actuators were designed, whereas for the out-of-plane displacement two x-axis actuators that generate opposing in-plane forces were activated, resulting in buckling of the structure. The micro-positioner was fabricated using the PiezoMUMPs microfabrication process, yielding a SOI device with a relatively compact footprint of 4 mm^2. The fabricated device provided displacements of ± 3.35 μm, 4.5 μm and 7 μm along the x-, y-, and z-axis, respectively. Hence, the micro-positioner has the potential to be used for chip-to-chip alignment between PICs.

5.1 Summary of chapter 5

In this chapter, we introduced a 3DOF positioner that leverages solely electrothermal actuators, marking a departure from the designs discussed in the preceding chapter. This new positioner is distinguished by its ability to achieve substantial displacements along all three axes while maintaining controlled cross-displacement between axes. Utilizing chevron-type electrothermal actuators enabled the design to occupy a minimal footprint. Similar to the positioners outlined previously, this electrothermal variant was fabricated using the commercial PiezoMUMPs process, featuring a 10 μm-thick SOI device layer. Although an integrated waveguide path was incorporated into the design, the fabrication process employed does not support the creation of functional optical waveguide layers. Addressing this limitation, a revised version of the electrothermal positioner, designed to be compatible with a specialized 58 μm-thick SOI technology provided by AEPONYX inc and that includes functional waveguide capabilities, was fabricated and is set to be evaluated in the subsequent chapter.

CHAPTER 6

TWO-AXIS MEMS POSITIONER FOR WAVEGUIDE ALIGNMENT IN SILICON NITRIDE PHOTONIC INTEGRATED CIRCUITS

Almur A S Rabih, Suraj Sharma, Julian Pita, Michaël Ménard, and Frederic Nabki

Department of Electrical Engineering, École de Technologie Supérieure, Montreal, Quebec H3C 1K3, Canada

6.1 Preface

This chapter presents a 2DOF version of the 3DOF electrothermal positioner described in the previous chapter. Importantly, the positioner in this chapter includes an integrated low-loss silicon nitride waveguide and is thus optically characterized in addition to the testing of its mechanical properties. Moreover, compared to previously mentioned positioners, this positioner has a thicker device layer and thus lower sensitivity to intrinsic stresses. AASR designed, simulated and tested the devices. SS helped in testing the devices. JP conducted optical simulations. MM and FN supervised the work.

6.2 Abstract

Alignment is critical for efficient integration of photonic integrated circuits (PICs), and microelectromechanical systems (MEMS) actuators have shown potential to tackle this issue. In this work, we report MEMS positioning actuators designed with the ultimate goal of aligning silicon nitride (SiN) waveguides either to different outputs within a SiN chip or to active chips, such as lasers and semiconductor optical amplifiers. For the proof-of-concept, suspended SiN waveguides implemented on a silicon-on-insulator wafer were displaced horizontally in the direction of light propagation to close an initial gap of 6.92 μm and couple the light to fixed

output waveguides located on a static section of the chip. With the gap closed, the suspended waveguides showed ~ 345 nm out-of-plane misalignment with respect to the fixed waveguides. The suspended waveguides can be displaced laterally by more than ±2 μm. When the waveguides are aligned and the gap closed, an average loss of −1.6 ± 0.06 dB was achieved, whereas when the gap is closed with a ±2 μm lateral displacement, a maximum average loss of ~ −19.00 ± 0.62 dB was obtained. The performance of this positioner does not only pave the way for active chip alignment, but it could also be considered for optical switching applications applications.

6.3   Introduction

There are significant efforts currently being made to develop photonic integrated circuits (PICs) to provide high-performance and low power optical communication systems (Kaur et al., 2021). These PICs generally integrate several optical components such as laser sources, modulators, multiplexers, and detectors (Kaur et al., 2021), into a single package. Silicon nitride (SiN) is a promising platform for developing photonic devices due several advantages (L. Wang et al., 2023). SiN-based photonics platforms enable the implementation of low loss devices, and SiN as material is compatible with standard CMOS fabrication processes (Lelit et al., 2022). In addition, SiN has a broad transparency window, low sensitivity to temperature variation and high fabrication tolerance (L. Wang et al., 2023), and can be used to create efficient non-linear devices (Smith, Francis, Navickaite, & Strain, 2023). Despite the aforementioned advantages, SiN does not possess electro-optical properties and thus SiN photonic circuits are typically tunned using power consuming thermo-optic effects. Furthermore, essential parts of PICs, i.e., active components, such as laser sources and semiconductor optical amplifiers (SOAs), cannot be realized on SiN and silicon-based platforms. Making an efficient light source from silicon is impossible since it has an indirect bandgap (Hong et al., 2021). The light amplification needed to compensate for optical losses caused by passive optical components such as couplers, interferometers, and filters is also not trivial to implement in SiN PICs. Therefore, direct bandgap III-V semiconductor materials (Z. Yao et al., 2018), such as indium phosphide (InP) and gallium arsenide (GaAs) (Yada et al.,

2018), need to be integrated with SiN and silicon-on-insulator (SOI) platforms. There are two main types of integration, hybrid and heterogeneous, which combine active components implemented on III-V platforms with passive devices fabricated on SiN and SOI platforms (Kaur et al., 2021; Ramirez et al., 2020). Hybrid integration combines two or more fully processed PICs into a single package. On the other hand, heterogeneous integration combines different materials into a single chip (Di & John, 2021). Additionally, heterogeneous integration allows for wafer-level integration of the III-V materials on silicon substrates, enabling the demonstration of efficient tunable lasers and SOAs (Ramírez et al., 2021; Yada et al., 2018).

Various techniques are used to bond different PICs. They include wafer bonding (Fang et al., 2006; Krainak et al., 2019), suited for heterogeneous integration, die-to-die bonding (J. Zhang et al., 2021), and flip-chip bonding, which is used primarily for hybrid integration (Alias et al., 2018). Although these bonding techniques make the integration of the PICs components possible, sub-micron level alignment is still a significant challenge (E.-H. Lee, Lee, O, & Park, 2004), where several fabrication dependent parameters determine the vertical and lateral alignment accuracies. For example, the vertical alignment accuracy depends on the accuracy of the etching processes, thickness tolerance of the deposited layers and bonding force. The effectiveness of lateral alignments depends on the offset angle due to rotation caused by thermal drift of the chip during bonding (Fitsios et al., 2014). One of the existing solutions to tackle the alignment issues seen in heterogeneous and hybrid integrations is to use photonic wire bonding (PWB) for directly connecting waveguides between the different processed chips or platforms, as reported in (Blaicher et al., 2020) and (Billah et al., 2018). However, although PWB is effective, its manufacturing process is complex since it requires several elaborate steps (Billah et al., 2018), and PWB has yet to reach manufacturability levels that will make it ubiquitous. Another promising solution to address the alignment challenge is Micro-Electro-Mechanical Systems (MEMS) actuators that have long been used in various sensing and telecommunications applications due to their compact size and low power consumption. MEMS actuators are used in photonic switches (Barazani et al., 2023; Briere et al., 2017; Qiao et al., 2020; Sharma et al., 2019), reconfigurable ring resonators (Qiao et al., 2021), phase

shifters (Poulton et al., 2019) and tunable optical couplers (Bishop et al., 2018; Xinmiao Liu et al., 2022; Takabayashi et al., 2021b). In (Wu & Tichem, 2018), electrothermal bimorph actuators were proposed to compensate out-of-plane misalignment between InP active chip and silicon photonic chip.

MEMS tuning approaches have been contributing to the development of programmable PICs (Xinmiao Liu et al., 2021), where waveguide meshes of tunable couplers and phase shifters could be reconfigured in software to define diverse functions and arbitrary connectivity between the input and output ports (Bogaerts & Rahim, 2020). For example, an electrostatically-actuated 1×2 optical MEMS switch with an extinction ratio of more than 23 dB over 70 nm of optical bandwidth was reported in (Takabayashi et al., 2021a). In (N. Quack et al., 2020), disk and ring resonators with MEMS-movable waveguides showed a high loaded optical quality factor of up to 3.6×10^4 and more than 20 dB of extinction ratio. In (Edinger et al., 2021; Van Iseghem et al., 2022), compact low-power comb-drive MEMS phase shifters were demonstrated where $\sim 3\pi$ phase shifts and a 3 dB bandwidth of over 1 MHz were achieved at a wavelength of 1550 nm. In (Sattari et al., 2020), a suspended MEMS-actuated directional coupler with an insertion loss of 0.5 dB and a 1 dB bandwidth of 3 nm at a wavelength of 1550 nm was implemented. In addition, optical beam steering over 5.6° has also been demonstrated with a MEMS actuator stretching a surface grating coupler (Errando-Herranz, Le Thomas, & Gylfason, 2019). A comprehensive review of MEMS-actuated gratings can be found in (Guangcan Zhou, Lim, Qi, Chau, & Zhou, 2021).

In this work, we demonstrate a MEMS positioner based on electrothermal actuators that can align suspended silicon nitride (SiN) waveguides to others located on a fixed section of the chip as a first step to show the potential of MEMS actuators to enable hybrid integration or to switch between devices in a SiN PIC. The micropositioners were implemented in a unique fabrication platform enabling monolithic integrating of SiN waveguides and silicon MEMS. It is the first fully integrated positioner capable of moving SiN along two degrees of freedom with high precision thermal actuators. The suspended waveguides were horizontally displaced to close an initial gap of 6.92 μm between the suspended and fixed waveguides. An insertion

loss of -1.6 ± 0.06 dB was achieved for the best alignment along the x and y axes, with an intrinsic average out-of-plane misalignment of 345 nm along the z axis, caused by mechanical stress.

This chapter is structured as follows: Section 6.4 presents the design and simulations of the device; Section 6.5 describes the layout and fabrication; Section 6.6 presents mechanical and optical characterization setups; Section 6.7 is dedicated to the experimental results; Section 6.8 provides a discussion of the results; and Section 6.9 presents conclusions drawn from the results and future work directions, followed by summary of the chapter in Section 6.10.

6.4 Device design and simulations

A schematic of the positioner is shown in Figure 6.1. It consists of a platform supported by electrothermal chevron-type actuators through pulling arms. These arms are supported by side springs to prevent side buckling.

The platform carries suspended waveguides routed over two dedicated optical path beams, to align them to fixed waveguides that simulate waveguides on an active chip such as a laser diode or a semiconductor optical amplifier. The lateral actuators are used to tune the light coupling into the fixed waveguides by finely displacing the platform laterally along the x-axis in both the positive or negative directions. The gap closing actuator is used to displace the platform in the direction of the positive y-axis to gradually close the gap and bring the suspended waveguides into close contact with the fixed ones to maximize coupling of the light. It is worth mentioning that when the gap is fully closed while both lateral and gap closing actuators are activated, the activation of the lateral actuator precedes in time that of the gap closing actuator to prevent damaging the contact surface of the waveguides.

To maximize the performance of the positioner, several parameters of the chevron actuators must be optimized. These parameters include the inclination angle θ, shown in Figure 6.2(a), the length, the width, the thickness and the number of chevron beams. The different parameters were optimized using a finite element analysis software (CoventorWare), where a single parameter was varied while keeping the others fixed and observing the electrical actuation power and / or displacement. The proposed positioner was fabricated using a multi-project process with a fixed device layer thickness of 59 μm, a minimum feature size of 4 μm, and a pre-defined cavity size. The fabrication process was developed by AEPONYX inc. and more details are provided in section 3. Since the displacement provided by electrothermal actuators depends on the thermal expansion of the beams, which is directly related to the size of the actuator, the size of the cavity sets the largest possible displacement because it constraints the maximum size of our actuators. Therefore, the parameters optimization was mainly focused on the inclination angle and the number of chevron beams. Figure 6.2(b) shows the effect of the inclination angle on the displacement for a single chevron beam with length, width and thickness fixed at 297 μm, 4 μm and 59 μm, respectively. It is worth noting that the length of
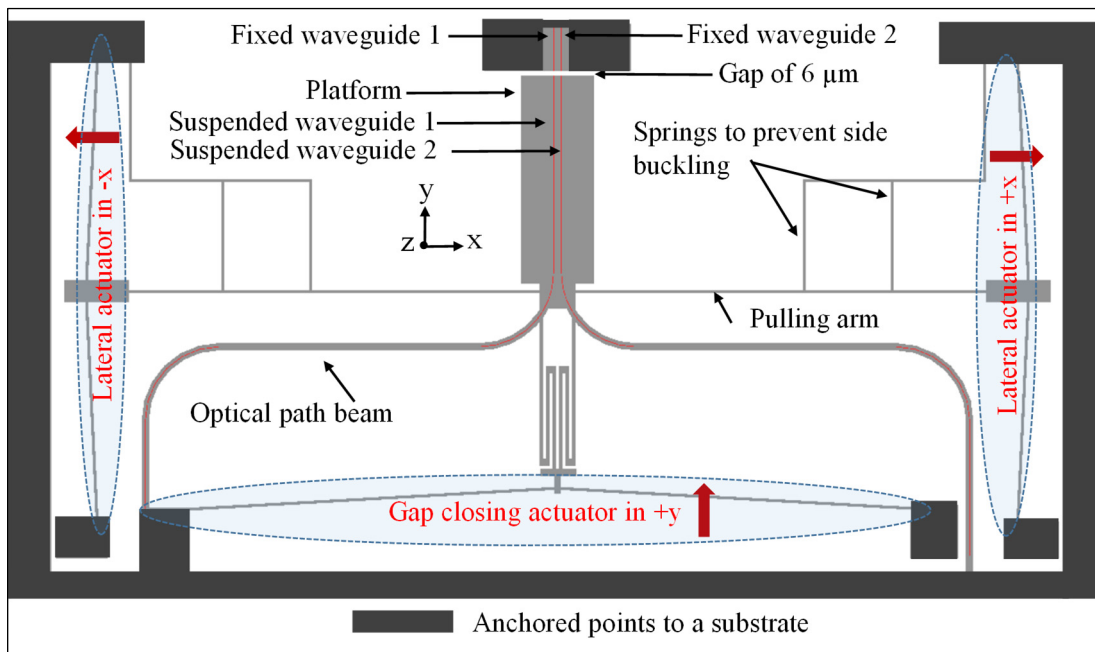
Figure 6.1 Schematic of the electrothermal MEMS waveguide positioner

the beams is determined by the pre-defined cavity size, whereas the width used was the minimum allowed by the fabrication process (displacement is reversely proportional to the width of the beam). At 5 V of actuation voltage, which corresponds to ~53 mW, the displacement was found to rapidly increase with increasing inclination angle. The displacement peaks at 2.77° then it gradually decreases beyond that angle. Thus, to determine the optimum number of chevron beams the angle was fixed at 2.77°.

Figure 6.2(c) shows the effect of chevron beams on both the displacement and the power consumption. Increasing the number of chevron beams slightly increases the displacement. However, it will linearly increase the power. As such, single chevron beams were used, as shown in Figure 6.1. Table 6.1 lists the design parameters of the positioner.
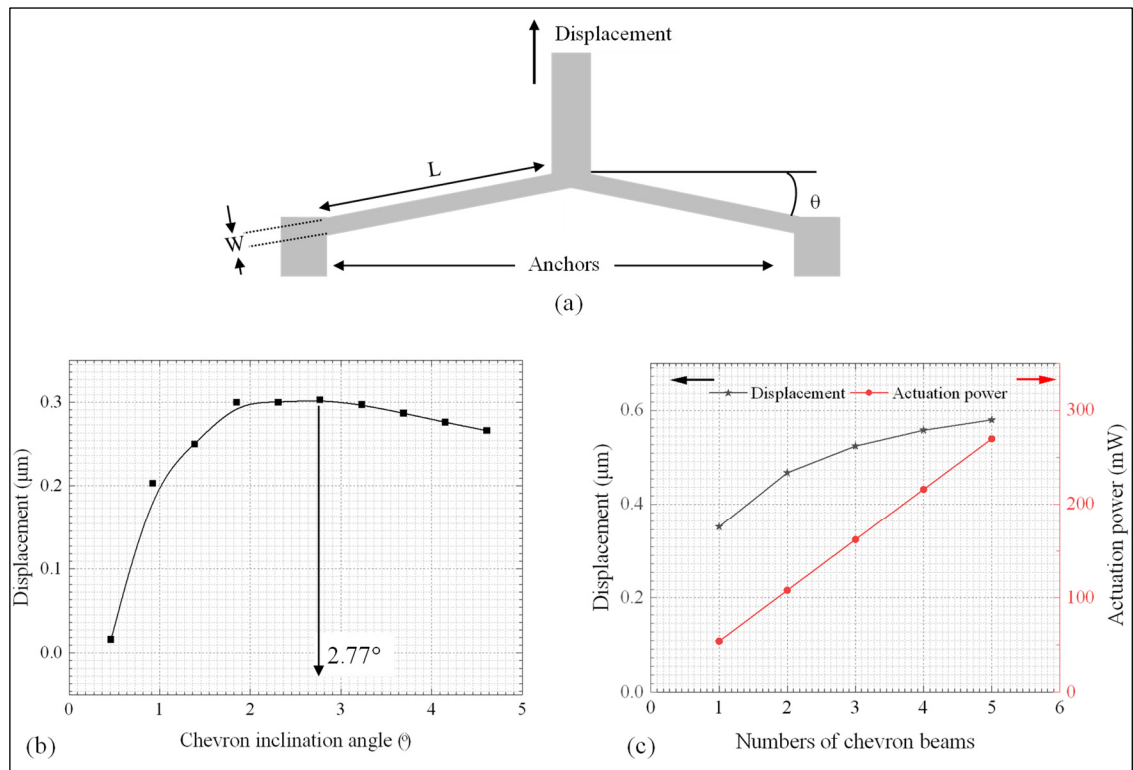
Figure 6.2 Parameters optimization of the chevron actuator: (a) schematic of a single chevron beam, (b) displacement versus inclination angle, and (c) displacement and actuation power versus the number of chevron beams

Table 6.1 Specifications of electrothermal MEMS
waveguide positioner

Parameter	Value
Average resistivity of device layer (Ω.cm)	0.0185
Gap closing actuator length (μm)	487
Lateral actuators length (μm)	297
Actuators width (μm)	4
Thickness of the device layer (μm)	59
Inclination angle (°)	2.77
Width of the optical path beam (μm)	10
Width of the pulling arms (μm)	4
Gap between fixed and movable waveguides (μm)	6
Number of movable waveguides	2

To investigate the thermal cross-talk between the gap closing and lateral actuators, electrothermomechanical simulations was conducted, where a single actuator is activated while the rest are off, and the displacement was monitored in all the three directions, i.e., along the x, y, and z-axes. Figure 6.3 (a) shows the displacements along the x and z-axes due to thermal cross-talk when the gap closing actuator in y-axis was activated. As can be seen, when the maximum actuation power of ~ 234 mW was provided to the gap closing actuator, a
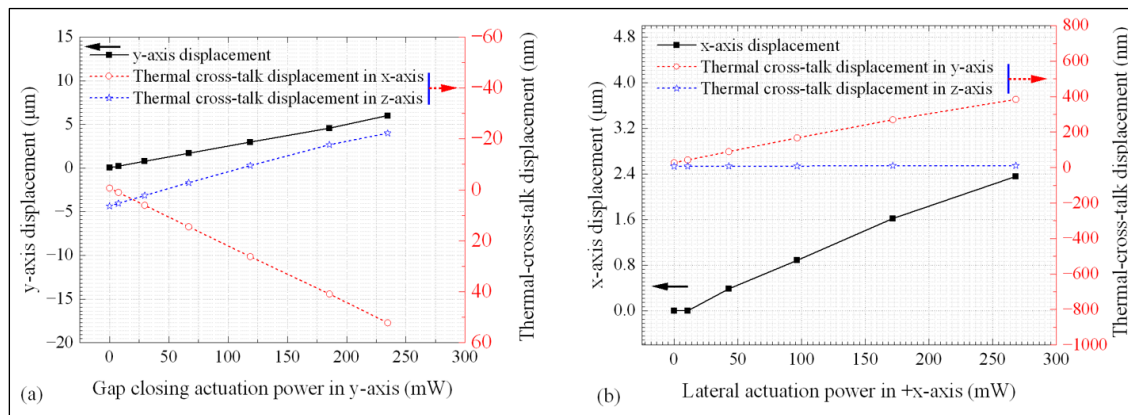
Figure 6.3 Simulated thermal cross-talk between the actuators: (a) displacements along the x and z-axes due to actuation along the y-axis, and (b) displacements along the y and z-axes due to lateral actuation along the x-axis
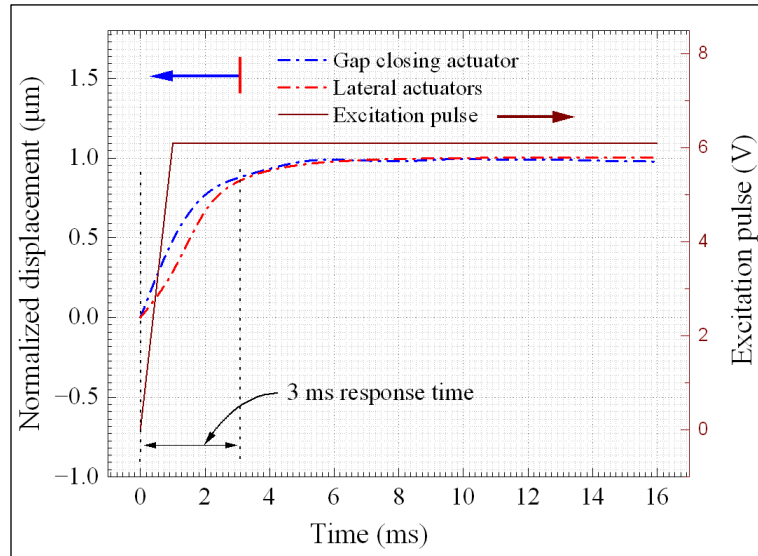
Figure 6.4 Simulated response time for gap closing and
lateral actuators

displacement of over 6 μm was obtained along the y-axis, whereas the maximum thermal cross-talk displacements along the x and z-axes were found to be only 52 nm and -22 nm, respectively. Likewise, applying 268 mW to the lateral actuators along the x-axis displaced the platform by 2.4 μm with only 9 nm of thermal-cross talk displacement along the z-axis, as shown in Figure 6.3(b). On the other hand, ~ 400 nm of displacement in +y axis direction was recorded (see Figure 6.3(b)). However, since this is the direction to close the gap, the lateral actuators can contribute to reduce the power required by the y-axis gap closing actuator.

The response time for the actuators was investigated by conducting FEA simulations, where a 15 ms-pulse of 6.1 V amplitude was applied as shown in Figure 6.4. The time for both the gap closing and lateral actuators to reach 90% of the maximum displacement amplitude was found to be 3 ms as in the figure.

6.5   Device layout and fabrication

The layout of the device, shown in Figure 6.5, was fabricated following a customized process developed by AEPONYX inc. (Sharma et al., 2022). The process uses a silicon-on-insulator wafer with a 59 μm thick silicon device layer. The wafer handle has predefined cavities to ease the release of the MEMS actuators of the positioner. Single-mode waveguides made of a stack of silicon dioxide-silicon nitride-silicon dioxide layers were used. The silicon dioxide (SiO_2) cladding layers are 3.4 μm-thick each and 10 μm-wide, whereas the core is made of a 435 nm-thick and 850 nm-wide silicon nitride (SiN) layer. The core is tapered down to 400 nm near the gap over a length of 100 μm.

The layout contains a reference waveguide (Figure 6.5(a)) that has a total length equivalent to that of the waveguides in the device to de-embed the optical propagation loss of the waveguides and find the insertion loss due only to the gap between the fixed and suspended waveguides. The waveguides have surface gratings at their end (Figure 6.5(b)) to vertically couple the light between the input/output and a fiber array. A cross-section of the device (identified by the line
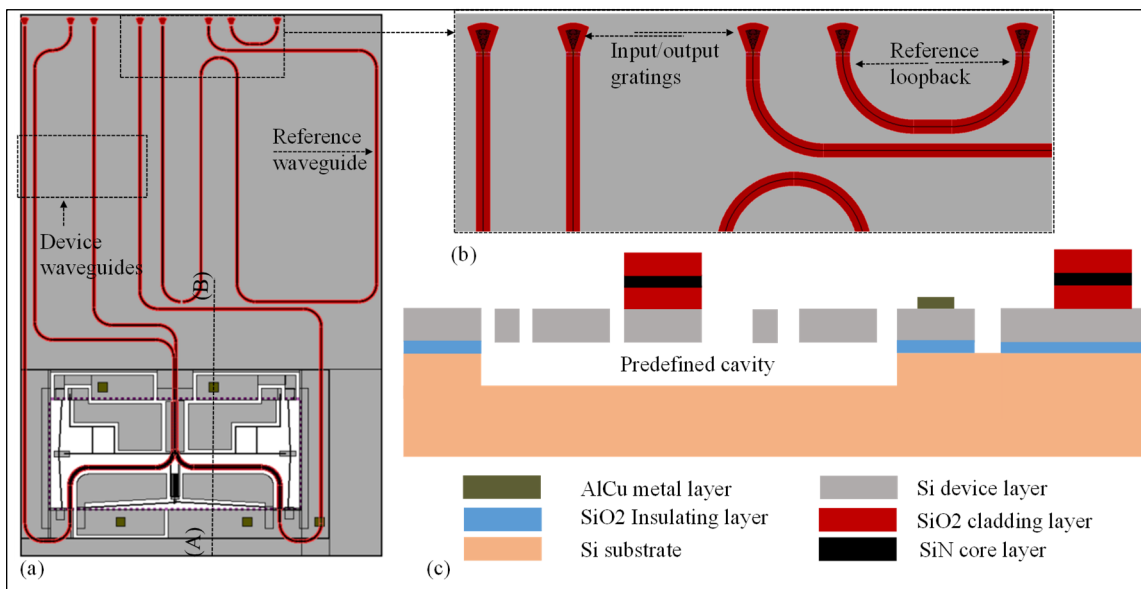
Figure 6.5 Layout of the MEMS waveguide positioner showing (a) the routing waveguides, (b) input/output gratings for vertical coupling of the light signals, and (c) the cross section corresponding to the A—B line in (a)

A—B) is shown in Figure 6.5(c). To make the connecting pads, a 250 nm-thick aluminum copper (AlCu) alloy was deposited and patterned on the terminals of the actuators. After fabricating the devices, scanning electron microscope (SEM) pictures were taken to investigate fabrication variations by comparing the measured parameters to their designed values, as shown in Figure 6.6. Variations from the designed dimensions were observed. For instance, in Figure 6.6(b), the gap was measured to be 5.86 ± 0.11 μm at the top of the silicon device layer compared to the designed value of 6 μm. It is worth noting that due to the etching sidewall slope, we could measure a larger gap of 6.87 ± 0.07 μm at the top of the waveguide. In Figure 6.6(c), the width of the optical path beam was measured to be 9.89 ± 0.20 μm compared
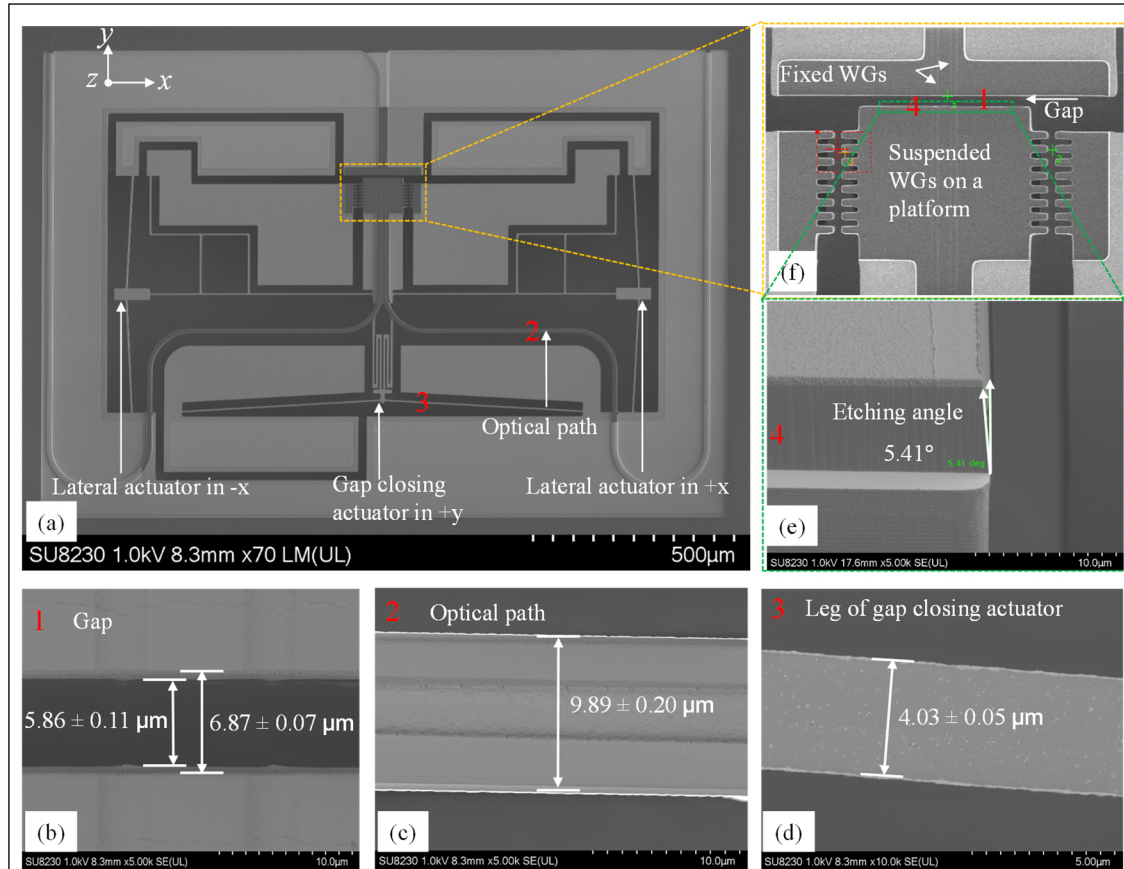
Figure 6.6 SEM images of the fabricated MEMS waveguide positioner, (a) SEM image of the MEMS actuators, (b) gap between the suspended and fixed waveguides, (c) width of an optical path beam, (d) width of the gap closing actuator along the y-axis, (e) sidewall angle of the optical stack, and (f) platform with the suspended waveguides (WGs) along with the fixed waveguides

to its designed value of 10 μm, and in Figure 6.6(d), the fabricated width of the gap closing actuator, which had a design value of 4 μm, was found to be 4.03 ± 0.05 μm. Figure 6.6(e) shows an optical stack sidewall angle of 5.41°, with an average value for the three devices found to be 5.15 ± 0.45°. This angle prevents the total closure of the gap and leaves a space of 0.59~0.6 μm between the core of the waveguides, as will be discussed in the results section of the mechanical characterization.

6.6   Characterization procedures

To characterize the fabricated devices, two type of tests, namely electromechanical and optical, were conducted. The devices were wire-bonded on specially designed printed circuit boards (PCB), and connection wires were soldered to the PCB pads to provide terminals for external power sources and measurement equipments. In general, measurements were repeated five times and the average values with their standard error deviations are reported.

6.6.1   Electromechanical characterization

Electromechanical tests were conducted to characterize the gap closing and lateral actuators by finding their displacements as a function of actuation power. A schematic of the setup used for these tests is shown in Figure 6.7(a). Before activating the actuators, the initial gaps around the platform (i.e., the separation between the movable and fixed waveguides and the gaps on the sides of the platform as shown in Figure 6.6(f)) were measured. Then, the actuators were activated, and the gaps were re-measured at each actuation voltage to find the displacement of the platform. Voltages in the range of 0 –16 V were applied using a DC voltage source (Keithley 2260B-800l, Cleveland, Ohio, USA), initially in increments of 2 V and then 1 V as the gap was nearing closure. Currents were measured using a digital multi-meter (Tektronix DMM 4050, Beaverton, Oregon, USA) and the corresponding power consumptions were calculated. A LEXT 3D confocal microscope (model OLS 4100) was used to capture and process the images to measure the gaps and the displacement of the platform.

6.6.2 Optical characterization

The optical tests were conducted using the setup shown in Figure 6.7(b). The MEMS dies were mounted on XYZ micro positioning stages (PS) to align the grating couplers with an optical fiber array polished at 30° with the help of top and side view cameras. A tunable laser source (TLS) model (T100S-HP), and an optical component tester (CT440) from EXFO were used to optically address the structures. With the TLS, an optical signal with polarization aligned along the transverse magnetic direction was swept across a wavelength range from 1500 to 1630 nm and coupled through a polarization maintaining fiber array to one of the fixed waveguides of the positioner. The light thus passed through the gap and was collected from the suspended waveguide through an output grating coupler. Output signals were read by the optical detectors (OD) and saved for analysis. The distance between the device under test (DUT) and the optical fiber array was estimated to be between 10 to 20 µm. The devices were tested in different states, including deactivating all actuators or only some of them, as summarized in Table 6.2.

After measuring the optical signal while all the actuators are inactive and the gaps are fully open, the gap closing actuator was activated by applying voltages following the procedure outlined above. The optical signal was monitored to determine the transmitted power as a
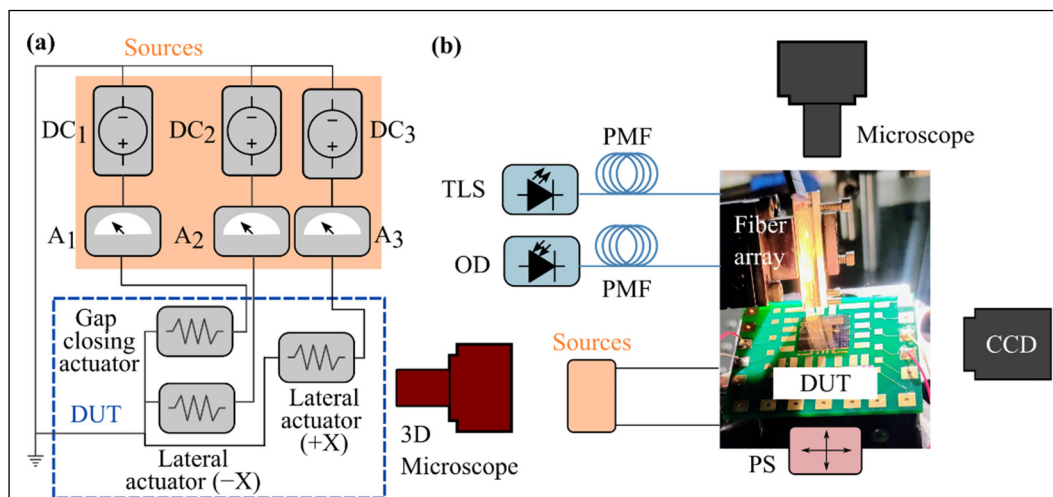
Figure 6.7 Schematic of the (a) mechanical and (b) optical testing setups used to characterize the MEMS devices under test (DUT).

Table 6.2 Conditions under which the DUTs were tested

Testing condition	Description
Gap Open (GO)	Initial state of the device where the gap is open and both gap closing and lateral actuators are inactive.
Gap Closed (GC)	State where the gap is fully closed by activating the gap closing actuator while the lateral actuators are inactive.
GC + Lateral Left (LL)	State where the gap is fully closed by activating the gap closing actuator while the lateral left actuator is also activated.
GC + Lateral Right (LR)	State where the gap is fully closed by activating the gap closing actuator while the lateral right actuator is also activated.

function of the electrical actuation power and to find the conditions when the optical output signal experienced the lowest loss. Measurements were also conducted to see the effect of laterally moving the platform either to the left or to the right when the gap was either open or closed. Note that, to be concise, only the results of lateral actuation after the gap was closed are reported here. To precisely determine the coupling losses, and hence the alignment performance of the actuators, a reference loop, i.e., a fixed structure with the same length and number of bends as the waveguides on the device, was included, as can be seen in Figure 6.5(a). Each test was repeated five times to investigate the repeatability of the measurements and to determine the measurement variability.

The experimental results are compared to 3-D FDTD simulations performed with Ansys Lumerical (Canonsburg, PA, USA) to calculate the transmission efficiency for different gaps and lateral displacements, and also while considering different out-of-plane misalignments.

6.7 Results

6.7.1 Electromechanical results

A total of three devices, referred to as Device 1, Device 2, and Device 3, were characterized, and the results were compared to finite element simulation carried out using the CoventorWare 10.5 software (Coventor, A Lam Research Company, Raleigh, North Carolina,

USA). The setup shown in Figure 6.7(a) was used to characterize the devices. First, the actuators were individually characterized by activating a single actuator while others are maintained in the off-state to measure the platform displacement along a single axis, then simultaneous activation of the gap closing actuator along the y-axis with either the lateral left actuator along the –x-axis or the lateral right actuator along the +x-axis were performed to measure the platform displacement in the x and y axes.

Figure 6.8 shows the results, where in (a) the gap and out-of-plane misalignment between the suspended and fixed waveguides are given as a function of the actuating power of the gap closing actuator when the lateral actuators are inactive, whereas (b) shows the lateral displacement of the platform versus drive power of the lateral actuators in addition to the simulated out-of-plane misalignments

As shown in Figure 6.8(a), the gap size is plotted as a function of the gap closing actuator drive power. When no power is provided to the actuator, the gap (designed value of 6 μm) was measured to be 6.92 ± 0.01, 6.80 ± 0.28 and 6.92 ± 0.01 μm for Devices 1, 2 and 3, respectively. These gaps were gradually reduced to their minimum value of 0.59~0.63 μm by increasing the actuation power to 189 mW, 215 mW and 194 mW for Devices 1, 2 and 3, respectively. This corresponds to a displacement of the platform of more than 6 μm. Increasing the actuation power beyond these values was found to have no effect on the remaining gap. This remaining gap is due to sidewall angles at the gap edges as will be discussed in section 6.

The average out-of-plane misalignment of the platform (i.e., suspended waveguides) along the z-axis with respect to the fixed waveguides was given as a function of the gap closing actuation power in Figure 6.8(a). It was found that the misalignment slightly increases by closing the gap. In Device 1, it changed from an initial value of 273 ± 32 nm to 345 ± 52 nm when 189 mW was applied. For Device 2, the misalignment increased from 287 ± 45 nm to 482 ± 29 nm at 214 mW, whereas in Device 3, the misalignment increased from a starting value of 484 ± 44 nm to 521 ± 43 nm at 194 mW. On the other hand, the finite element analysis (FEA)
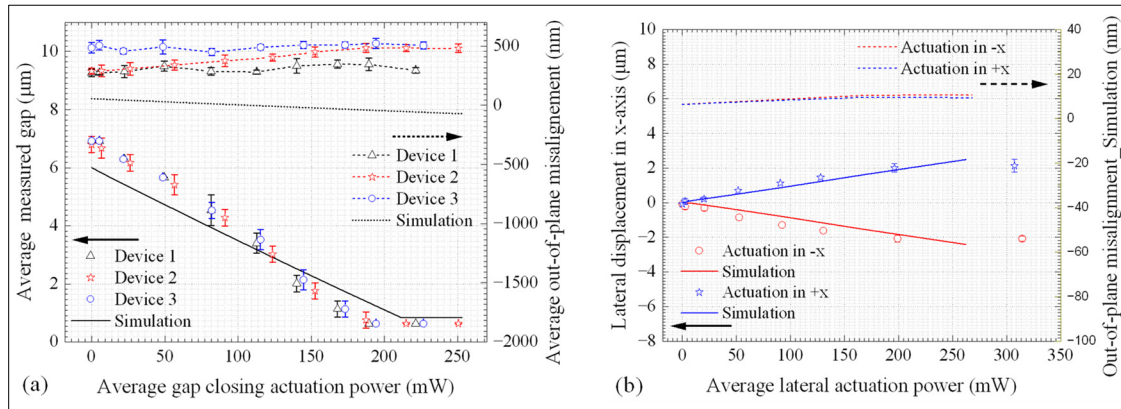
Figure 6.8 Mechanical characterizations results: (a) average gap size and average out-of-plane misalignment versus actuation power for Devices 1, 2 and 3; (b) average lateral displacement and simulated out-of-plane misalignment versus power supplied to the lateral actuators for Device 1

simulations predicted that the misalignment would decrease from +55 nm initially to −51 nm when the gap is closed, which required 211 mW.

By activating the lateral actuators, the suspended waveguides could be displaced to the left or right along the x-axis, with respect to the fixed waveguides. Figure 6.8(b) shows the average lateral displacement of Device 1 as a function of actuation power. More than ±2 μm of displacement was achieved with an actuation power of 196 mW. The results were found to be close and follow the same trends predicted by the FEA simulations. As can be seen in Figure 6.8(b), the impact of the simulated x-axis actuation on the out-of-plane misalignment is not significant.

Simultaneous activation of the gap closing and either the lateral left or lateral right actuators was also investigated since it would be required to align to different chips. Figure 6.9 shows optical images of the different actuation conditions, where Figure 6.9(a) shows the initial gap between the suspended and fixed waveguides when all three actuators are inactive. Figure 6.9(b) shows the activation of only the gap closing actuator to displace the platform along the positive y-axis to close the gap and bring the suspended waveguides into close contact with the fixed ones. Figures 6.9(c) & (d) respectively show the lateral displacement of the platform to the left

in the negative x-axis direction and to the right in the positive x-axis direction, while the gap closing actuator is activated.

6.7.2   Optical results

In this section, the optical results obtained from the test procedure described above (see Figure 6.7 (b)) are presented. The optical results were obtained for the mechanical states depicted in Figure 6.9 above; where results were recorded for the gap opened and gap closed with or without lateral displacements. The average measured results for five cycles are reported and compared to optical simulations carried out using the same gaps and out-of-plane
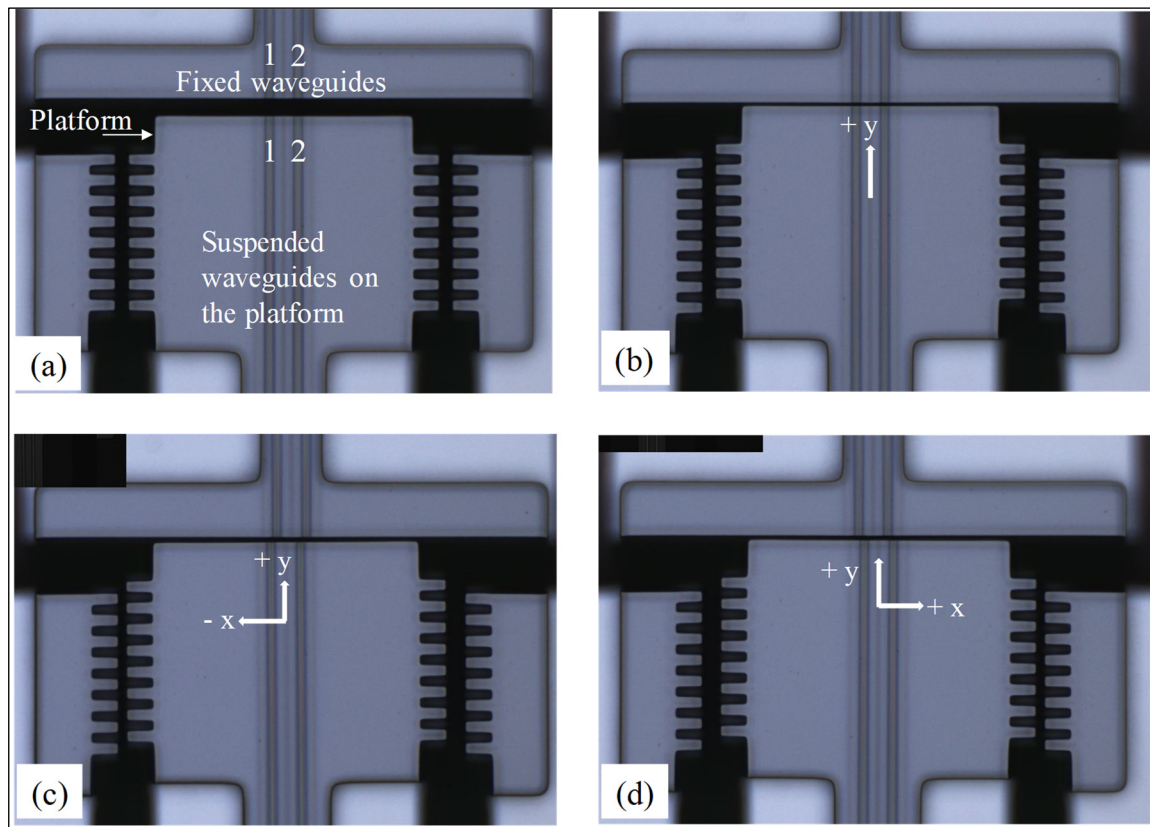
Figure 6.9 Optical image showing different actuation states of the MEMS waveguide positioners: (a) the initial state when all the actuators are inactive and the gap between the fixed and suspended waveguides is fully open (GO); (b) the gap closing actuator is activated and the gap is fully closed (GC); (c) simultaneous activation of both gap closing and lateral left actuators, where the platform was moved to the left and then the gap closed, and (d) simultaneous activation of both gap closing and lateral right actuators, where the

misalignments obtained during the mechanical characterization. Figure 6.10(a) shows the average normalized transmission over five cycles for each device over a broad wavelength range of 1555 nm to 1620 nm. The data normalization was carried out by subtracting the output signal of the device from the signal of the reference loop described in section 6.5. The data for wavelengths below 1555 nm were omitted due to high ripples associated with the grating reflections. The average normalized transmission was found when the gap is reduced to its minimum size obtained during the mechanical characterization. The average normalized transmission versus the gap size is shown by the primary y-axis of Figure 6.10(b). At the initial gap of 6.92 ± 0.01 μm, the average normalized transmissions for Devices 1, 2 and 3 were found to be -7.69 ± 0.09 dB, -7.85 ± 0.19 dB and -8.45 ± 0.04 dB, respectively versus -7.06 ± 0.10 dB for the simulation. As the gap closing actuation power increases and the gap decreases, the average normalized transmission loss decreases to -1.60 ± 0.06 dB, -1.70 ± 0.03 dB and -1.88 ± 0.02 dB for Devices 1, 2 and 3, respectively, when the gap is closed compared to -1.52 ± 0.06 dB for simulations. Note that the simulations did not consider the optical stack sidewall angle, where right angled sidewalls are used. The out-of-plane misalignment of the suspended waveguides with respect to the fixed waveguides is given by the secondary y-axis in Figure 6.10 (b). While the out-of-plane misalignment was found to slightly increase when the gap was decreased, it is clear that this misalignment has a noticeable impact on the average normalized transmission since devices with higher misalignments had higher
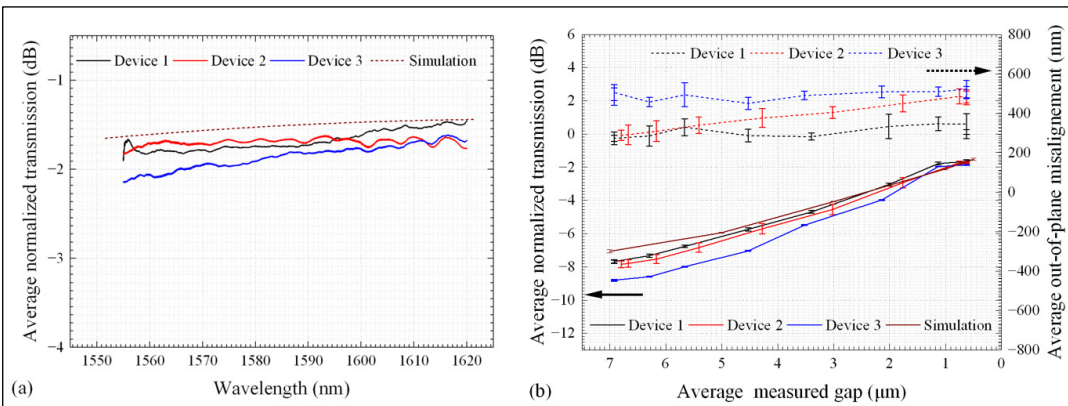
Figure 6.10 Optical characterization results showing: (a) the average normalized transmission over the wavelength range of 1555-1620 nm, and (b) the average normalized transmission and average out-of-plane misalignment versus the gap between the fixed and suspended waveguides

losses. At the minimum measured gaps of 0.63 μm, 0.67 μm and 0.59 μm for Devices 1, 2 and 3, respectively, the measured misalignments were found to be 345 ± 52 nm, 482 ± 29 nm and 521 ± 43 nm respectively. The out-of-plane misalignment used for the simulation was 400 nm.

The effect of lateral displacement on the transmission and the study of crosstalk between the two suspended waveguides were investigated for Device 1 as shown in Figure 6.11(a) and (b), respectively. To evaluate the impact of lateral displacements on the response of the device, either the lateral left or the lateral right actuator was activated with different actuation powers. For each lateral displacement value, the transmission efficiency was measured after the gap was closed. The transmission is plotted as a function of the lateral displacement in Figure 6.11(a). When the fixed waveguide (input) and suspended waveguide (output) are aligned, the average normalized transmission was -1.37 ± 0.33 dB for this device whereas the simulation predicted -1.52 ± 0.06 dB. Increasing the lateral displacement of the platform to $\sim \pm 2$ μm $(-2.08 \pm 0.17$ μm for lateral left and 2.12 ± 0.37 μm for lateral right) increases the average transmission loss to -19.0 ± 0.62 dB. The measured results were found to follow the same trend observed in the simulations for the same conditions, where for $\sim \pm 2.5$ μm, a simulated transmission loss of -20.48 ± 0.07 dB was predicted. The curve in the figure indicates that the

(a)　　Average lateral displacement (μm)　　(b)　　Wavelength (nm)
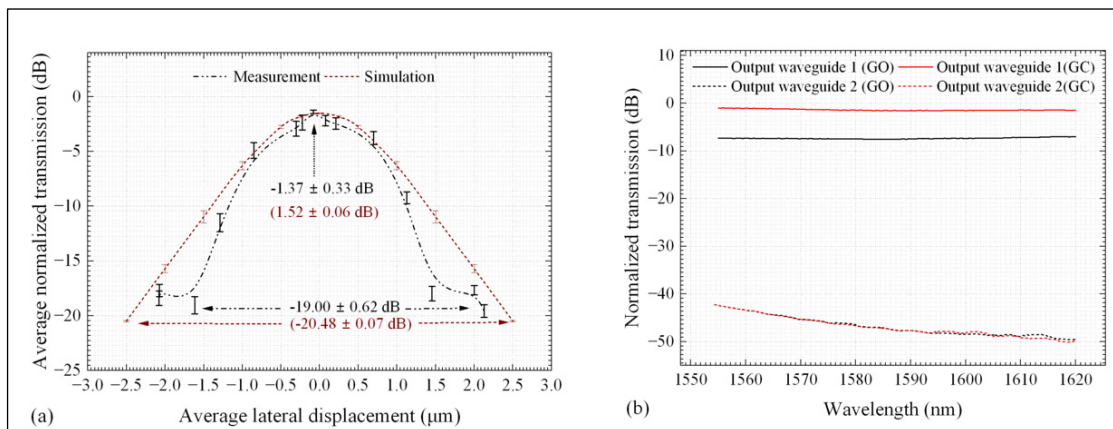
Figure 6.11 Optical characterization results of Device 1 showing: (a) the effect of lateral displacement of the platform on the average normalized transmission, and (b) the study of crosstalk between the two movable waveguides on the platform results

measured transmission saturates when displacement is close to 2 µm, contrary to simulations. This could be because we are reaching the limit of the lateral actuator, as shown in Figure 6.8(b).

To investigate the cross-talk between the movable waveguides, which are separated by 10 µm, light was coupled to the fixed waveguide 1 shown in Figure 6.9 (a) and the output was measured on both movable waveguides 1 and 2. When the gap is closed, the input waveguide 1 is aligned to the output waveguide 1 whereas the output waveguide 2 is offset by 10 µm from the input light path. The transmission was measured when the gap is open (GO) and closed (GC), as shown in Figure 6.11(b). For both the GO and GC states, output waveguide 2 shows almost no coupling of light from input waveguide 1, with less than −40 dB of crosstalk between the two movable waveguides when the gap is closed.

6.8   Discussion

The 59 µm device layer used to build the devices was previously reported to have a great resilience to residual stresses caused by waveguides, where significant improvement in out-of-plane misalignment between the fixed and suspended parts were achieved over structures with a 10 µm device layer (Sharma et al., 2022). For the three tested devices (Devices 1, 2 and 3), out-of-plane misalignments of 345 ± 52 nm, 482 ± 29 nm and 521 ± 43 nm were measured, respectively when the gap was closed. The corresponding average normalized optical transmission were -1.60 ± 0.06 dB, -1.70 ± 0.03 dB and -1.86 ± 0.02 dB, respectively. This result indicates a correlation between the out-of-plane misalignment and the coupling efficiency. This is also confirmed by simulations, as shown in Figure 6.12, obtained with the same residual measured closed gap size of 0.63 µm with no lateral misalignments. Simulations were carried out using the three-dimensional finite-difference time-domain (3-D FDTD) method for vertically aligned waveguides and with vertical out-of-plane misalignments of 200 nm, 400 nm, and 600 nm. Figures 6.12(a) & (b) show the electric field propagation for vertically aligned and 600 nm of vertical (i.e., out-of-plane) misalignment, respectively. As expected, simulations of the gaps with minor vertical misalignment between the fixed and suspended waveguides show less scattering. The simulated average transmission over the

wavelength range of 1550 to 1620 nm compared to that of the tested devices is shown in Figure 6.12(c). The simulated loss increases from −0.66 dB for the vertically aligned waveguides to −2.56 dB for 600 nm vertical misalignment. This is in good agreement with the experimental data, where the devices with low out-of-plane misalignment, such as Device 1, have shown better performance (−1.60 ± 0.06 dB) compared to that with higher misalignment, such as Device 3 (−1.86 ± 0.02 dB).

The effect of out-of-plane misalignments on optical losses was also reported by other authors. For instance, in (Chang et al., 2022), losses of −0.8 dB/μm of out-of-plane misalignment were mentioned when a silicon nitride waveguide of a tapered width of 120 nm and cladding of 8 μm was coupled to a fiber. This loss is smaller than that measured by our devices where 600 nm misalignment increases the loss by −1.9 dB. This significant difference could be due to the difference in design geometries (such as tapered waveguide width; 120 nm vs 400 nm in our case). In another study, simulation results on a silicon nitride waveguide with a 500×500 nm^2 cross-section aligned to a InP active chip showed −1.78 dB of coupling loss for 200 nm of out-of-plane misalignment and 300 nm of lateral misalignment (Chatzitheocharis, Ketzaki, Calò, Caillaud, & Vyrsokinos, 2020), compared to 0.9 dB for the case with ideal alignment. A second simulated result (Y. Zhang et al., 2021) obtained for the hybrid integration of a laser diode and
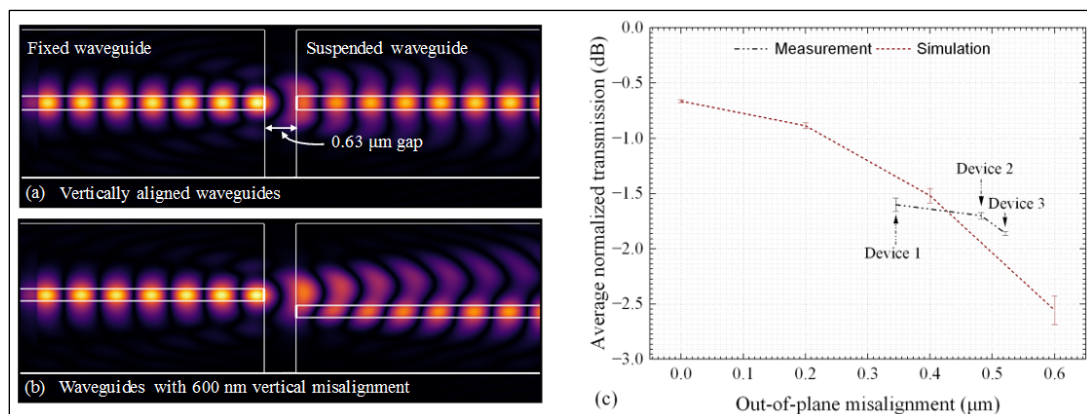
Figure 6.12 Effect of out-of-plane misalignment on the propagation of light from the fixed waveguide to the suspended one: simulated electric field propagation for (a) vertically aligned waveguides, (b) 0.6 μm out-of-plane misalignment, and (c) the effect of the out-of-plane misalignment on the transmission

a silicon photonic waveguide with the help of spot size converters, a 1 dB loss tolerance was reported for misalignments of ±1.69 μm in the lateral direction, of ±0.49 μm in the out-of-plane direction and of 3.8 μm in the direction of light propagation. These results support our findings about the impact of out-of-plane misalignment on the insertion loss.

The performance of the positioners could be improved by the use of spot size converters and coatings to minimize the optical modes mismatch and to reduce reflections and interferences (Marchetti, Lacava, Carroll, Gradkowski, & Minzioni, 2019). Furthermore, it was also reported that the sidewall angles limits the minimum achievable gap size (Brenes, Vysotskyi, Lefeuvre, & Juillard, 2019), and hence the minimal optical loss obtainable. For example in (Sharma et al., 2022), a residual air gap of 1 μm was reported for sidewall angles of 7.86° and 8.97°, and improving the etching process to improve the sidewall angle was found to reduce the minimal gaps achievable, and enhance the optical losses. Likewise, our SEM results showed that the two sidewalls of the gap that separate the input and output waveguides are not etched vertically. Angles of 5.26 ± 0.04°, 5.60 ± 0.07° and 4.91 ± 0.01° were measured for the sidewalls of Devices 1, 2 and 3, respectively. Because of these angles, measuring the initial gap reveals two distinct topographies, as shown in Figure 6.6(b). The first measurement shows a gap of 5.86 ± 0.11 μm at the level of the silicon layer, which is close to the designed value of 6 μm. However, the other measurement shows a gap in the range of 6.87 ± 0.07 μm, which is the one at the top of the optical stack.

The measured etching angles lead to a residual gap at the level of the core of the waveguide of 0.63 μm, 0.67 μm and 0.59 μm for Device 1, 2 and 3, respectively, as depicted in Figure 6.13. These measured residual gaps contribute to the minimal insertion losses obtained. Device 3, which has the lowest residual gap of 0.59 μm, is expected to show a lower loss compared to Devices 1 and 2. However, due to higher out-of-plane misalignment, Device 3 shows the highest loss nonetheless, in line with the previously discussed simulation results. A better loss profile thus requires right angled sidewalls along with precise vertical waveguide alignment.

The micropositioner demonstrated a flat transmission over the entire 1555-1620 nm wavelength range. For wavelengths below 1555 nm, the transmission was limited by the bandwidth of the surface grating coupler. The maximum wavelength was limited by our tunable laser. With over 70 nm of experimental optical transmission bandwidth, we consider that our device is broadband. Furthermore, since the waveguides are made of silicon nitride and silicon dioxide and that the geometry of the waveguides (i.e., the dimensions of the core and the thickness of the cladding) can be modified without changing the actuators, our design could be readily adapted to operate anywhere from the visible to the mid-infrared. The lower limit is set by the transparency of silicon nitride while the upper one is defined by the absorption of the silicon dioxide cladding. With the geometry used in the prototypes, the waveguide is single mode for wavelengths larger than 1425 nm. Therefore, with proper gratings or if light was launched onto the chip through edge coupling, the devices presented in this manuscript could operate from 1425 nm until approximately 2000 nm, where losses due to absorption by the cladding would become significant.
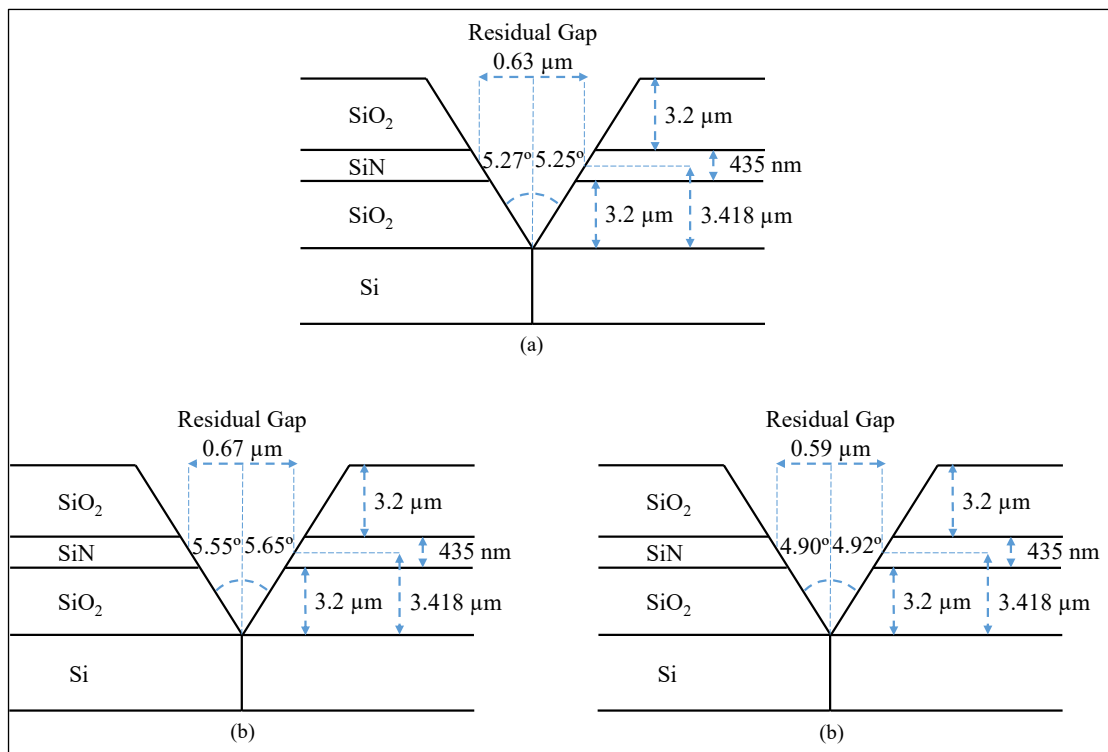
Figure 6.13 Residual gap sizes due to the measured sidewall angles for (a) Device 1 (b) Device 2 and (c) Device 3

Despite the high thermal stability of the SiN used to build the waveguides, electrothermal actuators generate heat, and temperature is expected to impact the waveguides characteristics, such as their effective refractive index. Nevertheless, since the micropositioner consists of a simple waveguide, variations in temperature will not affect its optical response.

Table 6.3 summarizes works involving active chips, such as laser diodes and semiconductor optical amplifiers (SOAs) that are integrated with silicon photonics. The comparison is focused on the resulting misalignment in the lateral direction (x), in the light propagation direction (y) and in the out-of-plane direction (z), in addition to the minimum insertion loss achieved. The table shows that photonic wire bonding (PWB) is a promising technology to avoid misalignment related issues, where in (Billah et al., 2018; Blaicher et al., 2020), optical insertion losses were reduced to sub 1-dB levels. Nonetheless, the production in volumes of this process

Table 6.3 Comparison of state-of-art works using different integration techniques for active chip integration with silicon and silicon nitride photonics

Reference	Technology used	Misalignment (µm)			Insertion loss (dB)
		x	y	z	
(Theurer et al., 2020)	Flip-chip bonding of InP laser on SiN TriPleX chip.	6	4.2	5.1	-2.1 ± 0.35
(Y. Yang, Zhao, Ren, & Huang, 2021)	Monolithic integration of DFB laser grown on the same Si PIC.	± 1	N/A	N/A	-3.7 ± 0.1
(Blaicher et al., 2020)	Using photonic wire bonding (PWB) for InP laser to SiPh chip.	N/A	N/A	N/A	-0.7 ± 0.15
(Billah et al., 2018)	Using photonic wire bonding (PWB) for InP laser to SiPh chip.	N/A	N/A	N/A	-0.4 ± 0.3
(Hatori et al., 2014)	Flip-chip bonding of InP light source fabricated on a Si platform.	± 1	N/A	N/A	~ -3.3
(Matsumoto et al., 2019)	Flip-chip bonding of SOAs on Si photonic platform	5	± 1	± 0.5	-5.1
This work	MEMS actuators to align suspended to fixed SiN WGs	0.63	0	0.35	-1.60 ± 0.06

still requires further optimization (Lindenmann, 2018), and its accessibility is still limited. Moreover, this technique does not provide post-assembly modification of the alignment profile or configuration. Monolithic integration shown in (Y. Yang et al., 2021) resolves the misalignment issues due to the local growth of laser sources on silicon platforms. However, monolithic integration requires a tradeoff in material properties to cater for both III-V devices and silicon passive devices (Franck Chollet, 2016). In addition, III-V devices grown on silicon will have a shorter lifetime due to defects caused by lattice mismatch between the grown III-V devices and the silicon substrates (Miller, 1998). Thus, typically for best performance, III-V devices are fabricated separately and then integrated onto the silicon substrate using flip-chip bonding, as demonstrated in (Theurer et al., 2020), (Hatori et al., 2014) and (Matsumoto et al., 2019). Our proposed MEMS devices that demonstrate silicon waveguide-waveguide misalignments of 0 μm, 0.63 μm and 0.345 μm in x, y and z directions, respectively, and an insertion loss of -1.60 ± 0.06 dB, represent a promising solution for a feasible alignment system that could be performed not only during the chips integration, but also throughout its operation, allowing for readjustments or reconfiguration. Nevertheless, the current demonstration was performed with waveguides on the same chip, which avoids the challenges related to positioning the active chip. Creating a cavity to integrate the active chip on the SiN PIC will be the next step.

With regard to MEMS positioners for chip-to-chip alignment, the research field remains limited. Only a few studies were reported about active components alignment. For instance, in (Wu et al., 2016), MEMS electrothermal actuators were used to actuate flexible suspended waveguides to align an InP active chip with a silicon chip on a common carrier. The silicon chip was comprised of a 16 μm-thick stack of materials of the TriPleX platform (silicon dioxide-silicon nitride- silicon dioxide on a silicon substrate). A pick-and-place machine was used to make the initial coarse alignment, whereas the MEMS actuators were activated to fine tune the alignment. A maximum vertical deflection of 18.5 μm at a consumed power of 130 mW (12 V) was achieved. In another study (Q. X. Zhang et al., 2010), two-axis in-plane electrothermal actuators were used to align a discrete laser diode, flip-chip-bonded to a fiber placed inside a v-groove on a silicon substrate. A displacement of 50 μm was achieved at a voltage of 25 V with a

positioning resolution of 0.1 μm. With the great success of MEMS devices in several PICs components, including tunable couplers (M. W. Pruessner et al., 2022), resonators (Ikeda & Hane, 2013a), optical switches (Sharma et al., 2022) and movable mirrors (Sadhukhan & Prasad Singh, 2022), MEMS actuators in combination with low loss silicon based waveguides, are expected to pave a way for a dynamic and low cost alignment method.

6.9   Conclusions

This work reported MEMS waveguide positioners proposed for alignment of active chips with passive silicon nitride photonic chips. The proof of concept was tested by aligning suspended and fixed silicon nitride waveguides on the same SOI substrate. The waveguides were composed of a stack of oxide-nitride-oxide deposited on top of a 59 μm device layer. Three devices were mechanically and optically tested, and the results were compared to FEA and 3-D FDTD simulations carried out with CoventorWare and Lumerical, respectively. Results showed that with 189 mW of actuation power, an initial gap of 6.92 μm between the suspended and fixed waveguides could be closed to 0.63 μm with an out-of-plane misalignment of 345 nm. When the gap is closed, an average insertion loss of -1.60 ± 0.06 dB was measured in the wavelength range between 1550 to 1620 nm. With 196 mW of actuation power, the suspended waveguides were laterally misaligned by ± 2 μm, and when the gap is closed they provide an attenuation of up to 20 dB. Thus, the positioner can operate as an attenuator or an on/off switch. The positioner has two suspended output waveguides separated by 10 μm, and less than -40 dB of crosstalk was observed between the waveguides. With the great performance achieved, the next step will be to incorporate an out-of-plane actuator to compensate the out-of-plane misalignment, to realize the actual application of chip-to-chip alignment.

6.10   Summary of chapter 6

In this chapter, an electrothermal-based 2DOF positioner incorporating a functional waveguide was developed and tested, evolving from the 3DOF positioner presented in the previous chapter. The adoption of a thicker SOI device layer, measuring 58 μm, posed significant challenges in

integrating an out-of-plane actuator for vertical displacement. Despite these hurdles, the positioner, fabricated with this larger device layer thickness, exhibited substantially lower residual stress compared to the 3DOF design that utilized a 10 μm-thick SOI layer. This reduction in residual stress resulted in diminished optical losses when the positioner's integrated suspended waveguide was compared against a stationary waveguide fabricated on the same silicon substrate. This comparative analysis served as an initial characterization step for the actuators, moving closer to the ultimate goal of achieving effective active chip alignment within PICs.

CONCLUSIONS AND FUTURE WORKS

Conclusions

This thesis presented several MEMS devices proposed as waveguide positioners in photonic integrated circuits for active chips alignment. It culminated in the demonstration of an optical waveguide positioner device that was optically characterized in addition to the testing of its mechanical operation.

First, in chapter 3, an aluminum nitride out-of-plane piezoelectric MEMS actuator was presented. Testing this device over a range of ±60 V provided upward and downward displacements with a total average displacement of 1.30 ± 0.04 µm for five runs. Capacitance measurement showed a linear relation with the displacement, where at −60 V the average change in capacitance was found to be -13.10 ± 0.89 fF, whereas at 60 V the change was 11.09 ± 0.73 fF. This study also investigated the effect of the residual stress caused by the top metal electrode on the linearity of the displacement-voltage relation. Simulation predicted that the prototype could be modified to accommodate waveguide routing without affecting the performance, in addition to the feasibility of incorporating in-plane lateral actuators.

Second, chapter 4 presented two novel Multi-Degrees of Freedom (MDOF) devices equipped with a capacitive sensing mechanism for tracking displacements, and a waveguide path to route an optical signal. Hybrid actuation mechanisms with aluminum nitride out-of-plane piezoelectric actuators and in-plane electrostatic actuators were implemented. The first device had 2DOF motions, where in the z-axis, at −60 V, downward displacement of -1.46 ± 0.34 µm was measured, with an average capacitance change of -15.37 ± 0.19 fF, whereas at 60 V, an upward displacement of 1.70 ± 0.14 µm was measured, with and average capacitance change of 10.72 ± 0.46 fF. For the in-plane motion in the y-axis, at 100 V, a 2.39 ± 0.34 µm displacement was measured, with an average capacitance change of -7.77 ± 0.32 fF. The second device had 3DOF, where in the z-axis at the same mentioned voltages, the measured downward and upward displacements were found to be of -0.17 ± 0.03 µm and 0.46 ± 0.04 µm,

respectively, with corresponding capacitance changes of −18.53 ± 0.16 fF and 13.06 ± 1.16 fF, respectively. For the in-plane displacement in the y-axis, at 100 V, a 5.16 ± 0.28 μm displacement was measured, with an average capacitance change of -20.09 ± 1.56 fF. This device also had lateral motion in the x-axis, where a 319 ± 33 nm total displacement was achieved at 100 V. Thanks to this hybrid combination, in-plane and out-of-plane misalignments were compensated by activating more than one actuator at a time, and the results were found to be close to that obtained by FEA simulations.

In chapter 5, an electrothermal-based 3DOF MEMS positioner device equipped with a waveguide path was presented. At 105 mW power, the device provided ±3.35 μm displacements in the x-axis to cover a total travel range of 6.7 μm. The y-axis actuator was found to provide a 4.5 μm displacement at a 140 mW actuation power, whereas 7 μm out-of-plane displacement in the z-axis at 210 mW was generated through beam buckling, by applying two opposite in-plane electrothermal forces on the x-axis actuators.

Finally, chapter 6 demonstrated a proof of concept of 2DOF electrothermal positioner device for active chip alignment. The fabricated prototype included an integrated suspended silicon nitride waveguide separated from a fixed waveguide by a measured initial gap of 6.92 ± 0.01 μm. This device was thus optically characterized, in addition to the testing of its displacement. Applying 189 mW to the y-axis actuator reduced the gap to a fixed residual remaining gap of only 0.63 μm, limited by the etching angle of 5.26 ± 0.04° at the edge of the material stack forming the optical waveguides. The measured out-of-plane misalignment at the gap closed was of 345 ± 52 nm. When the gap was closed, the average minimum measured optical insertion loss in the wavelength range of 1550 to 1620 nm was found to be -1.60 ± 0.06 dB. By applying around 196 mW to the lateral actuators in the x-axis, ± 2 μm of displacement was achieved, and simultaneous activation of the gap actuator and lateral actuators could provide an attenuation of up to 20 dB. Thus, the device could operate as an attenuator or an on/off switch. The device had two suspended output waveguides separated by 10 μm, and less than -40 dB of crosstalk between the waveguides was observed.

The measured mechanical results for all the reported devices were found to be in good accordance with the FEA simulation results obtained by CoventorWare. In addition, the measured optical results of the device presented in chapter 6 agreed well with the 3-D FDTD simulations carried out with Lumerical.

As a whole, this PhD thesis aimed to address the misalignment issues faced by the current photonic integration techniques, in which stringent alignment tools are used to align active chips such as laser sources and semiconductor optical amplifiers to silicon-based devices, on a common platform. Beside the critical alignment required to make the bonding, any post bonding misalignments can result in optical losses but no solution is readily available. Accordingly, the thesis proposed several MEMS positioners with the aim of moving suspended waveguides, and presented an optical aligned device which was optically characterized. This approach represents a path to eliminating the aforementioned issues by providing a dynamic and flexible alignment system. Firstly, using suspended waveguides that are free to move in the x-, y- and z- axes reduces the need for the stringent alignment tolerances required by the current bonding techniques. Secondly, any post bonding misalignments are compensated by displacing the suspended waveguide in the respective misalignment axis. Experiments showed that simultaneous activation of several actuators is possible. Thirdly, as the positioners are equipped with displacement sensing mechanisms, feedback control circuits could be integrated on the alignment system to provide self-alignment. Finally, these batch fabricated MEMS devices can lead to reduction of cost and alignment time.

Future work

The promising experimental results obtained shed the light on the possibility to have further improvements for better device performance. Future work could touch on many topics, and some topics will be discussed next:

- For the positioners presented in chapters 3 & 4 that use a displacement sensing mechanism, moving the capacitive sensing combs closer to the waveguide-carrying platforms is recommended. For the current designs, there are long beams (~ 1mm) between the combs and platforms, and due to the residual stress, the measured capacitance is not a direct function of the platform displacement.

- For the piezoelectric actuators of the positioners presented in chapters 3 & 4, due to the thickness difference between the bottom (10 μm-thick silicon) and top electrodes (1 μm-thick aluminum) and the residual stress, the downward and upward displacements were found to be different for the same actuation voltage. Thus, equating the thicknesses of the electrodes, and reducing the sizes of the devices are expected to improve displacement mismatches.

- Devices presented in chapters 3 to 5 are made of a 10 μm-thick silicon layer, thus the residual stress on the suspended waveguides has a large impact, which resulted in as much as ~ 5 μm of initial out-of-plane deformation. Increasing the thickness of the device layer is expected to reduce the impact of the stress and the out-of-plane deformation of the suspended waveguides. This was explored in chapter 6.

- The device presented in chapter 6 uses a 59 μm-thick silicon layer, which improved the initial out-of-plane deformation to ~ 350 nm. Incorporating an out-of-plane actuator to this device will facilitate the compensation of this deformation.

- While the 59 μm thickness improved tremendously impact of the residual stress observed over that seen in positioners that have a 10 μm thickness, it became challenging to integrate the out-of-plane actuator with the 59 μm-thick positioner. Thus, the possibility of using a 20 – 30 μm device layer thickness could be investigated.

LIST OF REFERENCES

Abe, S., & Hane, K. (2013). Variable-Gap Silicon Photonic Waveguide Coupler Switch With a Nanolatch Mechanism. *IEEE Photonics Technology Letters, 25*(7), 675-677. doi:10.1109/LPT.2013.2248354

Algamili, A. S., Khir, M. H. M., Dennis, J. O., Ahmed, A. Y., Alabsi, S. S., Ba Hashwan, S. S., & Junaid, M. M. (2021). A Review of Actuation and Sensing Mechanisms in MEMS-Based Sensor Devices. *Nanoscale Research Letters, 16*(1), 16. doi:10.1186/s11671-021-03481-7

Alias, M. S., Tangi, M., Holguín-Lerma, J. A., Stegenburgs, E., Alatawi, A. A., Ashry, I., . . . Ooi, B. S. (2018). Review of nanophotonics approaches using nanostructures and nanofabrication for III-nitrides ultraviolet-photonic devices. *Journal of Nanophotonics, 12*(4), 043508. Retrieved from https://doi.org/10.1117/1.JNP.12.043508

Alneamy, A., Al-Ghamdi, M., Park, S., Khater, M., Abdel-Rahman, E., & Heppler, G. (2019). Dimpled electrostatic MEMS actuators. *Journal of Applied Physics, 125*(2), 024304. doi:10.1063/1.5053597

Amin, T. M. F., Huda, M. Q., Tulip, J., & Jäger, W. (2015). Design and Fabrication of a Long-Arm Comb-Drive Rotary Actuator With Externally Mounted Mirror for Optical Applications. *Journal of Microelectromechanical Systems, 24*(5), 1565-1574. doi:10.1109/JMEMS.2015.2423285

An, Z., Men, C., Xu, Z., Chu, P. K., & Lin, C. (2005). Electrical properties of AlN thin films prepared by ion beam enhanced deposition. *Surface and Coatings Technology, 196*(1), 130-134. doi:https://doi.org/10.1016/j.surfcoat.2004.08.169

Aryal, N., & Emadi, A. (2020). A Method to Enhance Stroke Level of a MEMS Micromirror with Repulsive Electrostatic Force. *Micromachines, 11*, 401. doi:10.3390/mi11040401

Ba-Tis, F., & Ben-Mrad, R. (2015). A 3-DOF MEMS Electrostatic Piston-Tube Actuator. *Journal of Microelectromechanical Systems, 24*(4), 1173-1184. doi:10.1109/JMEMS.2015.2392692

Bahgat, A. S., Zaki, A. H., Mohamed, M. A., & Sherif, A. F. E. (2018). *Design and simulation of MEMS-actuated adjustable optical wedge for laser beam scanners* (Vol. 17): SPIE.

Barazani, B., Gascon, A., Coia, C., Nabki, F., & Ménard, M. (2023). Broadband 1 x 4 Silicon Nitride Photonic Switch Fabricated on a Hybrid Electrothermal and Electrostatic MEMS Platform. *Journal of Lightwave Technology*, 1-14. doi:10.1109/JLT.2023.3292341

146

Barrett, L. K., Stark, T., Reeves, J., Lally, R., Stange, A., Pollock, C., . . . Bishop, D. J. (2019). A Large Range of Motion 3D MEMS Scanner With Five Degrees of Freedom. *Journal of Microelectromechanical Systems, 28*(1), 170-179. doi:10.1109/JMEMS.2018.2886653

Barwicz, T., Lichoulas, T. W., Taira, Y., Martin, Y., Takenobu, S., Janta-Polczynski, A., . . . Boyer, N. (2018). Automated, high-throughput photonic packaging. *Optical Fiber Technology, 44*, 24-35. doi:https://doi.org/10.1016/j.yofte.2018.02.019

Bezzaoui, H., & Voges, E. (1991). Integrated optics combined with micromechanics on silicon. *Sensors and Actuators A: Physical, 29*(3), 219-223. doi:https://doi.org/10.1016/0924-4247(91)80018-K

Bian, Y., Ramachandran, K., Wu, Z. J., Hedrick, B., Dezfulian, K. K., Houghton, T., . . . Letavic, T. (2023). 3D Integrated Laser Attach Technology on a 300-mm Monolithic CMOS Silicon Photonics Platform. *IEEE Journal of Selected Topics in Quantum Electronics, 29*(3: Photon. Elec. Co-Inte. and Adv. Trans. Print.), 1-19. doi:10.1109/JSTQE.2023.3238290

Billah, M. R., Blaicher, M., Hoose, T., Dietrich, P.-I., Marin-Palomo, P., Lindenmann, N., . . . Koos, C. (2018). Hybrid integration of silicon photonics circuits and InP lasers by photonic wire bonding. *Optica, 5*(7), 876-883. doi:10.1364/OPTICA.5.000876

Bishop, Z. K., Foster, A. P., Royall, B., Bentham, C., Clarke, E., Skolnick, M. S., & Wilson, L. R. (2018). Electro-mechanical control of an on-chip optical beam splitter containing an embedded quantum emitter. *Optics Letters, 43*(9), 2142-2145. doi:10.1364/OL.43.002142

Blaicher, M., Billah, M. R., Kemal, J., Hoose, T., Marin-Palomo, P., Hofmann, A., . . . Koos, C. (2020). Hybrid multi-chip assembly of optical communication engines by in situ 3D nano-lithography. *Light: Science & Applications, 9*(1), 71. doi:10.1038/s41377-020-0272-5

Bogaerts, W., & Rahim, A. (2020). Programmable Photonics: An Opportunity for an Accessible Large-Volume PIC Ecosystem. *IEEE Journal of Selected Topics in Quantum Electronics, 26*(5), 1-17. doi:10.1109/JSTQE.2020.2982980

Boroojerdi, M. T., Ménard, M., & Kirk, A. G. (2016a). Two-period contra-directional grating assisted coupler. *Optics Express, 24*(20), 22865-22874. doi:10.1364/OE.24.022865

Boroojerdi, M. T., Ménard, M., & Kirk, A. G. (2016b). Wavelength tunable integrated add-drop filter with 10.6 nm bandwidth adjustability. *Optics Express, 24*(19), 22043-22050. doi:10.1364/OE.24.022043

Brenes, A., Vysotskyi, B., Lefeuvre, E., & Juillard, J. (2019, 12-15 May 2019). *Reliability of etching angle estimation of MEMS resonators from electrical measurements.* Paper

presented at the 2019 Symposium on Design, Test, Integration & Packaging of MEMS and MOEMS (DTIP).

Brière, J., Beaulieu, P.-O., Saidani, M., Nabki, F., & Menard, M. (2015). *Rotational MEMS mirror with latching arm for silicon photonics* (Vol. 9375): SPIE.

Briere, J., Elsayed, M. Y., Saidani, M., Bérard, M., Beaulieu, P.-O., Rabbani-Haghighi, H., . . . Ménard, M. (2017). Rotating Circular Micro-Platform with Integrated Waveguides and Latching Arm for Reconfigurable Integrated Optics. *Micromachines, 8*(12), 354. Retrieved from https://www.mdpi.com/2072-666X/8/12/354

Budd, R. A., Schares, L., Lee, B. G., Doany, F. E., Baks, C., Kuchta, D. M., . . . Libsch, F. (2015, 26-29 May 2015). *Semiconductor optical amplifier (SOA) packaging for scalable and gain-integrated silicon photonic switching platforms.* Paper presented at the 2015 IEEE 65th Electronic Components and Technology Conference (ECTC), San Diego, CA, USA

Cai, K., Tian, Y., Wang, F., Zhang, D., Liu, X., & Shirinzadeh, B. (2017). Design and control of a 6-degree-of-freedom precision positioning system. *Robotics and Computer-Integrated Manufacturing, 44*, 77-96.

Carrara, D., Shen, A., Pommarede, X., Levaufre, G., Girard, N., Make, D., . . . Kopp, C. (2017). *Hybrid III-V/silicon photonic integrated circuits for high bitrates telecommunication applications.*

Chang, T.-H., Zhou, X., Tamura, H., & Hung, C.-L. (2022). Realization of efficient 3D tapered waveguide-to-fiber couplers on a nanophotonic circuit. *Optics Express, 30*(18), 31643-31652. doi:10.1364/OE.468738

Chatzitheocharis, D., Ketzaki, D., Calò, C., Caillaud, C., & Vyrsokinos, K. (2020). Design of Si-rich nitride interposer waveguides for efficient light coupling from InP-based QD-emitters to Si3N4 waveguides on a silicon substrate. *Optics Express, 28*(23), 34219-34236. doi:10.1364/OE.401225

Chen, S. H., Michael, A., & Kwok, C. Y. (2018, 22-26 April 2018). *A Fast Response MEMS Piezoelectric Microlens Actuator with Large Stroke and Low Driving Voltage.* Paper presented at the 2018 IEEE 13th Annual International Conference on Nano/Micro Engineered and Molecular Systems (NEMS).

Chen, Y., Zhao, X., Li, Z., Ke, X., Wang, C., Zhou, M., . . . Ou, X. (2022). Wafer-Scale Fabrication of Silicon Film on Lithium Niobate on Insulator (LNOI). *Crystals, 12*(10), 1477. Retrieved from https://www.mdpi.com/2073-4352/12/10/1477

Chien, C.-H., Su, T.-H., Wang, C.-T., Gan, J.-L., & Wang, J.-S. (2017). *The effects of film thickness variations on the residual stress distributions in coated Cr thin films* (Vol. 53).

Chollet, F. (2016). Devices Based on Co-Integrated MEMS Actuators and Optical Waveguide: A Review. *Micromachines, 7*(2), 18. doi:10.3390/mi7020018

Chollet, F., & Liu, H. (2018, 10 Aug 2018). A (not so) short introduction to MEMS. Retrieved from http://memscyclopedia.org/introMEMS.html

Cowen, A., Hames, G., Glukh, K., & Hardy, B. (2014). *PiezoMUMPs™ Design Handbook*.

Cragun, R., & Howell, L. L. (1999). *Linear Thermomechanical Microactuators.* Paper presented at the ASME 1999 International Mechanical Engineering Congress and Exposition.

Damjanovic, D. (2008). Lead-Based Piezoelectric Materials. In A. Safari & E. K. Akdogan (Eds.), *Piezoelectric and Acoustic Materials for Transducer Applications*: Springer: Boston, MA, USA.

De Groote, A., Cardile, P., Subramanian, A. Z., Fecioru, A. M., Bower, C., Delbeke, D., . . . Roelkens, G. (2016). Transfer-printing-based integration of single-mode waveguide-coupled III-V-on-silicon broadband light emitters. *Optics Express, 24*(13), 13754-13762. doi:10.1364/OE.24.013754

Devices, A. (2007). 24-Bit Capacitance-to-Digital Converter with Temperature Sensor. In M. Analog Devices: Cambridge, USA (Ed.).

Di, L., & John, E. B. (2021). *Recent Progress in Heterogeneous III-V-on-Silicon Photonic Integration* (Vol. 2).

Ding, Z., Sun, J., Li, C., & Shi, Y. (2023). Broadband Ultrasound Detection Using Silicon Micro-Ring Resonators. *Journal of Lightwave Technology, 41*(6), 1906-1910. doi:10.1109/JLT.2022.3227064

Doany, F. E., Budd, R., Schares, L., Huynh, T., Wood, M., Kuchta, D., . . . Lo, G. Q. (2016, 31 May-3 June 2016). *A Four-Channel Silicon Photonic Carrier with Flip-Chip Integrated Semiconductor Optical Amplifier (SOA) Array Providing >10-dB Gain.* Paper presented at the 2016 IEEE 66th Electronic Components and Technology Conference (ECTC), Las Vegas, NV, USA

Du, H., Chau, F. S., & Zhou, G. (2016). Mechanically-Tunable Photonic Devices with On-Chip Integrated MEMS/NEMS Actuators. *Micromachines, 7*(4), 69. Retrieved from http://www.mdpi.com/2072-666X/7/4/69

Edinger, P., Takabayashi, A. Y., Errando-Herranz, C., Khan, U., Sattari, H., Verheyen, P., . . . Gylfason, K. B. (2021). Silicon photonic microelectromechanical phase shifters for

scalable programmable photonics. *Optics Letters, 46*(22), 5671-5674. doi:10.1364/OL.436288

El Shamy, R. S., Afifi, A. E., Badr, M. M., & Swillam, M. A. (2022). Modelling, characterization, and applications of silicon on insulator loop terminated asymmetric Mach Zehnder interferometer. *Scientific Reports, 12*(1), 3598. doi:10.1038/s41598-022-07449-0

Errando-Herranz, C., Le Thomas, N., & Gylfason, K. B. (2019). Low-power optical beam steering by microelectromechanical waveguide gratings. *Optics Letters, 44*(4), 855-858. doi:10.1364/OL.44.000855

Errando-Herranz, C., Niklaus, F., Stemme, G., & Gylfason, K. B. (2015). Low-power microelectromechanically tunable silicon photonic ring resonator add-drop filter. *Optics Letters, 40*(15), 3556-3559. doi:10.1364/OL.40.003556

Espinosa, A., Rabenorosoa, K., Clévy, C., Komati, B., Lutz, P., Zhang, X., . . . Xie, H. (2014). Piston Motion Performance Analysis of a 3DOF Electrothermal MEMS Scanner for Medical Applications. *International Journal of Optomechatronics, 8*(3), 179-194. doi:10.1080/15599612.2014.916581

Fan, Y., Cui, C., Yu, H., Shen, W., Wang, Z., & Li, J. (2017, 9-12 April 2017). *An electrostatic vertical comb-drive micromirror with self-aligned assembly.* Paper presented at the 2017 IEEE 12th International Conference on Nano/Micro Engineered and Molecular Systems (NEMS), Los Angeles, CA, USA.

Fang, A. W., Park, H., Cohen, O., Jones, R., Paniccia, M. J., & Bowers, J. E. (2006). Electrically pumped hybrid AlGaInAs-silicon evanescent laser. *Optics Express, 14*(20), 9203-9210. doi:10.1364/OE.14.009203

Fitsios, D., Alexoudi, T., Kanellos, G. T., Vyrsokinos, K., Pleros, N., Tekin, T., . . . Aalto, T. (2014). Dual SOA-MZI Wavelength Converters Based on III-V Hybrid Integration on a μm-Scale Si Platform. *IEEE Photonics Technology Letters, 26*(6), 560-563. doi:10.1109/LPT.2013.2297404

Fretz, M. (2009). *Flip Chip Bonding Technologies for Hybrid Integration.* (PhD). Université de Neuchâtel,

Gablech, I., Klempa, J., Pekárek, J., Vyroubal, P., Hrabina, J., Holá, M., . . . Neužil, P. (2020). Simple and Efficient AlN-Based Piezoelectric Energy Harvesters. *Micromachines, 11*(2), 143. Retrieved from https://www.mdpi.com/2072-666X/11/2/143

Gabrelian, A., Ross, G., Bespalova, K., & Paulasto-Kröckel, M. (2022). Unlocking the Potential of Piezoelectric Films Grown on Vertical Surfaces for Inertial MEMS. *Materials Today Communications, 33*, 104522. doi:10.1016/j.mtcomm.2022.104522

150

Ghosh, S. (2015). *Piezoelectric Acousto-Optical Modulation in Aluminum Nitride for Integrated RF-Photonics.* (PhD Ph.D. Thesis). Carnegie Mellon University, Pittsburgh, PA, USA,

Gora, M. J., Suter, M. J., Tearney, G. J., & Li, X. (2017). Endoscopic optical coherence tomography: technologies and clinical applications [Invited]. *Biomed Opt Express, 8*(5), 2405-2444. doi:10.1364/boe.8.002405

Grade, J. D., & Jerman, H. (2001, 17-22 March 2001). *MEMS electrostatic actuators for optical switching applications.* Paper presented at the OFC 2001. Optical Fiber Communication Conference and Exhibit. Technical Digest Postconference Edition (IEEE Cat. 01CH37171).

Guerre, R., Hibert, C., Burri, Y., Flückiger, P., & Renaud, P. (2005). Fabrication of vertical digital silicon optical micromirrors on suspended electrode for guided-wave optical switching applications. *Sensors and Actuators A: Physical, 123-124*, 570-583. doi:https://doi.org/10.1016/j.sna.2005.02.039

Haake, J. M., & Beranek, M. W. (1998, 25-28 May 1998). *In package micro-aligner for fiber-optic packaging.* Paper presented at the 1998 Proceedings. 48th Electronic Components and Technology Conference (Cat. No.98CH36206).

Hamed, S., Alain Yuji, T., Pierre, E., Peter, V., Kristinn, B. G., Wim, B., & Niels, Q. (2022). Silicon photonic microelectromechanical systems add-drop ring resonator in a foundry process. *Journal of Optical Microsystems, 2*(4), 044001. doi:10.1117/1.JOM.2.4.044001

Han, Q., Menard, M., & Shi, W. (2020). Superlattice Arrayed Waveguide Grating in Silicon Nitride. *IEEE Photonics Technology Letters, 32*, 1411-1414. doi:10.1109/LPT.2020.3028130

Han, Q., St-Yves, J., Chen, Y., Ménard, M., & Shi, W. (2019). Polarization-insensitive silicon nitride arrayed waveguide grating. *Optics Letters, 44*(16), 3976-3979. doi:10.1364/OL.44.003976

Han, Y., Park, H., Bowers, J., & Lau, K. M. (2022). Recent advances in light sources on silicon. *Advances in Optics and Photonics, 14*(3), 404-454. doi:10.1364/AOP.455976

Hatori, N., Shimizu, T., Okano, M., Ishizaka, M., Yamamoto, T., Urino, Y., . . . Arakawa, Y. (2014). A Hybrid Integrated Light Source on a Silicon Platform Using a Trident Spot-Size Converter. *Journal of Lightwave Technology, 32*(7), 1329-1336. doi:10.1109/JLT.2014.2304305

He, S., Ben Mrad, R., & Chong, J. (2011). Repulsive-force out-of-plane large stroke translation micro electrostatic actuator. *Journal of Micromechanics and Microengineering, 21*(7), 075002. doi:10.1088/0960-1317/21/7/075002

He, Y. (2021). *Piezoelectric MEMS Devices in CMOS-Compatible Platform.* (PhD). Purdue University Graduate School,

Henneken, V. A., Sassen, W. P., Vlist, W., Wien, W. H. A., Tichem, M., & Sarro, P. M. (2008). Two-Dimensional Fiber Positioning and Clamping Device for Product-Internal Microassembly. *Microelectromechanical Systems, Journal of, 17*, 724-734. doi:10.1109/JMEMS.2008.918393

Henneken, V. A., Tichem, M., & Sarro, P. M. (2006). In-package MEMS-based thermal actuators for micro-assembly. *Journal of Micromechanics and Microengineering, 16*(6), S107. doi:10.1088/0960-1317/16/6/S17

Hong, Z., Zhao, Y., Ma, Y., Shi, Y., Wang, X., & Chen, X. (2021, 23-27 Aug. 2021). *Multi-channel High Power Laser Array Chip for Silicon Photonic Integration.* Paper presented at the 2021 19th International Conference on Optical Communications and Networks (ICOCN).

Hussein, H., Fariborzi, H., & Younis, M. I. (2020). Modeling of Beam Electrothermal Actuators. *Journal of Microelectromechanical Systems*, 1-12. doi:10.1109/JMEMS.2020.3033477

Ikeda, T., & Hane, K. (2013a). A microelectromechanically tunable microring resonator composed of freestanding silicon photonic waveguide couplers. *Applied Physics Letters, 102*(22), 221113. doi:10.1063/1.4809733

Ikeda, T., & Hane, K. (2013b). A tunable notch filter using microelectromechanical microring with gap-variable busline coupler. *Optics Express, 21*(19), 22034-22042. doi:10.1364/OE.21.022034

Ikeda, T., Takahashi, K., Kanamori, Y., & Hane, K. (2010). Phase-shifter using submicron silicon waveguide couplers with ultra-small electro-mechanical actuator. *Optics Express, 18*(7), 7031-7037. doi:10.1364/OE.18.007031

Ikehashi, T., Ogawa, E., Yamazaki, H., & Ohguro, T. (2007, 10-14 June 2007). *A 3V Operation RF MEMS Variable Capacitor using Piezoelectric and Electrostatic Actuation with Lithographical Bending Control.* Paper presented at the TRANSDUCERS 2007 - 2007 International Solid-State Sensors, Actuators and Microsystems Conference.

Jiang, W., Mayor, F., Patel, R., McKenna, T., Sarabalis, C., & Safavi-Naeini, A. (2020). Nanobenders as efficient piezoelectric actuators for widely tunable nanophotonics at CMOS-level voltages. *Communications Physics, 3*, 156. doi:10.1038/s42005-020-00412-3

152

Jin, W., Yang, Q.-F., Chang, L., Shen, B., Wang, H., Leal, M. A., . . . Bowers, J. E. (2021). Hertz-linewidth semiconductor lasers using CMOS-ready ultra-high-Q microresonators. *Nature Photonics, 15*(5), 346-353. doi:10.1038/s41566-021-00761-7

Jovic, A., Uto, T., Hei, K., Sancho, J., Sanchez, N., Zinoviev, K., . . . Sarro, P. M. (2018, 21-25 Jan. 2018). *A highly miniturized single-chip MOEMS scanner for all-in-one imaging solution.* Paper presented at the 2018 IEEE Micro Electro Mechanical Systems (MEMS).

Kaajakari, V. (2009). *Practical MEMS*: Small Gear Publishing: Las Vegas, NV, USA.

Kaur, P., Boes, A., Ren, G., Nguyen, T. G., Roelkens, G., & Mitchell, A. (2021). Hybrid and heterogeneous photonic integration. *APL Photonics, 6*(6), 061102. doi:10.1063/5.0052700

Kazuhiro, T., Makoto, M., Hiroyuki, F., & Hiroshi, T. (2007, 21-25 Jan. 2007). *Topological layer switch technique for monolithically integrated electrostatic XYZ-stage.* Paper presented at the 2007 IEEE 20th International Conference on Micro Electro Mechanical Systems (MEMS).

Kim, M., Park, J.-H., Jeon, J.-A., Yoo, B.-W., Park, I., & Kim, Y.-K. (2009). High fill-factor micromirror array using a self-aligned vertical comb drive actuator with two rotational axes. *Journal of Micromechanics and Microengineering, 19*, 035014. doi:10.1088/0960-1317/19/3/035014

Kim, T., & Gorman, J. J. (2022, 9-13 Jan. 2022). *A 3-Dof Mems Motion Stage for Scanning Tunneling Microscopy.* Paper presented at the 2022 IEEE 35th International Conference on Micro Electro Mechanical Systems Conference (MEMS).

Kim, Y., Han, J.-H., Ahn, D., & Kim, S. (2021). Heterogeneously-Integrated Optical Phase Shifters for Next-Generation Modulators and Switches on a Silicon Photonics Platform: A Review. *Micromachines, 12*(6), 625. Retrieved from https://www.mdpi.com/2072-666X/12/6/625

Kim, Y. S., Dagalakis, N. G., & Gupta, S. K. (2012, August 12-15, 2012). *Design and Fabrication of a Three-DoF MEMS Stage Based on Nested Structures.* Paper presented at the ASME 2012 International Design Engineering Technical Conference & Computers and Information in Engineering Conference, Chicago, IL.

Kim, Y. S., Dagalakis, N. G., & Gupta, S. K. (2014). Design of MEMS based three-axis motion stage by incorporating a nested structure. *Journal of Micromechanics and Microengineering, 24*(7), 075009. doi:10.1088/0960-1317/24/7/075009

Kong, X., Cao, Y., Zhu, H., Nie, W., & Xi, Z. (2023). A Self-Latching MEMS Optical Interrupter With Status Monitoring for Laser Initiation System. *IEEE Transactions on Electron Devices, 70*(5), 2473-2480. doi:10.1109/TED.2023.3255159

Krainak, M., Stephen, M., Troupaki, E., Tedder, S., Reyna, B., Klamkin, J., . . . Komljenovic, T. (2019). *Integrated photonics for NASA applications* (Vol. 10899): SPIE.

Krupa, K. (2009). *Opto-numerical analysis of AlN piezoelectric thin film operating as an actuation layer in MEMS cantilevers.* (PhD Ph.D. Thesis). Université de Franche-Comté, Besançon, France,

Larsen, T., Doll, J. C., Loizeau, F., Hosseini, N., Peng, A. W., Fantner, G. E., . . . Pruitt, B. L. (2017). Rise time reduction of thermal actuators operated in air and water through optimized pre-shaped open-loop driving. *Journal of Micromechanics and Microengineering, 27*(4), 045005. doi:10.1088/1361-6439/aa5fd2

Lee, E.-H., Lee, S.-G., O, B. H., & Park, S. G. (2004). *Integration of micro-/nano-/quantum-scale photonic devices: scientific and technological considerations* (Vol. 5451): SPIE.

Lee, M. M., & Wu, M. C. (2005). MEMS-actuated microdisk resonators with variable power coupling ratios. *IEEE Photonics Technology Letters, 17*(5), 1034-1036. doi:10.1109/LPT.2005.845772

Legtenberg, R., Groeneveld, A. W., & Elwenspoek, M. (1996). Comb-drive actuators for large displacements. *Journal of Micromechanics and Microengineering, 6*(3), 320-329. doi:10.1088/0960-1317/6/3/004

Lelit, M., Słowikowski, M., Filipiak, M., Juchniewicz, M., Stonio, B., Michalak, B., . . . Piramidowicz, R. (2022). Passive Photonic Integrated Circuits Elements Fabricated on a Silicon Nitride Platform. *Materials, 15*(4), 1398. Retrieved from https://www.mdpi.com/1996-1944/15/4/1398

Leondes, C. T. (2006). *MEMS/NEMS Handbook Techniques and Applications* (Vol. 2): Springer.

LEXT OLS4100 3D measuring Laser microscope. (2005). In OLYMPUS (Ed.).

Li, N., Chen, G., Ng, D. K. T., Lim, L. W., Xue, J., Ho, C. P., . . . Lee, L. Y. T. (2022). Integrated Lasers on Silicon at Communication Wavelength: A Progress Review. *Advanced Optical Materials, 10*(23), 2201008. doi:https://doi.org/10.1002/adom.202201008

Li, N., Ho, C. P., Zhu, S., Fu, Y. H., Zhu, Y., & Lee, L. Y. T. (2021). Aluminium nitride integrated photonics: a review. *Nanophotonics, 10*(9), 2347-2387. doi:doi:10.1515/nanoph-2021-0130

Lindenmann, N. (2018). *Photonic Wire Bonding as a Novel Technology for Photonic Chip Interfaces.* (PhD in Engineering). Karlsruhe Institute of Technology (KIT),

Liu, L., Wang, E., Zhang, X., Liang, W., Li, X., & Xie, H. (2014). MEMS-based 3D confocal scanning microendoscope using MEMS scanners for both lateral and axial scan. *Sensors and Actuators A: Physical, 215*, 89-95. doi:https://doi.org/10.1016/j.sna.2013.09.035

Liu, T., Pagliano, F., & Fiore, A. (2017). Nano-opto-electro-mechanical switch based on a four-waveguide directional coupler. *Optics Express, 25*(9), 10166-10176. doi:10.1364/OE.25.010166

Liu, X., Kim, K., & Sun, Y. (2007, 22-25 Sept. 2007). *A MEMS Stage for 3-Axis Nanopositioning.* Paper presented at the 2007 IEEE International Conference on Automation Science and Engineering.

Liu, X., Liu, W., Ren, Z., Ma, Y., Dong, B., Zhou, G., & Lee, C. (2021). Progress of optomechanical micro/nano sensors: a review. *International Journal of Optomechatronics, 15*(1), 120-159. doi:10.1080/15599612.2021.1986612

Liu, X., Qiao, Q., Dong, B., Liu, W., Xu, C., Xu, S., & Zhou, G. (2022). MEMS enabled suspended silicon waveguide platform for long-wave infrared modulation applications. *International Journal of Optomechatronics, 16*(1), 42-57. doi:10.1080/15599612.2022.2137608

Liu, Y., Cai, Y., Zhang, Y., Tovstopyat, A., Liu, S., & Sun, C. (2020). Materials, Design, and Characteristics of Bulk Acoustic Wave Resonator: A Review. *Micromachines, 11*(7), 630. Retrieved from https://www.mdpi.com/2072-666X/11/7/630

Luo, S., Wang, D., Tang, J., Zhou, L., Duan, C., Wang, D., . . . Xie, H. (2018). Circumferential-scanning endoscopic optical coherence tomography probe based on a circular array of six 2-axis MEMS mirrors. *Biomed Opt Express, 9*(5), 2104-2114. doi:10.1364/BOE.9.002104

Mahameed, R., Sinha, N., Pisani, M. B., & Piazza, G. (2008). Dual-beam actuation of piezoelectric AlN RF MEMS switches monolithically integrated with AlN contour-mode resonators. *Journal of Micromechanics and Microengineering, 18*(10), 105011. doi:10.1088/0960-1317/18/10/105011

Manh, C. H., & Hane, K. (2009). Vacuum operation of comb-drive micro display mirrors. *Journal of Micromechanics and Microengineering, 19*(10), 105018. doi:10.1088/0960-1317/19/10/105018

Manosalvas-Kjono, S. N., Quan, R., & Solgaard, O. (2022). Integrated Amplitude and Phase Monitor for Micro-Actuators. *Micromachines (Basel), 13*(8). doi:10.3390/mi13081360

Marchetti, R., Lacava, C., Carroll, L., Gradkowski, K., & Minzioni, P. (2019). Coupling strategies for silicon photonics integrated chips [Invited]. *Photonics Research, 7*(2), 201-239. doi:10.1364/PRJ.7.000201

Marinins, A., Hänsch, S., Sar, H., Chancerel, F., Golshani, N., Wang, H. L., . . . Campenhout, J. V. (2023). Wafer-Scale Hybrid Integration of InP DFB Lasers on Si Photonics by Flip-Chip Bonding With sub-300 nm Alignment Precision. *IEEE Journal of Selected Topics in Quantum Electronics, 29*(3: Photon. Elec. Co-Inte. and Adv. Trans. Print.), 1-11. doi:10.1109/JSTQE.2022.3223641

Maroufi, M., Fowler, A. G., & Moheimani, S. O. R. (2017). MEMS for Nanopositioning: Design and Applications. *Journal of Microelectromechanical Systems, 26*(3), 469-500. doi:10.1109/JMEMS.2017.2687861

Mastronardi, V. M. (2016). *Piezoelectric Transducers Based on Aluminum Nitride and Polyimide for Tactile Applications.* (Ph.D Ph.D. Thesis). Politecnico di Torino, Turin, Italy,

Matsui, Y., Schatz, R., Che, D., Khan, F., Kwakernaak, M., & Sudo, T. (2021). Low-chirp isolator-free 65-GHz-bandwidth directly modulated lasers. *Nature Photonics, 15*, 59–63.

Matsumoto, T., Kurahashi, T., Konoike, R., Suzuki, K., Tanizawa, K., Uetake, A., . . . Sekiguchi, S. (2019). Hybrid-Integration of SOA on Silicon Photonics Platform Based on Flip-Chip Bonding. *Journal of Lightwave Technology, 37*(2), 307-313.

Megat Hasnan, M. M. I., Mohd Sabri, M. F., Mohd Said, S., & Nik Ghazali, N. N. (2014). Modeling of a High Force Density Fishbone Shaped Electrostatic Comb Drive Microactuator. *The Scientific World Journal, 2014*, 8. doi:10.1155/2014/912683

Michael, A., Chen, S. S., & Kwok, C. Y. (2016). Feedback Driven Fast Piezoelectric Micro-lens Actuator. *Procedia Engineering, 168*, 1492-1495. doi:https://doi.org/10.1016/j.proeng.2016.11.432

Miller, D. A. (1998). *Dense two-dimensional integration of optoelectronics and electronics for interconnections* (Vol. 10292): SPIE.

Moody, G., Sorger, V. J., Blumenthal, D. J., Juodawlkis, P. W., Loh, W., Sorace-Agaskar, C., . . . Camacho, R. M. (2022). 2022 Roadmap on integrated quantum photonics. *Journal of Physics: Photonics, 4*(1), 012501. doi:10.1088/2515-7647/ac1ef4

Mu, J., Alexoudi, T., Sheng Yong, Y., A. Vazquez-Cordova, S., Dijkstra, M., Worhoff, K., . . . Garcia Blanco, S. (2016). *Low-Loss Highly Tolerant Flip-Chip Couplers for Hybrid Integration of Si3N4 and Polymer Waveguides* (Vol. PP).

Mukhopadhyay, D., Dong, J., Pengwang, E., & Ferreira, P. (2008). A SOI-MEMS-based 3-DOF planar parallel-kinematics nanopositioning stage. *Sensors and Actuators A: Physical, 147*(1), 340-351.

Nabavi, S., M, M., x00E, nard, & Nabki, F. (2022). A SOI Out-of-Plane Electrostatic MEMS Actuator Based on In-Plane Motion. *Journal of Microelectromechanical Systems*, 1-10. doi:10.1109/JMEMS.2022.3190829

Nada, M., Nakajima, F., Tatsumi, S., Yamada, Y., Nakanishi, Y., Yoshimatsu, T., . . . Matsuzaki, H. (2020, 6-10 Dec. 2020). *Inverted p-down pin photodiode exceeding 70-GHz bandwidth featuring low operating bias voltage of 2 V.* Paper presented at the 2020 European Conference on Optical Communications (ECOC), Virtual Event, Belgium

Nagai, T., & Hane, K. (2018). Silicon photonic microelectromechanical switch using lateral adiabatic waveguide couplers. *Optics Express, 26*(26), 33906-33917. doi:10.1364/OE.26.033906

Nair, D., & Menard, M. (2021). A Compact Low-Loss Broadband Polarization Independent Silicon 50/50 Splitter. *IEEE Photonics Journal, PP*, 1-1. doi:10.1109/JPHOT.2021.3091539

Nezami, M. S., Radi, B., Gour, A., Xiong, Y., Taherzadeh-Sani, M., Ménard, M., . . . Liboiron-Ladouceur, O. (2018). Integrated RF Passive Low-Pass Filters in Silicon Photonics. *IEEE Photonics Technology Letters, 30*(23), 2052-2055. doi:10.1109/LPT.2018.2875895

Oda, K., Takao, H., Terao, K., Suzuki, T., Shimokawa, F., Ishimaru, I., & Oohira, F. (2012). Vertical comb-drive MEMS mirror with sensing function for phase-shift device. *Sensors and Actuators A: Physical, 181*, 61-69. doi:https://doi.org/10.1016/j.sna.2012.04.007

Overstolz, T. (2007). *Tunable Optical Microsystems featuring Vertical Electrostatic Comb Drives.* (Doctorate in Sciences). University of Neuchâtel,

Pantouvaki, M., Srinivasan, S. A., Ban, Y., Heyn, P. D., Verheyen, P., Lepage, G., . . . Campenhout, J. V. (2017). Active Components for 50 Gb/s NRZ-OOK Optical Interconnects in a Silicon Photonics Platform. *Journal of Lightwave Technology, 35*(4), 631-638. doi:10.1109/JLT.2016.2604839

Pengwang, E., Rabenorosoa, K., Rakotondrabe, M., & Andreff, N. (2013). *A Hybrid Electrostatic-piezoelectric Integrative Actuated Microsystem for Robot-assisted Laser Phonomicrosurgery.*

Peters, T.-J., & Tichem, M. (2015). Fabrication and characterization of suspended beam structures for SiO2 photonic MEMS. *Journal of Micromechanics and Microengineering, 25*(10), 105003. doi:10.1088/0960-1317/25/10/105003

Peters, T.-J., & Tichem, M. (2016a). Electrothermal actuators for SiO2 photonic MEMS. *Micromachines, Micromachines, 2016, 7, 200*. doi:10.3390/mi7110200

Peters, T.-J., & Tichem, M. (2016b). *On-chip positionable photonic waveguides for chip-to-chip optical interconnects*.

Peters, T.-J., Tichem, M., & Staufer, U. (2014). *Suspended photonic waveguide arrays for submicrometer alignment* (Vol. 9133): SPIE.

Peters, T., & Tichem, M. (2017). On-Chip Positionable Waveguides for Submicrometric Photonic Alignment. *Journal of Microelectromechanical Systems, 26*(6), 1259-1271. doi:10.1109/JMEMS.2017.2729945

Piazza, G., Felmetsger, V., Muralt, P., Olsson, R. H., & Ruby, R. (2012). Piezoelectric aluminum nitride thin films for microelectromechanical systems. *MRS Bulletin, 37*(11), 1051-1061. doi:10.1557/mrs.2012.268

Piyawattanametha, W., & Qiu, Z. (2012). Optical MEMS. In N. Islam (Ed.), *Microelectromechanical Systems and Devices*: IntechOpen.

Poot, M., & Tang, H. X. (2014). Broadband nanoelectromechanical phase shifting of light on a chip. *Applied Physics Letters, 104*(6), 061101. doi:10.1063/1.4864257

Potekhina, A., & Wang, C. (2019). Review of Electrothermal Actuators and Applications. *Actuators, 8*(4), 69.

Poulton, C. V., Byrd, M. J., Russo, P., Timurdogan, E., Khandaker, M., Vermeulen, D., & Watts, M. R. (2019). Long-Range LiDAR and Free-Space Data Communication With High-Performance Optical Phased Arrays. *IEEE Journal of Selected Topics in Quantum Electronics, 25*(5), 1-8. doi:10.1109/JSTQE.2019.2908555

Pruessner, M. W., Park, D., Stievater, T. H., Kozak, D. A., & Rabinovich, W. S. (2016). Broadband opto-electro-mechanical effective refractive index tuning on a chip. *Optics Express, 24*(13), 13917-13930. doi:10.1364/OE.24.013917

Pruessner, M. W., Roxworthy, B. J., Kozak, D. A., Tyndall, N. F., Rabinovich, W. S., & Stievater, T. H. (2022, 2022/07/24). *On-Chip Mode Conversion with MEMS-Tunable Phase-Matching*. Paper presented at the Optica Advanced Photonics Congress 2022, Maastricht,Limburg.

Qiao, Q., Sun, H., Liu, X., Dong, B., Xia, J., Lee, C., & Zhou, G. (2021). Suspended Silicon Waveguide with Sub-Wavelength Grating Cladding for Optical MEMS in Mid-Infrared. *Micromachines, 12*(11), 1311. Retrieved from https://www.mdpi.com/2072-666X/12/11/1311

Qiao, Q., Yazici, M. S., Dong, B., Liu, X., Lee, C., & Zhou, G. (2020). Multifunctional mid-infrared photonic switch using a MEMS-based tunable waveguide coupler. *Optics Letters, 45*(19), 5620-5623. doi:10.1364/OL.400132

158

Qiu, Z., Liu, Z., Duan, X., Khondee, S., Joshi, B., Mandella, M. J., . . . Wang, T. D. (2013). Targeted vertical cross-sectional imaging with handheld near-infrared dual axes confocal fluorescence endomicroscope. *Biomed Opt Express, 4*(2), 322-330. doi:10.1364/boe.4.000322

Qiu, Z., Pulskamp, J. S., Lin, X., Rhee, C.-H., Wang, T., Polcawich, R. G., & Oldham, K. (2010). Large displacement vertical translational actuator based on piezoelectric thin films. *Journal of micromechanics and microengineering : structures, devices, and systems, 20*(7), 075016. doi:10.1088/0960-1317/20/7/075016

Qu, H. (2016). CMOS MEMS Fabrication Technologies and Devices. *Micromachines (Basel), 7*(1). doi:10.3390/mi7010014

Qu, Y., Luo, T., Wen, Z., Wei, M., Gu, X., Chen, X., . . . Sun, C. (2023). Aluminum Nitride-Based Adjustable Effective Electromechanical Coupling Coefficient Film Bulk Acoustic Resonator. *Micromachines, 14*(1), 157. Retrieved from https://www.mdpi.com/2072-666X/14/1/157

Quack, N., Sattari, H., Takabayashi, A. Y., Zhang, Y., Verheyen, P., Bogaerts, W., . . . Gylfason, K. B. (2020). MEMS-Enabled Silicon Photonic Integrated Devices and Circuits. *IEEE Journal of Quantum Electronics, 56*(1), 1-10. doi:10.1109/JQE.2019.2946841

Quack, N., Takabayashi, A. Y., Sattari, H., Edinger, P., Jo, G., Bleiker, S. J., . . . Bogaerts, W. (2023). Integrated silicon photonic MEMS. *Microsystems & Nanoengineering, 9*(1), 27. doi:10.1038/s41378-023-00498-z

Que, L., Park, J. S., & Gianchandani, Y. B. (1999, 21-21 Jan. 1999). *Bent-beam electro-thermal actuators for high force applications.* Paper presented at the Technical Digest. IEEE International MEMS 99 Conference. Twelfth IEEE International Conference on Micro Electro Mechanical Systems (Cat. No.99CH36291).

Rabih, A. A. S., Kazemi, M., Ménard, M., & Nabki, F. (2023). Aluminum Nitride Out-of-Plane Piezoelectric MEMS Actuators. *Micromachines, 14*(700). doi:https://doi.org/10.3390/mi14030700

Rabih, A. A. S., Sharma, S., Pita, J., Ménard, M., & Nabki, F. (2023). Two-axis MEMS positioner for waveguide alignment in silicon nitride photonic integrated circuits. *Optics Express, 31*(19), 30797-30814. doi:10.1364/OE.500102

Rahim, M., Zeb, K., Lu, Z., Pakulski, G., Liu, J., Poole, P., . . . Zhang, X. (2019). Monolithic InAs/InP quantum dash dual-wavelength DFB laser with ultra-low noise common cavity modes for millimeter-wave applications. *Optics Express, 27*(24), 35368-35375. doi:10.1364/OE.27.035368

Ramirez, J. M., Elfaiki, H., Verolet, T., Besancon, C., Gallet, A., Néel, D., . . . Achouche, M. (2020). III-V-on-Silicon Integration: From Hybrid Devices to Heterogeneous Photonic Integrated Circuits. *IEEE Journal of Selected Topics in Quantum Electronics, 26*(2), 1-13. doi:10.1109/JSTQE.2019.2939503

Ramírez, J. M., Fanneau de la Horie, P., Provost, J.-G., Malhouitre, S., Néel, D., Jany, C., . . . Bitauld, D. (2021). Low-Threshold, High-Power On-Chip Tunable III-V/Si Lasers with Integrated Semiconductor Optical Amplifiers. *Applied Sciences, 11*(23), 11096. Retrieved from https://www.mdpi.com/2076-3417/11/23/11096

Rezaei, M., Lueke, J., Raboud, D., & Moussa, W. (2013). Challenges in fabrication and testing of piezoelectric MEMS with a particular focus on energy harvesters. *Microsystem Technologies, 19*(8), 1195-1219. doi:10.1007/s00542-012-1721-8

Richard Doerr, C. (2015). *Silicon photonic integration in telecommunications* (Vol. 3).

Richard, P., Diarmuid, B., John, O. C., Michael, G., Marta, N., Rob, L., . . . Brian, K. (2019). Mid-Infrared InP-Based Discrete Mode Laser Diodes. In H.-C. Guillermo & I. Roghayeh (Eds.), *Optical Fiber Applications* (pp. Ch. 2). Rijeka: IntechOpen.

Ruiz-Díez, V., Hernando-García, J., Toledo, J., Ababneh, A., Seidel, H., & Sánchez-Rojas, J. L. (2021). Piezoelectric MEMS Linear Motor for Nanopositioning Applications. *Actuators, 10*(2), 36. Retrieved from https://www.mdpi.com/2076-0825/10/2/36

S, P., Shinde, S. D., Kumar, H., & Kharat, D. K. (2012, 7-10 March 2012). *Characterization of PZT multi-layer actuator.* Paper presented at the 2012 1st International Symposium on Physics and Technology of Sensors (ISPTS-1), Pune, India.

Sadhukhan, D., & Prasad Singh, G. (2022). Design of electrostatic actuated MEMS biaxial scanning micro-mirror with serpentine structure. *Materials Today: Proceedings, 65*, 229-234. doi:https://doi.org/10.1016/j.matpr.2022.06.120

Sandhu, G., Meade, R., Bi, L., & Smythe, J. (2017). US Patent No. United States: I. Micron Technology.

Sanjay Joshi, A., Mohammed, H., & Kulkarni, S. M. (2018). Analysis of a Chevron Beam Thermal Actuator. *IOP Conference Series: Materials Science and Engineering, 310*(1), 012123. doi:10.1088/1757-899X/310/1/012123

Sano, C., Ataka, M., Hashiguchi, G., & Toshiyoshi, H. (2020). An Electret-Augmented Low-Voltage MEMS Electrostatic Out-of-Plane Actuator for Acoustic Transducer Applications. *Micromachines, 11*(3), 267.

Sattari, H., Takabayashi, A. Y., Zhang, Y., Verheyen, P., Bogaerts, W., & Quack, N. (2020). Compact broadband suspended silicon photonic directional coupler. *Optics Letters, 45*(11), 2997-3000. doi:10.1364/OL.394470

Schneider, M., Pfusterschmied, G., Patocka, F., & Schmid, U. (2020). High performance piezoelectric AlN MEMS resonators for precise sensing in liquids. *e & i Elektrotechnik und Informationstechnik, 137*(3), 121-127. doi:10.1007/s00502-020-00794-w

Sciberras, T., Mollicone, P., Demicoli, M., Grech, I., Sammut, N., & Mallia, B. (2022, 11-13 July 2022). *Experimental and Numerical Analysis of MEMS Electrothermal Actuators with Cascaded V-shaped Mechanisms.* Paper presented at the 2022 Symposium on Design, Test, Integration and Packaging of MEMS/MOEMS (DTIP).

Segovia-Fernandez, J., Sonmezoglu, S., Block, S. T., Kusano, Y., Tsai, J. M., Amirtharajah, R., & Horsley, D. A. (2017, 18-22 June 2017). *Monolithic piezoelectric Aluminum Nitride MEMS-CMOS microphone.* Paper presented at the 2017 19th International Conference on Solid-State Sensors, Actuators and Microsystems (TRANSDUCERS), Kaohsiung, Taiwan.

Septon, T., Becker, A., Gosh, S., Shtendel, G., Sichkovskyi, V., Schnabel, F., . . . Eisenstein, G. (2019). Large linewidth reduction in semiconductor lasers based on atom-like gain material. *Optica, 6*(8), 1071-1077. doi:10.1364/OPTICA.6.001071

Shakespeare, W. J., Pearson, R. A., Grenestedt, J. L., Hutapea, P., & Gupta, V. (2005). MEMS integrated submount alignment for optoelectronics. *Journal of Lightwave Technology, 23*(2), 504-509. doi:10.1109/JLT.2004.841269

Sharma, S., Kohli, N., Brière, J., Ménard, M., & Nabki, F. (2019). Translational MEMS Platform for Planar Optical Switching Fabrics. *Micromachines, 10*(7), 435. Retrieved from https://www.mdpi.com/2072-666X/10/7/435

Sharma, S., Kohli, N., Brière, J., Nabki, F., & Ménard, M. (2022). Integrated 1x 3 MEMS silicon nitride photonics switch. *Optics Express, 30*(12), 22200-22220. doi:10.1364/OE.460533

Sharma, S., Nabavi, S., Rabih, A. A. S., Ménard, M., & Nabki, F. (2023a). Hybrid MEMS Actuator With 3 Degrees-of- Freedom for Efficient Planar Optical Switching. *Journal of Microelectromechanical Systems, 32*(6), 593-603. doi:10.1109/JMEMS.2023.3322223

Sharma, S., Nabavi, S., Rabih, A. A. S., Ménard, M., & Nabki, F. (2023b). Hybrid MEMS Actuator With 3 Degrees-of-Freedom for Efficient Planar Optical Switching. *Journal of Microelectromechanical Systems*, 1-11. doi:10.1109/JMEMS.2023.3322223

Shkel, C. A. A. (2009). *MEMS Vibratory Gyroscopes* Springer, Boston, MA.

Si, G., Ding, M., Zhang, Z., & Zhang, X. (2020, 13-16 Oct. 2020). *Design and Simulation of A Novel Three-Dimensional Multi-Degree-Of-Freedom Electrothermal Microgripper.* Paper presented at the 2020 IEEE International Conference on Mechatronics and Automation (ICMA), Beijing, China

Siew, S., Li, B., Feng, G., Zheng, H., Zhang, W., Guo, P., . . . Lo, P. (2021). Review of Silicon Photonics Technology and Platform Development. *Journal of Lightwave Technology, PP*, 1-1. doi:10.1109/JLT.2021.3066203

Sinclair, M. J. (2000, 23-26 May 2000). *A high force low area MEMS thermal actuator.* Paper presented at the ITHERM 2000. The Seventh Intersociety Conference on Thermal and Thermomechanical Phenomena in Electronic Systems (Cat. No.00CH37069).

Sinha, N., Wabiszewski, G., Mahameed, R., Felmetsger, V., Tanner, S., Carpick, R., & Piazza, G. (2009a). *Ultra Thin AlN Piezoelectric Nano-Actuators*. Paper presented at the Transducers 2009 - 2009 International Solid-State Sensors, Actuators and Microsystems Conference, Denver, CO, USA.

Sinha, N., Wabiszewski, G. E., Mahameed, R., Felmetsger, V. V., Tanner, S. M., Carpick, R. W., & Piazza, G. (2009b). Piezoelectric aluminum nitride nanoelectromechanical actuators. *Applied Physics Letters, 95*(5), 053106. doi:10.1063/1.3194148

Smith, J. A., Francis, H., Navickaite, G., & Strain, M. J. (2023). SiN foundry platform for high performance visible light integrated photonics. *Optical Materials Express, 13*(2), 458-468. doi:10.1364/OME.479871

Sridaran, S., & Bhave, S. A. (2011). Electrostatic actuation of silicon optomechanical resonators. *Optics Express, 19*(10), 9020-9026. doi:10.1364/OE.19.009020

Stanfield, P. R., Leenheer, A. J., Michael, C. P., Sims, R., & Eichenfield, M. (2019). CMOS-compatible, piezo-optomechanically tunable photonics for visible wavelengths and cryogenic temperatures. *Optics Express, 27*(20), 28588-28605. doi:10.1364/OE.27.028588

Su, Y., Liu, D., & Zhang, M. (2022). Sb2Se3-assisted reconfigurable broadband Y-junction. *Optics Express, 30*(22), 40379-40388. doi:10.1364/OE.473157

Suzuki, K., Tanizawa, K., Suda, S., Matsuura, H., Inoue, T., Ikeda, K., . . . Kawashima, H. (2017). Broadband silicon photonics 8 x 8 switch based on double-Mach-Zehnder element switches. *Optics Express, 25*(7), 7538-7546. doi:10.1364/OE.25.007538

Syms, R., & Liu, D. (2022). Buckling Electrothermal NEMS Actuators: Analytic Design for Very Slender Beams. *Micro, 2*(1), 54-67.

Takabayashi, A. Y., Sattari, H., Edinger, P., Verheyen, P., Gylfason, K. B., Bogaerts, W., & Quack, N. (2021a). Broadband Compact Single-Pole Double-Throw Silicon Photonic MEMS Switch. *Journal of Microelectromechanical Systems, 30*(2), 322-329. doi:10.1109/JMEMS.2021.3060182

Takabayashi, A. Y., Sattari, H., Edinger, P., Verheyen, P., Gylfason, K. B., Bogaerts, W., & Quack, N. (2021b, 20-24 June 2021). *Continuously Tunable Silicon Photonic MEMS 2×2 Power Coupler.* Paper presented at the 2021 21st International Conference on Solid-State Sensors, Actuators and Microsystems (Transducers).

Takahashi, K., Oyama, H., Misawa, N., Okumura, K., Ishida, M., & Sawada, K. (2013). Surface stress sensor using MEMS-based Fabry–Perot interferometer for label-free biosensing. *Sensors and Actuators B: Chemical, 188*, 393-399. doi:https://doi.org/10.1016/j.snb.2013.06.106

Tanner, D. M., Walraven, J. A., Helgesen, K. S., Irwin, L. W., Gregory, D. L., Stake, J. R., & Smith, N. F. (2000, 10-13 April 2000). *MEMS reliability in a vibration environment.* Paper presented at the 2000 IEEE International Reliability Physics Symposium Proceedings. 38th Annual (Cat. No.00CH37059).

Theurer, M., Moehrle, M., Sigmund, A., Velthaus, K. O., Oldenbeuving, R. M., Wevers, L., . . . Schell, M. (2019). Flip-Chip Integration of InP and SiN. *IEEE Photonics Technology Letters, 31*(3), 273-276. doi:10.1109/LPT.2019.2892851

Theurer, M., Moehrle, M., Sigmund, A., Velthaus, K. O., Oldenbeuving, R. M., Wevers, L., . . . Schell, M. (2020). Flip-Chip Integration of InP to SiN Photonic Integrated Circuits. *Journal of Lightwave Technology, 38*(9), 2630-2636. doi:10.1109/JLT.2020.2972065

Tian, Y., Lu, K., Wang, F., Zhou, C., Ma, Y., Jing, X., . . . Zhang, D. (2020). A Spatial Deployable Three-DOF Compliant Nano-Positioner With a Three-Stage Motion Amplification Mechanism. *IEEE/ASME Transactions on Mechatronics, 25*(3), 1322-1334. doi:10.1109/TMECH.2020.2973175

Uhlig, S., Gaudet, M., Langa, S., Schimmanz, K., Conrad, H., Kaiser, B., & Schenk, H. (2018). Electrostatically Driven In-Plane Silicon Micropump for Modular Configuration. *Micromachines, 9*(4), 190. Retrieved from https://www.mdpi.com/2072-666X/9/4/190

Ullmann, P. G., Bretthauer, C., Schneider, M., & Schmid, U. (2023). Stress analysis of circular membrane-type MEMS microphones with piezoelectric read-out. *Sensors and Actuators A: Physical, 349*, 114003. doi:https://doi.org/10.1016/j.sna.2022.114003

Unamuno, A., Yao, J., & Uttamchandani, D. (2005). Alignment and fixing of fiber optics based on electrothermal MEMS actuators. *IEEE Photonics Technology Letters, 17*(4), 816-818. doi:10.1109/LPT.2005.844006

Van Iseghem, L., Picavet, E., Takabayashi, A. Y., Edinger, P., Khan, U., Verheyen, P., . . . Bogaerts, W. (2022). Low power optical phase shifter using liquid crystal actuation on a silicon photonics platform. *Optical Materials Express, 12*(6), 2181-2198. doi:10.1364/OME.457589

Vargas-Chable, P., Tecpoyotl-Torres, M., Vera-Dimas, G., Grimalsky, V., & Mireles García, J., Jr. (2022). Novel Electrothermal Microgrippers Based on a Rotary Actuator System. *Micromachines (Basel), 13*(12). doi:10.3390/mi13122189

Vitali, V., Lacava, C., Domínguez Bucio, T., Gardes, F. Y., & Petropoulos, P. (2022). Highly efficient dual-level grating couplers for silicon nitride photonics. *Scientific Reports, 12*(1), 15436. doi:10.1038/s41598-022-19352-9

Wang, L., Peng, H., Zheng, L., Chen, H., Zhang, Y., Huang, J., . . . Zhu, M. (2023). Broadband and CMOS-compatible polarization splitter and rotator built on a silicon nitride-on-silicon multilayer platform. *Applied Optics, 62*(4), 1046-1056. doi:10.1364/AO.477870

Wang, W., Chen, J., Zivkovic, A. S., Tanguy, Q. A. A., & Xie, H. (2016). A Compact Fourier Transform Spectrometer on a Silicon Optical Bench With an Electrothermal MEMS Mirror. *Journal of Microelectromechanical Systems, 25*(2), 347-355. doi:10.1109/JMEMS.2016.2522767

Wei, W.-Q., He, A., Yang, B., Wang, Z.-H., Huang, J.-Z., Han, D., . . . Wang, T. (2023). Monolithic integration of embedded III-V lasers on SOI. *Light: Science & Applications, 12*(1), 84. doi:10.1038/s41377-023-01128-z

Wenqi, W., He, A., Yang, B., Huang, J.-Z., Han, D., Ming, M., . . . Wang, T. (2022). *Monolithic Integration of Embedded III-V Lasers on SOI.*

Wörhoff, K., Prak, A., Postma, F., Leinse, A., Wu, K., Peters, T. J., . . . Robbins, D. (2016). *Photonic hybrid assembly through flexible waveguides* (Vol. 9891): SPIE.

Wu, K., Peters, T.-J., Tichem, M., Postma, F., Prak, A., Worhoff, K., & Leinse, A. (2016). *Bimorph actuators in thick SiO 2 for photonic alignment.*

Wu, K., & Tichem, M. (2018). Post-Release Deformation and Motion Control of Photonic Waveguide Beams by Tuneable Electrothermal Actuators in Thick SiO2. *Micromachines, 9*(10), 496. Retrieved from https://www.mdpi.com/2072-666X/9/10/496

Xiang, C., Jin, W., Huang, D., Tran, M. A., Guo, J., Wan, Y., . . . Bowers, J. E. (2022). High-Performance Silicon Photonics Using Heterogeneous Integration. *IEEE Journal of Selected Topics in Quantum Electronics, 28*(3: Hybrid Integration for Silicon Photonics), 1-15. doi:10.1109/JSTQE.2021.3126124

164

Xiang, C., Jin, W., Terra, O., Dong, B., Wang, H., Wu, L., . . . Bowers, J. E. (2023). 3D integration enables ultralow-noise isolator-free lasers in silicon photonics. *Nature, 620*(7972), 78-85. doi:10.1038/s41586-023-06251-w

Xie, X., & Livermore, C. (2015). A high-force, out-of-plane actuator with a MEMS-enabled microscissor motion amplifier. *Journal of Physics: Conference Series, 660*(1), 012026. doi:10.1088/1742-6596/660/1/012026

Yada, H., Kamada, N., Onuki, Y., Han, X., Periyanayagam, G. K., Uchida, K., . . . Shimomura, K. (2018, 29 July-3 Aug. 2018). *Successful Fabrication of GaInAsP Ridge Waveguide Laser Diode Using Hydrophilic Bonded InP/Si Substrate.* Paper presented at the 2018 Conference on Lasers and Electro-Optics Pacific Rim (CLEO-PR).

Yang, C., Liang, L., Qin, L., Tang, H., Lei, Y., Jia, P., . . . Wang, L. (2023). Advances in silicon-based, integrated tunable semiconductor lasers. *Nanophotonics, 12*(2), 197-217. doi:doi:10.1515/nanoph-2022-0699

Yang, Y., Zhao, H., Ren, X., & Huang, Y. (2021). Monolithic integration of laser onto multilayer silicon nitride photonic integrated circuits with high efficiency at telecom wavelength. *Optics Express, 29*(18), 28912-28923. doi:10.1364/OE.434913

Yao, J., Leuenberger, D., Lee, M. M., & Wu, M. C. (2007). Silicon Microtoroidal Resonators With Integrated MEMS Tunable Coupler. *IEEE Journal of Selected Topics in Quantum Electronics, 13*(2), 202-208. doi:10.1109/JSTQE.2007.893743

Yao, Z., Wu, K., Tan, B. X., Wang, J., Li, Y., Zhang, Y., & Poon, A. W. (2018). Integrated Silicon Photonic Microresonators: Emerging Technologies. *IEEE Journal of Selected Topics in Quantum Electronics, 24*(6), 1-24. doi:10.1109/JSTQE.2018.2846047

Yunas, J., Mulyanti, B., Hamidah, I., Mohd Said, M., Pawinanto, R. E., Wan Ali, W. A. F., . . . Yeop Majlis, B. (2020). Polymer-Based MEMS Electromagnetic Actuator for Biomedical Application: A Review. *Polymers, 12*(5), 1184. Retrieved from https://www.mdpi.com/2073-4360/12/5/1184

Zeng, D., Liu, Q., Mei, C., Li, H., Huang, Q., & Zhang, X. (2022). Demonstration of Ultra-High-Q Silicon Microring Resonators for Nonlinear Integrated Photonics. *Micromachines (Basel), 13*(7). doi:10.3390/mi13071155

Zha, S., Li, D., Wen, Q., Zhou, Y., & Zhang, H. (2022). Design and Fabrication of Silicon-Blazed Gratings for Near-Infrared Scanning Grating Micromirror. *Micromachines (Basel), 13*(7). doi:10.3390/mi13071000

Zhang, J., Xu, H., Zhang, G., Chen, Y., Wang, H., Tan, K. H., . . . Gong, X. (2021, 13-19 June 2021). *First InGaAs/InAlAs Single-Photon Avalanche Diodes (SPADs) Heterogeneously Integrated with Si Photonics on SOI Platform for 1550 nm Detection.* Paper presented at the 2021 Symposium on VLSI Circuits.

Zhang, L., La, X., Zhu, X., Guo, J., Zhao, L., Wang, W., & Liang, S. (2022). High Speed Waveguide Uni-Traveling Carrier InGaAs/InP Photodiodes Fabricated By Zn Diffusion Doping. *IEEE Journal of Selected Topics in Quantum Electronics, 28*(2), 1-6. doi:10.1109/JSTQE.2021.3072702

Zhang, M., Wang, C., Kharel, P., Zhu, D., & Lončar, M. (2021). Integrated lithium niobate electro-optic modulators: when performance meets scalability. *Optica, 8*(5), 652-667. doi:10.1364/OPTICA.415762

Zhang, M., Yang, J., Si, C., Han, G., Zhao, Y., & Ning, J. (2015). Research on the Piezoelectric Properties of AlN Thin Films for MEMS Applications. *Micromachines, 6*(9), 1236-1248. Retrieved from https://www.mdpi.com/2072-666X/6/9/1236

Zhang, Q. X., Du, Y., Tan, C. W., Zhang, J., Yu, M. B., Yeoh, W. G., . . . Kwong, D. (2010). A Silicon Platform With MEMS Active Alignment Function and Its Potential Application in Si-Photonics Packaging. *IEEE Journal of Selected Topics in Quantum Electronics, 16*(1), 267-275. doi:10.1109/JSTQE.2009.2034271

Zhang, X., Zhou, L., & Xie, H. (2016, 24-28 Jan. 2016). *A large range micro-XZ-stage with monolithic integration of electrothermal bimorph actuators and electrostatic comb drives.* Paper presented at the 2016 IEEE 29th International Conference on Micro Electro Mechanical Systems (MEMS), Shanghai, China

Zhang, Y., Liu, S., Zhai, W., Peng, C., Wang, Z., Feng, J., & Guo, J. (2021). Reconfigurable spot size converter for the silicon photonics integrated circuit. *Optics Express, 29*(23), 37703-37711. doi:10.1364/OE.438652

Zhou, G., & Lee, C. (2018). Optical MEMS: An introduction. In G. Zhou & C. Lee (Eds.), *Optical MEMS, Nanophotonics, and Their Applications*: Tayler and Francis Group.

Zhou, G., Lim, Z. H., Qi, Y., Chau, F. S., & Zhou, G. (2021). MEMS gratings and their applications. *International Journal of Optomechatronics, 15*(1), 61-86. doi:10.1080/15599612.2021.1892248

Zhou, Z., Ou, X., Fang, Y., Alkhazraji, E., Xu, R., Wan, Y., & Bowers, J. E. (2023). Prospects and applications of on-chip lasers. *eLight, 3*(1), 1. doi:10.1186/s43593-022-00027-x

Zia, N., Tuorila, H., Viheriälä, J., Ojanen, S.-P., Koivusalo, E., Hilska, J., & Guina, M. (2022). Hybrid silicon photonics DBR laser based on flip-chip integration of GaSb amplifiers and µm-scale SOI waveguides. *Optics Express, 30*(14), 24995-25005. doi:10.1364/OE.460883